Dissertations and Theses

6-2013

A 3-D Model of the Auroral Ionosphere

Yishi Lee
Embry-Riddle Aeronautical University - Daytona Beach

Scholarly Commons Citation

A 3-D Model
of
the Auroral Ionosphere

by

Yishi Lee

A thesis submitted to the

Physical Sciences Department

in partial fulfilment of the requirements for the degree of

Master of Science in Engineering Physics

Embry-Riddle Aeronautical University

Daytona Beach, Florida

June 2013

A 3-D Model of the Auroral Ionosphere
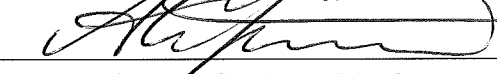
by

Yishi Lee

This thesis was prepared under the direction of the candidate's thesis committee chair, Dr. Matthew Zettergren, Department of Physical Sciences, and has been approved by the members of the thesis committee. It was submitted to the Department of Physical Sciences and was accepted in partial fulfillment of the requirement of the Degree of

Masters of Science in Engineering Physics

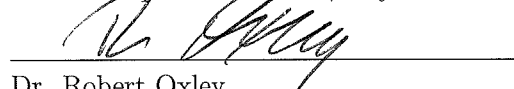THESIS COMMITTEE
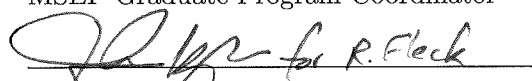
_____
Dr. Matthew Zettergren, Chair

_____
Dr. John Hughes, Member

_____
Dr. Jonathan B. Snively, Member

_____
Dr. Anatoly Streltsov, Member

_____
Dr. Peter Erdman
MSEP Graduate Program Coordinator

_____
Dr. Robert Fleck
Interim Department Chair, Physical Sciences

_____
Dr. Robert Oxley
Associate Vice President for Academics

6-11-13
_____
Date

iii

Abstract

A new 3-D model of the high latitude ionosphere is developed to study the coupling of the ionosphere with the magnetosphere and neutral atmosphere. The model consists of equations describing conservations of mass, momentum and energy for the six ionospheric constituents (O^+, NO^+, N_2^+, O_2^+, N^+ and e^-) and an electrostatic potential equation. This 3-D model is used to examine interrelated processes of ion heating, plasma structuring due to perpendicular transport, ion upflow, molecular ion generation, and neutral wave forcing. It is first validated by comparisons with a 2-D model, which uses similar mathematical and numerical approaches, and is additionally compared against incoherent scatter radar data. Results from a simulation of ionospheric response to a large amplitude acoustic wave also suggests an important role for these waves in generating local dynamo currents and density variations. Results of this model also shed some light on the interplay of perpendicular and parallel transports of plasma in producing structures in density and drift velocity profiles.

THIS PAGE INTENTIONALLY LEFT BLANK

Acknowledgments

More than a year long of research allows me to understand the challenging journey of being a researcher. Every footprint is marked with devotions, dedications, teamwork and supports from the people who are involved. Certainly, the success of this project relies on many important elements. Among them, the human element is the most critical factor that enables me to come to the final chapter of this work. Therefore, I want to start off by giving a special thank to my dear mother who has been encouraging me to pursue my passions. Not only her nurturing and teaching helped me to discover my dreams, but also motivated me to continue pursuing my goals. Therefore, I want to first dedicate this paper to her as a gift to signify the sacrifices and devotions she has made to support me. Secondly, I also want to dedicate this to my mentor, Dr. Matthew Zettergren who has funded the entire project. His technical depth and breadth in this area are truly profound. His articulated guidance and attention to details assisted me tremendously to overcome many technical challenges. Therefore, I also want to dedicate this work to him. Thirdly, I want to thank my friends and peers for their continuously supports during this time. Finally, I want to thank Embry-Riddle Aeronautical University for providing me with an academically challenging and nurturing environment to learn and conduct research during my time here.

THIS PAGE INTENTIONALLY LEFT BLANK

Contents

List of Tables

List of Figures

xvi

Chapter 1

Introduction

This project aims to simulate dynamic processes occurring in the high-latitude ionosphere. By incorporating models of the mathematical descriptions of ionospheric physics, we develop a platform to understand the three dimensional evolution of various aeronomic and transport processes. Three-Dimensional (3-D) numerical models have been developed for the mid latitude regions to study the effects of the Perkins instability [Yokoyama et al., 2008; Yokoyama et al., 2009] and equatorial spread F [Huba et al., 2009]. However, due to the magnetospheric interactions in the high latitude region, the auroral ionosphere experiences a different range of energetic processes. As a result, it becomes essential to develop a 3-D high latitude ionospheric model to study the impacts of these phenomena. Currently, 2-D models have been developed which are capable to demonstrate many main processes. For example, the depletion process in the E and F regions, ion upflow process in the upper regions and plasma enhancement process in the E region [Zettergren and Semeter, 2012], [Zhu et al., 2001] and [Noël et al., 2000]. This present work seeks to extend these

studies by investigating effects of non-uniformity in density, energy flux or imposed boundary conditions in 3-D. We focus specifically on the evolution of plasma density structures, heating due to ion-neutral coupling, plasma flows and ion composition changes through chemistry.

The outcome of this project is to provide a comprehensive test bed for researchers to analyze the ionospheric physics and enhance our understanding of various ionospheric responses. We begin in Chapter 2 with an introduction to the fundamentals of high latitude ionospheric physics including the formations of the ionosphere and some basic processes. In Chapter 3, we then delve into the mathematical descriptions and formulations of a new 3-D ionospheric model including the important numerical techniques used along with the implementations. In Chapter 4, we will first validate our model by making direct comparisons with previous work done in 2-D [Zettergren and Semeter, 2012], and also analyze some simple 3D geometries. Finally in Chapter 5, we will employ this model in case studies of the ionospheric responses to (1) realistic potential patterns and (2) large amplitude acoustic waves.

Chapter 2

Terrestrial Ionosphere

2.1 Basic Ionospheric Processes

The basic features of the ionosphere are a consequence of the interactions among three physical processes: Photoionizaton, chemical interactions (charge exchange and recombination processes), and field aligned diffusion of plasma. These three processes result in the typical layered plasma density profile (shown in Figure 2.1) . In the next few sections, we will discuss each process and the associated contributions to the formation of ionosphere. We will also outline several high-latitude features of specific interest to this research.

2.1.1 Photoionization

The solar extreme ultraviolet (EUV) and X-ray radiation are the two main wavelength ranges that interact strongly with the earth's neutral atmosphere and produce plasma through the different photoionization processes [Richards et al., 1994] and
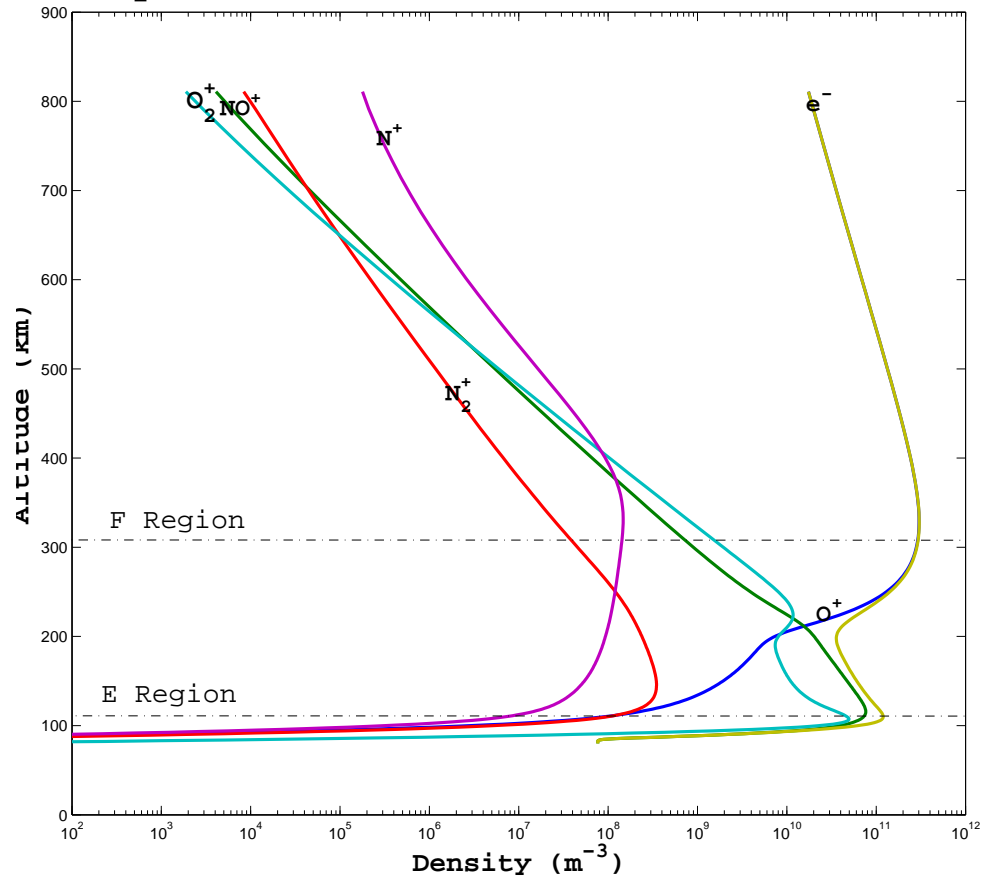
Figure 2.1: A nominal density profile is an equilibrim profile generated by the 3-D auroral ionospheric model.

[Solomon and Qian, 2005]. As solar radiation propagates downwards through the Earth's Atmosphere, the energy is absorbed in creation of ion-electron pairs. Absorption also results in heating which allows high temperatures to be maintained in the thermosphere. With the basic assumptions of monochromatic radiation and a single ionizable gas, this process is succinctly described using the Chapman theory [Rishbeth and Garriott, 1969]. However, the interactions of solar radiation with the neutral atmosphere are highly wavelength dependent. With the aid of high altitude rockets, direct measurements have been made to construct a quantitative picture of different ionization processes. In the D region, depending on the solar activity, both X-rays spectrum $\alpha = 1 \sim 8$ Å and Lyman α with $\lambda = 1286$ Å can ionize some major constituents (O_2 and NO) in that region. Similarly in the E-region, X-rays with a wavelength between 100 and 31 Å, Lyman β of 1025.7 Å and Lyman continuum of less than 910 Å dominate the ionization of O_2 and N_2. Figure 2.2 shows the electron production rate $p_e(h)$ as a function of altitude and wavelength of the incident radiation for typical daytime, mid-latitude conditions.

2.1.2 Chemistry

In addition to the photoionization process, which constitutes the productions of the ionosphere, the chemical production and loss also play an important role in determining the density of constituents including ions present in the ionospheric regions. Two main chemical processes (charge exchange and recombination) that govern the chemical compositions of the auroral ionosphere are discussed:
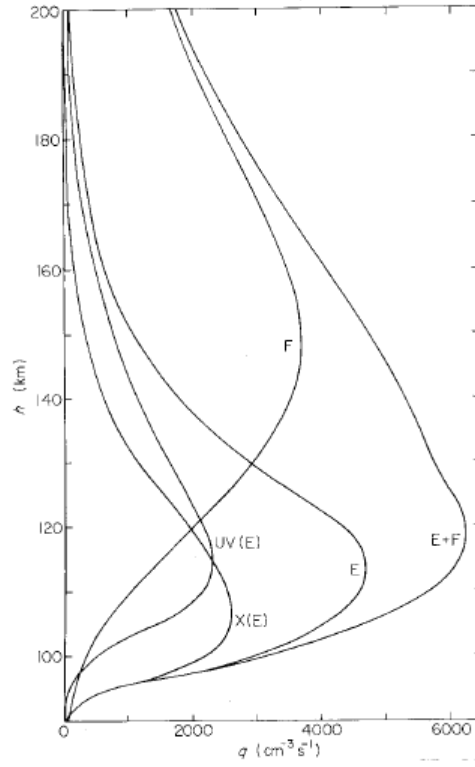
Figure 2.2: X(E) = 8 ∼ 140 Å, UV(E) = 796 ∼ 1027 Å, E = UV(E)+X(E), F = 140 ∼ 796 Å; E+F = 8 ∼ 1027 Å [Rishbeth and Garriott, 1969, Fig. 24 on pp. 101].

Charge Exchange Processes

Reactions involving charge exchange perform momentum transfer in the process. More specifically, the reactant of this process first exchanges the electric charge with the neutral particles, and after the process is complete, the kinetic energy remains the same. This sudden transition produces different kinds of ion species, and also gives resulting neutral particles a different energy spectrum. In addition, due to the nature of momentum/energy transfer in this process, the charge exchange reactions are highly sensitive to temperature variations [St.-Maurice and Laneville, 1998]. The general formula for charge exchange is listed as follows:

$$WX^+ + YZ \rightarrow WX + YZ^+ \tag{2.1}$$

The reaction constant is usually in the order of $10^{-10}\text{cm}^3\text{s}^{-1}$. Full lists of reactions can be found in [Schunk and Nagy, 2004], [Rishbeth and Garriott, 1969] and [Banks and Kockarts, 1973]. In addition, depending on the bond of the neutral particle, a charged particle can also break a molecular bound to form a new charged species:

$$X^+ + YZ \rightarrow XY^+ + Z \tag{2.2}$$

Recombination

There are two kinds of recombination reactions. The first one is radiative recombination. When an electron "strikes" a charged ion, it excites and neutralizes the charged particle. The excited particle emits a photon to decay to a lower energy state. This situation is very similar to the inverse of photoionization. The general reaction formula is as follows:

$$X^+ + e^- \rightarrow X^* + h\nu \tag{2.3}$$

This reaction is typically quite slow, and occurs at reaction constant in the order of $10^{-12} \text{cm}^3 \text{s}^{-1}$

The second type of recombination reaction is the dissociative recombination, and it is most frequently occurred in the ionospheric environment. The production usually excites the resulting atoms, and converts the excess energy into kinetic energy of the products. This reaction has fast rate, of the order of $10^{-7} \text{cm}^3/\text{sec}$. A typical reaction of this kind is represented in the following:

$$\text{XY}^+ + \text{e}^- \rightarrow \text{X} + \text{Y} \tag{2.4}$$

Dissociative recombination rates are listed in Schunk and Sojka [1982]. Note, the recombination of electron and atomic ions can take place only by a very slow radiative process. In the F and E regions, dissociative recombination dominates the chemistry. Figure 2.3 provided by Blelly et al. [1996] gives a complete diagram of the terrestrial ionospheric chemical processes, with specific products and reactants.

2.1.3 Geomagnetic Field-Aligned Diffusion

Field-aligned diffusion is an important contributor to the ionospheric profile in the F-region and topside. It helps explain the formation of the F2 peak. At the ionospheric altitudes, four major forces act on particles: Gravity, Lorentz force, neutral collisions, and pressure gradient. Figure 2.4 illustrates these forces. Note that the gravity force can be neglected for the electrons owing to a much smaller mass. A force equilibrium condition is achieved if the sum of forces acting equals to zero. Here, ∇p_s is the pressure gradient of species "s", $n_s m_s g$ is the force due to gravity and $n_s m_s \nu_{in}(\mathbf{v}_i - \mathbf{v}_n)$
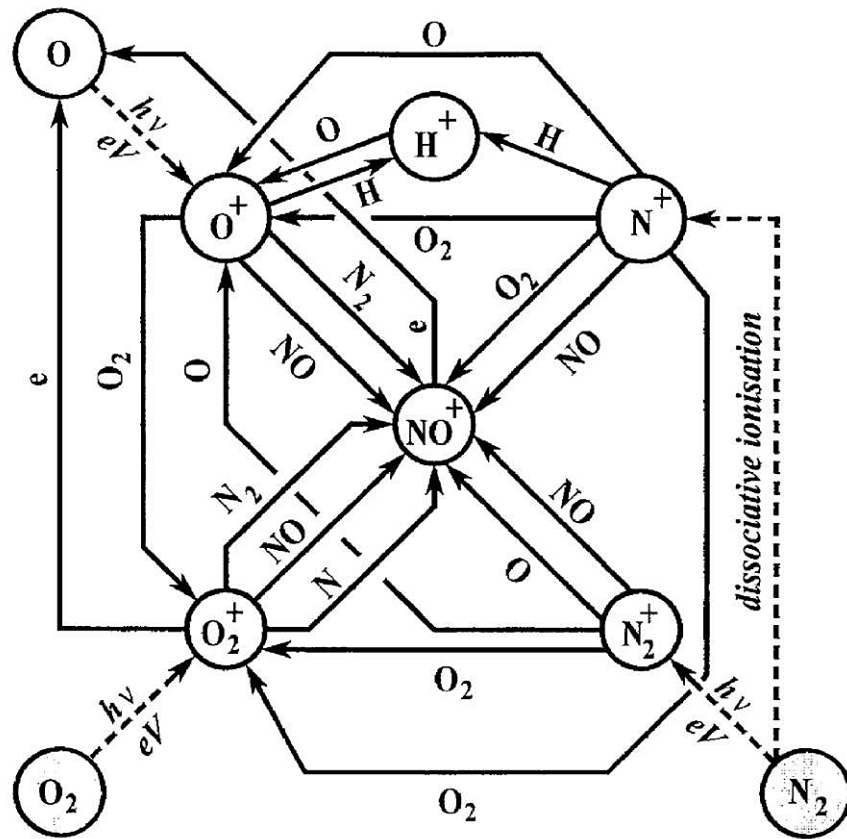
Figure 2.3: Chemistry in Ionosphere [Blelly et al., 1996].

is the collisional force,

$$\sum F = -\nabla p_s - n_s m_s g + n_s q_s E - n_s m_s \nu_{in}(\mathbf{v}_i - \mathbf{v}_n) = 0. \qquad (2.5)$$

Similarly, the equation for electrons becomes

$$\sum F = -\nabla p_e - n_e m_e g + n_e q_e E - n_e m_e \nu_{in}(\mathbf{v}_e - \mathbf{v}_n) = 0. \qquad (2.6)$$

The above equations 2.5 and 2.6 can be solved by imposing the Ideal Gas Law $p_s = n_s k T_s$ and $p_e = n_e k T_e$. By invoking the conservation of mass and deploying simple mathematical manipulations, solution for density in absence of production/loss (valid only for topside) can be found from the continuity equation for density. More specifically, by solving for the velocities of ionospheric species $\mathbf{v}_s$, and substituting them to the continuity equation, it produces a diffusion equation. A more detailed discussion can be found in Schunk and Walker [1973].

2.2 High Latitude Ionosphere

On a global scale, the high latitude ionosphere is coupled with the magnetosphere, generating three interrelated processes: Global scale current systems, perpendicular particle convection pattern in the polar region, and the polar wind. These processes represent disturbances to the "background" ionosphere (see Section 2.1) and also relate to the smaller scale auroral ionospheric disturbances focused on in this work.
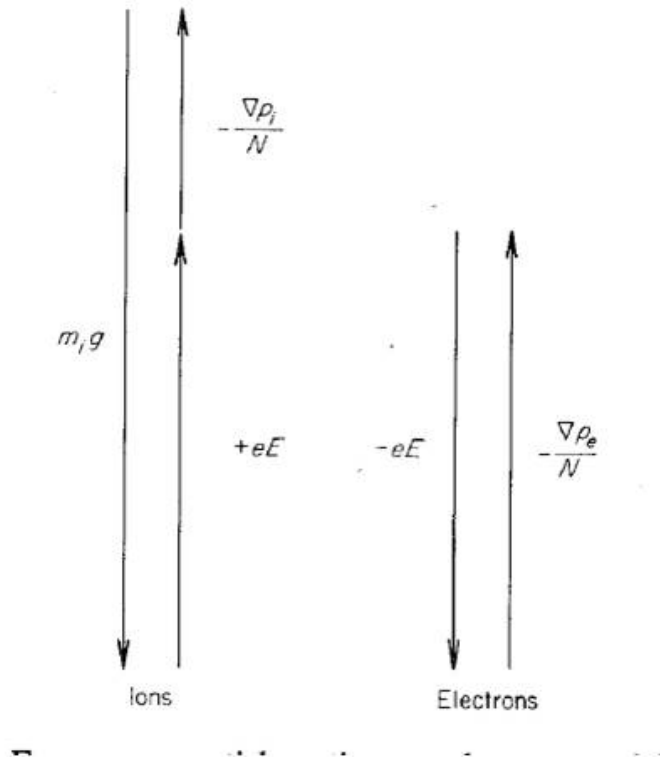
Figure 2.4: A simplified diagram illustrates the vertical forces that contribute to the ionospheric momentum balance [Rishbeth and Garriott, 1969, Fig. 36 on pp. 149].

2.2.1 Global Scale Current System and 2-Cell Convection Pattern

Interactions between the solar wind/geomagnetic field induce motional EMFs, producing current flows into the ionosphere which acts as a resistive load in the "circuit". Depending on the locations of the sources for the currents, we classify them as the Region-1 (R_1) and Region-2 (R_2) current systems. First of all, R_1 currents link the poleward portion of the auroral oval and the polar cap to the magnetosheath, solar wind, or the boundary layer plasma near the magnetopause. R_2 currents link the inner magnetosphere with the auroral oval near its equatorward edge [Kelley, 2009]. For a very long time scale, we can assume that the currents have zero divergence (see Section 3.2). Pedersen currents through ionosphere to close the loop from both the highest latitude and the auroral zone regions of the ionosphere. This system is illustrated in Figure 2.5. In addition, the electric field concurrent with the current system, combined with the magnetic field, implies an $\mathbf{E} \times \mathbf{B}$ drift. The result of this process is the well known 2-cell convection pattern.

The convection pattern implies that plasma is transported from the dayside to the nightside in the polar cap region, and it is recirculated to dayside. Studies have shown that the B_y of the IMF contributes the most to the geometrical size of the convection cells [Heelis, 1984]. In addition, data from DE2 spacecrafts also suggests that this perpendicular drift pattern could result in frictional heating with the neutral gas creating upflow velocity. This correlation between the pependiuclar convection flow and the upflow of plasma has been well examined by some authors [Heelis et al., 1992].
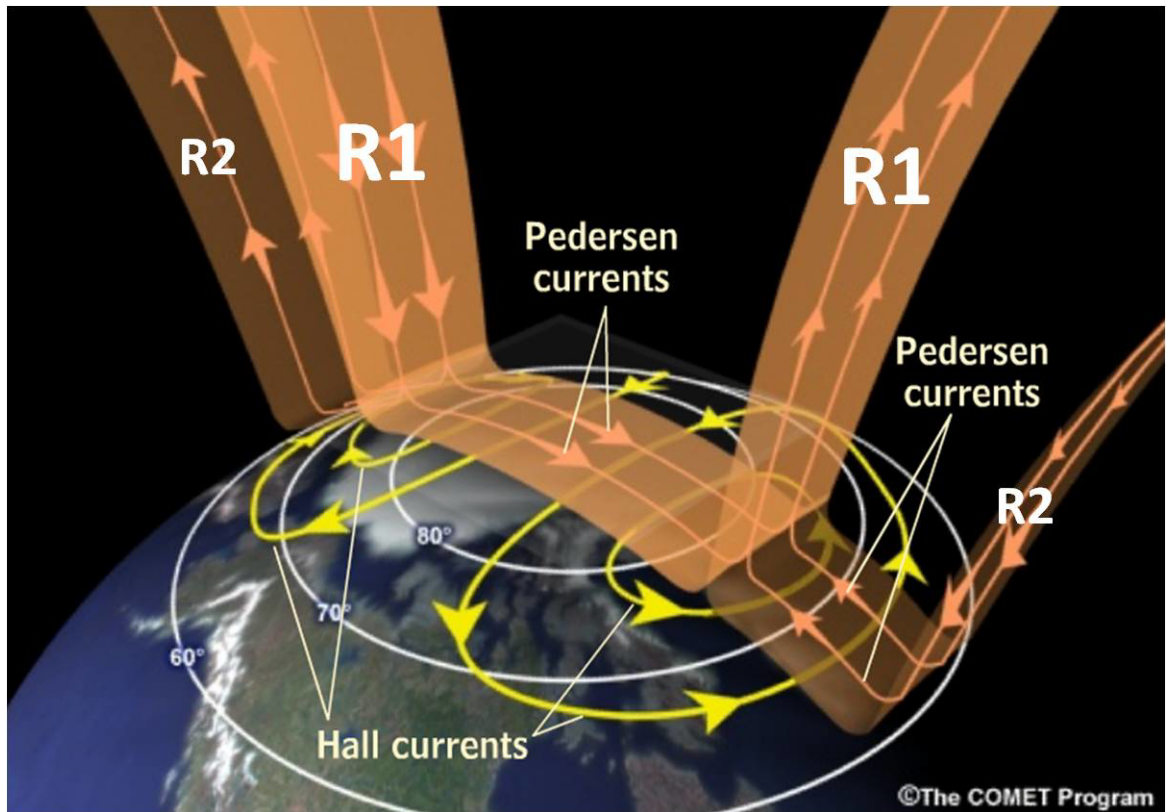
Figure 2.5: A 3-D representation of the Global Scale Current System (Adapted from MedEd, an Teaching and Training Resources for Geoscience Community *https://www.meted.ucar.edu/index.php*).
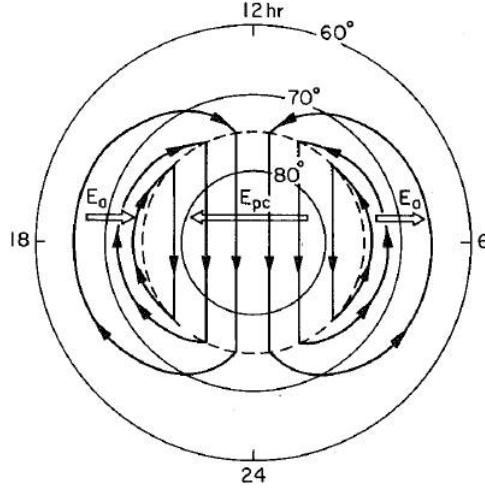
Figure 2.6: Due to the $\mathbf{E} \times \mathbf{B}$ drifts, two-cell convection pattern appears [Heelis et al., 1992, Fig. 6.3 on pp. 267].

2.2.2 Polar Wind Outflow

Polar wind outflow is a fairly constant flow of protons out of the polar cap region. This stream of outflow depletes the lighter charged particles such as H^+ from the high altitude regions thus reducing the electron densities and altering plasma composition. Qualitatively speaking, this is a result of the open magnetospheric geometry in the high latitude regions whereby polar ionosphere is connected to lower pressure tail lobes. As polar wind plasma flows upward, a decrease in collisions frequency allows the charge species to accelerate from the electric field and pressure gradients. At around 2000 to 4000 km altitude, a sufficient amount of energy has been given to each particle, allowing them to achieve escape speed and transporting them well into the magneto tail [Banks and Kockarts, 1973]. Figure 2.7 shows the parallel velocity of H^+ through the collisionless transition region.

14
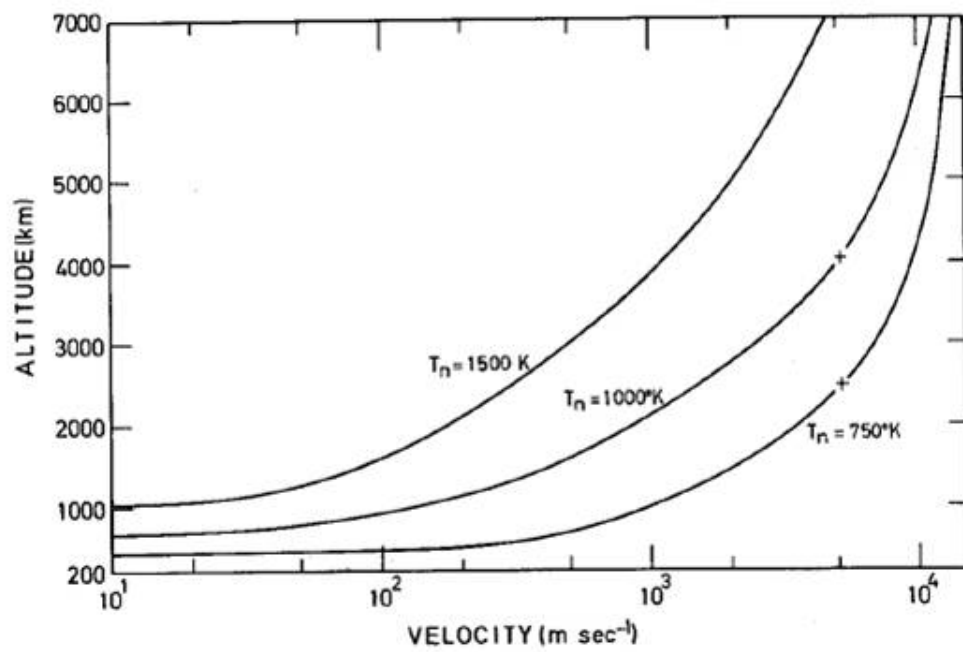
Figure 2.7: Daytime Polar Region H$^+$ Velocity Profiles [Banks and Kockarts, 1973, Fig. 21.12 on pp. 230].
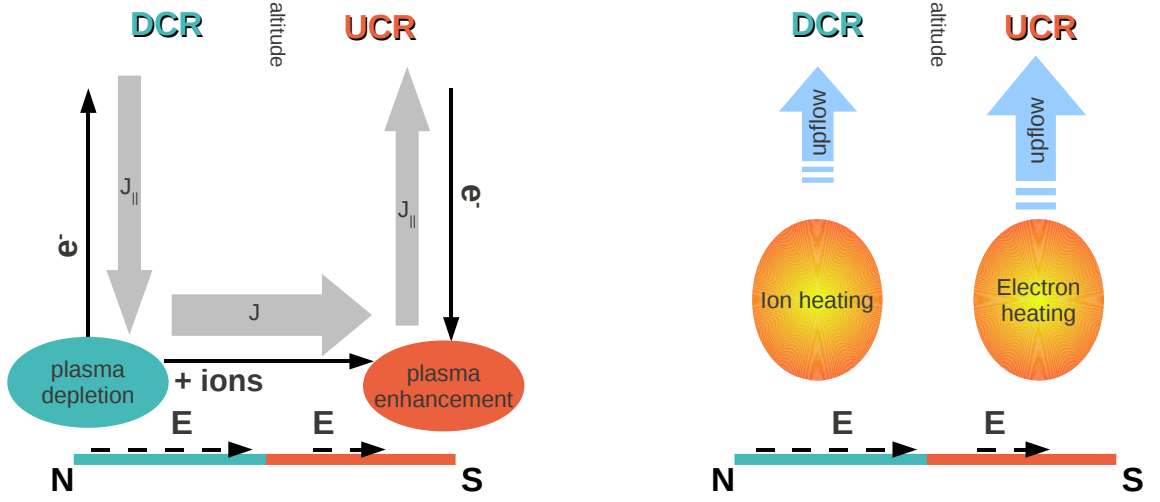
Figure 2.8: Simplistic Illustrations of the Ionospheric Current System (Courtesy of Dr. M. Zettergren).

2.3 Auroral Ionospheric Disturbances

Due to the complex coupling between the ionosphere and magntosphere, disturbances in the auroral regions create ionospheric responses that can be spatially extended and temporally persistent. In this section, we will focus on the smaller scale auroral disturbances. Before we dive into the different processes, we will first focus our attention to a simplified diagram of 2-D auroral ionospheric structure (Figure 2.8).

On the left, when a potential structure is imposed on top of this system, downward current region (DCR) and upward current region (UCR) are formed. Since the electrons have higher mobility than the ions in the parallel direction, they become the main carrier for the current as indicated in Figure (2.8). Based on the quasi-static approximation of the charge continuity equation: $\nabla \cdot \mathbf{J} = 0$, these two current

regions have to be closed. The closure occurs at the lower region (E-region) of the ionosphere where the cross-field conductivity is the highest. This cross-field current is called the Pedersen current. In that region, ions are essentially the only carrier to close the loop, creating plasma depletion (Section 2.3.4) and enhancement (Section 2.3.1) in the DCR and UCR respectively. However, the E-region is highly collisional, and the perpendicular motion of the ions causes them to collide with neutrals, and heat the E-region (Section: 2.3.2). In addition, in the DCR, the combination of the $\mathbf{E} \times \mathbf{B}$ drift and the downward motion of electrons causes the heating which results in upward motion of ions. In contrast, in the UCR, upward moving electrons precipitate energy resulted from the ion-electron collisions. A more quantitative description is discussed in Section 2.3.3.

2.3.1 Plasma Enhancement

At the bottom of the downward current region, the plasma enhancement is due to two important processes: Ion motions due to Pedersen current and electron impact ionization. Electron impact ionization is an important source for creating charged particles:

$$\mathrm{e^-} + \mathrm{O} \Rightarrow 2\mathrm{e^-} + \mathrm{O^+} \tag{2.7}$$
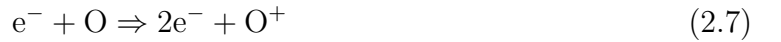
This excitation of the O^+ leads to three different energy states (^4S, ^2P and ^2D). Experiments using Atmosphere Explorer D satellite measured the emissions due to each of these states [Rees et al., 1982]. Analysis have shown the production efficiency of ^2P is around 18 percent [Rees et al., 1982]. This number also confirmed the theoretical calculation by Burnett and Roundtree [1979] using the differential and

17

total cross sections for electron impact ionization of the oxygen gas. Due to the geometry of electric fields, the ions in the E-regions stagnate to further create plasma enhancement. The combination of these two processes can produce an enhancement of around 100 percent. At some point, this stagnation area may expand vertically and reach to the bottom of the F-region [Zettergren and Semeter, 2012].

2.3.2   Frictional Heating

The temperature profile in the high latitude auroral ionopshere is governed by frictional heating between ion and neutral species. As we recall, the motion of the ions is controlled by the $\mathbf{E} \times \mathbf{B}$ drift. As the ions drift along this direction, they encounter neutral species through collisions, these collisions trigger energy and momentum exchange and in turn increase the total energy of the neutral species. A simplified frictional heating rate R_{heat} of a two gas system r and s is described by Banks and Kockarts [1973] as follows:

$$R_{heat} = \nu_{rs}\mu_{rs}n_r\left(\mathbf{v}_s - \mathbf{v}_r\right) \tag{2.8}$$

where ν_{rs} is the reduced mass of the gases, μ_{rs} is the momentum transfer collision frequency, n_r is the density of species "r" and $\mathbf{v}_s$ and $\mathbf{v}_r$ are the drift velocities of the r and s gases.

Figure 2.9 illustrates the temperature profile (solid line) which shows the frictional heating manifested in the E-region and continues to be maintained after reaching a maximum of 2250 K. it also fluctuates between 1250 and 2000 K as altitude gets well into the F-region. The high temperatures are the result of frictional heating. The
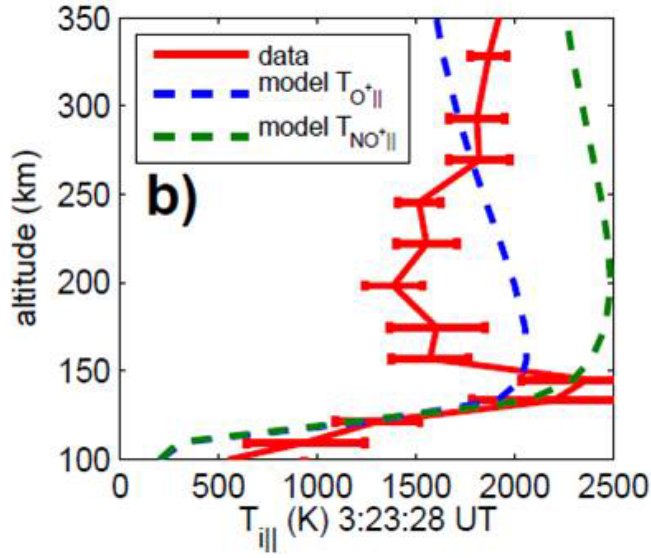
Figure 2.9: Measurements of Frictional Heating and Model Comparison [Zettergren and Semeter, 2010].

data show the ion temperature from the Sondrestrom ISR during an auroral event. The two dotted lines signified data generated using a simple model to simulate the temperature profiles of two primary constituents O^+ and NO^+.

2.3.3   Ion Upflow

In the topside of the high latitude ionosphere, observations have frequently measured the upward flow of ions travelling with high vertical velocities [Su et al., 1999]. For instance, a velocity of approximately 1000 m/s for O^+ has been simulated [Su et al., 1999]. It suggests that there are two main processes that could contribute to the upflow of O^+. The first one is due to the ion frictional heating. As we have mentioned, ion frictional heating occurring in the E-region initiates ion upflow. However, due to the high collisional environment below the F-region, this upflow is suppressed

19

significantly. Once ions reach above 500 km altitude, the decrease in collisions with neutral species allows parallel ion motions resulting in high upflow velocity. We will revisit this process in Chapter 4.

A second contributor of it is due to the electron temperature enhancement driven by electron precipitation. The details of this process are described in Whitteker [1977].

2.3.4 E-Region and F-Region depletion processes

There are two regions of the ionosphere that experience depletion in plasma density. However, the mechanism behind these are completely different. In the E-region, we have depletion due to Pedersen current that advects the ions from the bottom of the DCR to the UCR. This current is mainly determined by two factors: the E-region density or the initial conductivity and the size of the current system. Zettergren and Semeter [2012] illustrate the effects of it by modifying the imposed topside current density. In the F-region however, chemistry is responsible for the depletion. More specifically, the increase in temperature triggers the charge exchange process turning atomic O^+ to molecular ion NO^+. With the high recombination rate of NO^+ with the electrons, it forces the charged particles to be quickly converted into neutral. That in turn creates the depletion in the F-region. In this model illustrated in Figure 2.10 , it makes a comparison of the electron density with and without temperature enhancement. With only the current closure simulated (dashed red line), the depletion only occurs in the E-region. By incorporating the frictional heating process (solid green line), it reveals the depletion of both the E and F regions.
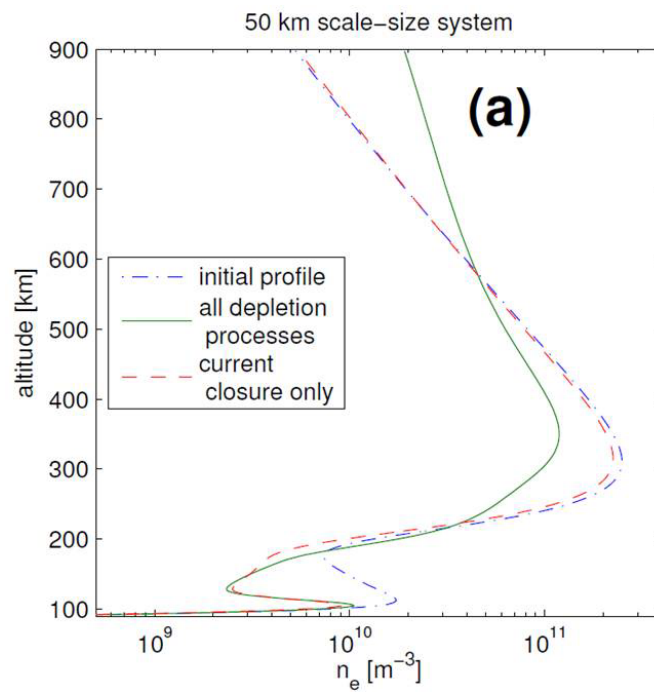
Figure 2.10: Simulation of E and F Regions Depletion [Zettergren and Semeter, 2012].

Chapter 3

Formulation of the Ionospheric Model

3.1 Fluid Moment Formulation

According to Schunk and Nagy [2004], due to the highly non-equilibrium flow conditions and the diverse collisional environment existing in high latitude ionosphere, there have been a number of efforts to model the various flow conditions by using the collison-dominated and collisionless transport equations, kinetic and semi-kinetic models, and macroscopic particle-in-cell techniques. Among them, Boltzmann's equation has the capabilities to demonstrate various flow conditions. In addition, it is also an analytical description of the distribution of the particles. By fusing the areas of electricity and magnetism with the formulation of hydrodynamics, it allows users to simulate different kinds of ionospheric physics. For the purpose of this project, we will focus our attention to three primary state variables: *density, velocity, and en-*

ergy. The basic formulation of the full fluid moment equations are obtained by taking velocity moments of Boltzmann equation. They are expressed as followed:

Density Equation:

$$\frac{\partial n_s}{\partial t} = -\bigtriangledown \cdot (n_s \mathbf{v}_s) + P_s - L_s n_s \tag{3.1}$$

This expression describes the time evolution of density. Essentially, it suggests that there are three different processes that contribute to the density change: particles being advected to a new location via $\mathbf{v}_s$, and productions P_s model or loss L_s via the chemical interactions. (Note, "s" subscript denotes six different ionospheric constituents, they are O^+, NO^+, N_2^+, O_2^+, N^+ and e^-).

Momentum Equation:

$$m_s(\frac{\partial \mathbf{v}_s}{\partial t}) + m_s(\mathbf{v}_s \cdot \bigtriangledown \mathbf{v}_s) = m_s \mathbf{g} - \frac{1}{n_s} \bigtriangledown p_s +$$
$$q_s(\mathbf{E} + \mathbf{v}_s \times \mathbf{B}) + \sum_t m_s \nu_{st}(\mathbf{v}_t - \mathbf{v}_s) \tag{3.2}$$

On the right hand side of this equation, we have the Lorentz's force $q_s(\mathbf{E} + \mathbf{v}_s \times \mathbf{B})$ in addition to the pressure gradient $\frac{1}{n_s} \bigtriangledown p_s$ due to changes in temperature and density. Other forces include gravity $m_s \mathbf{g}$, Coulomb and ion-neutral Collisions $\sum_t m_s \nu_{st}(\mathbf{v}_t - \mathbf{v}_s)$. These forces contribute to the total time rate of change of the drift velocities. This equation closely resembles the Newton's second law: $m_s \mathbf{a} = \mathbf{F}$.

Energy Equation:

$$\frac{\partial T_s}{\partial t} + \mathbf{v}_s \cdot \nabla T_s + \frac{2}{3}T_s(\nabla \cdot \mathbf{v}_s) + \frac{2}{3n_s k_B}\nabla \cdot \mathbf{h}_s =$$
$$-\sum_t \frac{m_s \nu_{st}}{m_s + m_t}[2(T_s - T_t) - \frac{2m_t}{3k_B}(\mathbf{v}_s - \mathbf{v}_t)^2] \tag{3.3}$$

Since we only have three equations with five unknowns ($n_s, \mathbf{v_s}, T_s$, $\mathbf{h}_s$ and p_s, in order to close the system, two additional pieces of information have to be added. The first equation comes from the ideal gas law which relates n_s, T_s and p_s:

$$p_s = k_b n_s T_s, \tag{3.4}$$

where k_b is the Boltzmann's constant.

The second piece of information resolves the heat flux. It is common to express heat flux $\mathbf{h}_s$ for ions and $\mathbf{h}_e$ for electrons using a Fourier's law to capture effects of heat conduction and thermo-electric processes. They are expressed in the following manner:

$$\mathbf{h}_s = -\lambda_s \nabla T_s, \tag{3.5}$$

$$\mathbf{h}_e = -\lambda_e \nabla T_e - \beta_e \mathbf{J}, \tag{3.6}$$

where λ_s and λ_e are the thermal conductivities for ions and electrons respectively. The coefficient β_e measures how much heat is carried per unit charge. Note that the heat flux equation is circumvented in this model through the use of the steady state energy approximation (see Section 3.1.2 for a detailed discussion).

3.1.1 Momentum Balance Approximation

Unlike a direct solution to the momentum equation which illustrates the transient state of the motions of the particles, the momentum balance solution directly gives the equilibrium state of motions. In our model, we deploy this method to calculate the perpendicular drift of ions and parallel drift of electrons. The detailed discussion is deferred until Section 3.2.

To obtain this equation, let's recall equation 3.2 and set the right hand side zero:

$$m_s \mathbf{g} - \frac{1}{n_s} \nabla p_s + q_s(\mathbf{E} + \mathbf{v}_s \times \mathbf{B}) + \sum_t m_s \nu_{st}(\mathbf{v}_t - \mathbf{v}_s) = 0. \tag{3.7}$$

For simplicity, let's rewrite it as followed without the summation and move the drift velocity term $\mathbf{v}_s$, and first consider the perpendicular term $\mathbf{v}_{s\perp}$ That is,

$$\mathbf{v}_{s\perp} \times \mathbf{B} - \frac{m_s \nu_s}{q_s} \mathbf{v}_{s\perp} = \frac{1}{n_s q_s} \nabla p_s - \mathbf{E}_\perp - \frac{m_s \nu_s}{q_s} \mathbf{v}_{n\perp}, \tag{3.8}$$

where $\nu_s \equiv \sum_n \nu_{sn}$ (it only sums over the neutral species).

We can rewrite the left hand side of the equation as follows:

$$\begin{bmatrix} -\frac{m_s \nu_s}{qs} & B_z \\ -B_z & -\frac{m_s \nu_s}{q_s} \end{bmatrix} \begin{pmatrix} v_{sx} \\ v_{sy} \end{pmatrix} = \frac{1}{n_s q_s} \nabla p_s - \mathbf{E}_\perp - \frac{m_s \nu_s}{q_s} \mathbf{v}_{n\perp}. \tag{3.9}$$

By taking the inverse of the coefficient matrix on the LHS, we have,

$$\begin{pmatrix} v_{sx} \\ v_{sy} \end{pmatrix} = \frac{1}{\nu_s^2 + \frac{q_s^2 B^2}{m_s^2}} \frac{q_s^2}{m_s^2} \begin{bmatrix} \frac{m_s \nu_s}{q_s} & B_z \\ -B_z & \frac{m_s \nu_s}{q_s} \end{bmatrix} \cdot \left(\frac{1}{n_s q_s} \nabla p_s - \mathbf{E}_\perp - \frac{m_s \nu_s}{q_s} \mathbf{v}_{n\perp} \right). \tag{3.10}$$

If we recall the gyro-frequency, that is

$$\Omega_s \equiv \frac{q_s B}{m_s}, \tag{3.11}$$

25

The above equation 3.10 can be rewritten as

$$
\begin{pmatrix} v_{sx} \\ v_{sy} \end{pmatrix} = \frac{q_s}{m_s \nu_s} \begin{bmatrix} \frac{\nu_s^2}{\nu_s^2 + \Omega_s^2} & \frac{\nu_s \Omega_s}{\nu_s^2 + \Omega_s^2} \\ -\frac{\nu_s \Omega_s}{\nu_s^2 + \Omega_s^2} & \frac{\nu_s^2}{\nu_s^2 + \Omega_s^2} \end{bmatrix} \cdot \left(\frac{1}{n_s q_s} \nabla p_s - \mathbf{E}_\perp - \frac{m_s \nu_s}{q_s} \mathbf{v}_{n\perp} \right). \quad (3.12)
$$

We can define the coefficient matrix of equation 3.12 as the mobility tensor $\boldsymbol{\mu}_s$ of species:

$$
\boldsymbol{\mu_s} = \frac{q_s}{m_s \nu_s} \begin{bmatrix} \frac{\nu_s^2}{\nu_s^2 + \Omega_s^2} & \frac{\nu_s \Omega_s}{\nu_s^2 + \Omega_s^2} \\ -\frac{\nu_s \Omega_s}{\nu_s^2 + \Omega_s^2} & \frac{\nu_s^2}{\nu_s^2 + \Omega_s^2} \end{bmatrix} \quad (3.13)
$$

We may assume steady state for both the electrons moving in the vertical direction and ions moving in perpendicular directions (A detailed discussion is provided in Section 3.2.1). For the electrons moving parallel to the $B\hat{e}_z$ field, the cross product term becomes zero. Secondly, we can neglect the gravity due to the mass of an electron. By rewriting the collisions (Coulomb and electron-neutral) in term of mobility, it yields the following:

$$
v_{e\parallel} = \mu_{e0}(E_\parallel - \frac{1}{n_e q_e} \nabla_\parallel p_e), \quad (3.14)
$$

where μ_{e0} is the parallel mobility of an electron, and it is expressed as $\nu_{e0} = \frac{q_e}{m_e \nu_e}$.

Perpendicular to the **B** field, high ion Pederson and Hall mobilities indicate that they are the primary charge carriers. Due to ion-neutral collision frequency, perpendicular to **B**, transport of ions can be approximated. By performing the same procedures as before, the following equation is derived:

$$
\mathbf{v}_{s\perp} = \boldsymbol{\mu}_{s\perp} \cdot (\mathbf{E}_\perp - \frac{1}{n_s q_s} \nabla_\perp p_s + \frac{m_s \nu_s}{q_s} \mathbf{v}_{n\perp}). \quad (3.15)
$$

In summary, equations 3.14 and 3.15 can be used in place of the full time dependent momentum equation. The justification of this can found in Section 3.2. It could speed

up the computation process while providing a good approximation for the model. Note that the $v_{s\parallel}$ shall be obtained by solving the fully time dependent moment equation.

3.1.2 Energy Balance Approximation

The Energy Balance approximation can also be used for obtaining the temperature profile. The term $T_s(\bigtriangledown \cdot \mathbf{v}_s)$ represents compressibility of the gas [Saint-Maurice and Hanson, 1982]. Since the ion motion is essentially incompressible, this term can be ignored, and for the purpose of approximation, we can neglect this term. Schunk and Sojka [1982] also examine the effects of heat conduction up to 500km. It suggests that the energy balance is not greatly affected by heat conduction. Therefore, heat conduction term $\bigtriangledown \cdot \mathbf{h}_s$ can also be neglected for solution going up to 500km. All these assumptions allow the use of the energy balance equation by setting:

$$\frac{\partial T}{\partial t} = 0, \tag{3.16}$$

which is essentially the equilibrium temperature to construct the temperature profile.

$$\frac{\partial T_s}{\partial t} = -\sum_t \frac{m_s \nu_{st}}{m_s + m_t} [2(T_s - T_t) - \frac{2m_t}{3k_B}(\mathbf{v}_s - \mathbf{v}_t)^2], \tag{3.17}$$

In addition, due to dense concentration of the neutral species in the low altitude region, the time scale for Coulomb Collisions normally occurs in the order of seconds, much longer than the ion-neutral collisions ($1/\nu_{sn}$). Therefore, we can simply set the left hand-side of the equation zero, and only consider the ion-neutral interactions. We assume that the most ions and neutral particles are all moving at the same velocity in the perpendicular directions.

27

$$T_s - T_n = \frac{\langle m_n \rangle}{3 k_B} (\mathbf{v}_{s\perp} - \mathbf{v}_{n\perp})^2, \tag{3.18}$$

where $\langle m_n \rangle$ is defined as follows:

$$\langle m_n \rangle = \frac{\sum\limits_t \frac{m_t \nu_t}{m_s + m_t}}{\sum\limits_t \frac{\nu_{st}}{m_s + m_t}}. \tag{3.19}$$

Instead of solving the entire energy equation, energy balance provides an approximation to the temperature while greatly reducing both the computational and numerical complexity. In summary, the basic ionospheric transport model would consists the followings:

Density:

$$\frac{\partial n_s}{\partial t} + \bigtriangledown \cdot (n_s \mathbf{v}_s) = P_s - L_s n_s \tag{3.20}$$

Momentum Equation for $v_{s,\|}$:

$$m_s \left(\frac{\partial \mathbf{v}_{\mathbf{s},\|}}{\partial t} \right) + m_s (\mathbf{v}_{\mathbf{s},\|} \cdot \bigtriangledown \mathbf{v}_{\mathbf{s},\|}) = m_s \mathbf{g} - \frac{1}{n_s} \bigtriangledown p_s +$$
$$q_s (\mathbf{E} + \mathbf{v}_{\mathbf{s},\|} \times \mathbf{B}) + \sum_t m_s \nu_{st} (\mathbf{v}_t - \mathbf{v}_{\mathbf{s},\|}) \tag{3.21}$$

Momentum Balance Equation for $v_{s,\perp}$ and $v_{e^-,\|}$:

$$v_{s\perp} = \mu_s \cdot \left(E_\perp - \frac{1}{n_s q_s} \bigtriangledown_\perp p_s + \frac{m_s \nu_s}{q_s} \mathbf{v}_{n\perp} \right) \tag{3.22}$$

$$v_{e\|} = \mu_{e0} \left(E_\| - \frac{1}{n_e q_e} \bigtriangledown_\| p_e \right) \tag{3.23}$$

Energy Balance:

$$T_s - T_n = \frac{\langle m_n \rangle}{3 k_B} (\mathbf{v}_{s\perp} - \mathbf{v}_{n\perp})^2 \tag{3.24}$$

Ideal Gas Law:

$$p_s = k_b n_s T_s \tag{3.25}$$

3.1.3 Numerical Methodology

Even though the momentum balance equations help to reduce the computational complexity, we are still facing the challenge of resolving the parallel momentum equation, and continuity equation in 3D for all ion species. As you recall, these advection equations are nonlinear with complex time and spatially dependent source and sink terms. To resolve these complexity, we propose to use a fractional step method combined with an appropriate finite volume method.

3.1.3.1 Fractional-Step

For our purposes, the fractional step method is to divide the equation into the advection term and the source/sink term. By solving each portion independently, it drastically reduces the numerical complexity, yet still maintains an acceptable first-order accuracy according to LeVeque [2002]. Similar methods have been deployed in many MHD and ionospheric modeling codes. The system is of the following form:

$$\frac{\partial f}{\partial t} + \frac{\partial v_x f}{\partial x} = \Psi(f). \tag{3.26}$$

The basic idea is to solve the homogeneous part to obtain the intermediate solution. We then plug the intermediate solution to the source (sink) term. As an example, consider following continuity equation:

$$\frac{\partial n_s}{\partial t} + \bigtriangledown \cdot (n_s \mathbf{v}_s) = P_s - L_s n_s, \tag{3.27}$$

where

$$\bigtriangledown = \left[\frac{\partial}{\partial x}, \frac{\partial}{\partial y}, \frac{\partial}{\partial z} \right]. \tag{3.28}$$

29

By setting the source term to zero, we have the homogeneous equation.

$$\frac{\partial n_s}{\partial t} + \bigtriangledown \cdot (n_s \mathbf{v}_s) = 0. \tag{3.29}$$

There are a number of methods we can use to calculate the intermediate solution for densities. Let's assume for now that the numerical solution is obtained and denoted by n_s^*, where n_s^* is the intermediate solution. Since the production and loss terms couple different species at each grid, the approach is to compute the $P_{i,j}$ and $L_{i,j}$ using the values to calculate the the effects of source terms (P,L). That is,

$$\frac{dn_s^*}{dt} = P_{i,j} - L_{i,j} n_s^*. \tag{3.30}$$

The solution to equation 3.30 is calculated as:

$$n_s^{n+1} = n_s^* e^{-L_{i,j}^n \Delta t} + \frac{P_{i,j}^n}{L_{i,j}^n} \left(1 - e^{-L_{i,j}^n \Delta t} \right), \tag{3.31}$$

Equation 3.31 gives the solution to equation 3.27 for the next time step.

Similar techniques can also be used for computing the drift velocities. For example, recall the advection portion of the momentum equation.

$$\frac{\partial v_{sz}}{\partial t} + \frac{\partial}{\partial x}(v_{sz}v_{sx}) + \frac{\partial}{\partial y}(v_{sz}v_{sy}) + \frac{\partial}{\partial z}\left(\frac{1}{2}v_{sz}v_{sy} \right) = 0. \tag{3.32}$$

Let's denote the solution to equation 3.32 as the intermediate solution v_{sz}^*. We then combine this solution with the nonhomogeneous part of the full momentum equation 3.21.

For the quantities that increase the velocity, we denote them as the production term. Likewise, all the retarding forces contribute to the loss terms. By only focusing on the $\hat{z}$ direction of the velocities, parallel to B, we have:

$$L_{i,j} = \left(\frac{\partial v_x}{\partial x} + \frac{\partial v_y}{\partial y} - \sum_t \nu_{st} \right) v_{sz}^*,$$

$$P_{i,j} = -g_z - \frac{1}{m_s n_s} \frac{\partial p}{\partial z} + \frac{q_s}{m} E_z + \sum_t \nu_{st} v_{tz}, \tag{3.33}$$

Note that the term $\frac{\partial v_x}{\partial x} + \frac{\partial v_y}{\partial y}$ is relatively smaller than the collision term $\sum_t \nu_{st}$. As a result, the loss term $L_{i,j}$ is always negative.

Then the source and sink step of the total solution would be

$$\frac{dv_{i,j}^*}{dt} = -L_{i,j} v_{i,j}^* + P_{i,j}. \tag{3.34}$$

By using similar approach to solve equation 3.34 analytically to obtain the velocity in the next time step. That is,

$$v_s^{n+1} = v_s^* e^{-L_{i,j}^n \Delta t} + \frac{P_{i,j}^n}{L_{i,j}^n} \left(1 - e^{-L_{i,j}^n \Delta t} \right). \tag{3.35}$$

3.1.3.2 Advection Solution

The Advection equations 3.32 are the hyperbolic systems that can be solved using some very familiar methods such as Lax-Wendroff or Beam-Warming Methods [LeVeque, 2002]. These second-order accurate methods do well in smooth function but fail to give accurate results near sharp gradients (e.g. Step function). However, the ionospheric system can experience various flow conditions which inevitably produce very sharp gradients. One approach to resolving this is to apply a gate or a limiter to control the flux in such a way that it suppresses the oscillations in the discontinuous

portion of the solution but allows resolution of a smooth structure when needed. That is called a slope-limiter method [LeVeque, 2002].

The advection solution is derived from the transport equation in its integral form:

$$\frac{d}{dt} \int_V f d^3 r + \oint_{\partial V} f \mathbf{v_a} \cdot \hat{e}_n da = 0, \tag{3.36}$$

where $\mathbf{v}_a$ is the velocity at which the quantities f such as density, velocity and temperature are advected.

As you can see from equation 3.36, the term $f\mathbf{v}_a$ is the flux. By doting with the surface outward normal direction $\hat{e}_n$, we have the total flux of the above quantities that passes through all the different walls. For the purpose of simple illustration, we decompose the problem in one dimension. That is,

$$f\mathbf{v}_a = \psi \hat{e}_x. \tag{3.37}$$

In discretizing problem spatially, one important assumption we make is that the quantity is being calculated is the cell average which is defined as followings:

$$\overline{f}_i^n = \frac{1}{\Delta x} \int_v f dx, \tag{3.38}$$

where Δx is the length of a cell defined as $\Delta_x = x_{i+1/2} - x_{i-1/2}$.

Since the variation of cell average at each cell $\overline{f}_{i,j,k}$ is a result of the total time average flux calculated from different cell walls at each time step, according to LeVeque [2002], the cell average at the next time step is defined:

$$\overline{f}_i^{n+1} = \overline{f}_i^n - \frac{\Delta t}{\Delta x} \left(\overline{\psi}_{i+1/2}^{n+1/2} - \overline{\psi}_{i-1/2}^{n+1/2} \right), \tag{3.39}$$

where $\overline{\psi}$ is the time average flux defined:

$$\overline{\psi}_{i\pm1/2}^{n+1/2} = \frac{1}{\Delta t} \int\limits_{t_n}^{t_{n+1}} \psi_{i\pm1/2}^{n+1/2} dt. \tag{3.40}$$

By going to half step in the cell grid $i \pm 1/2$ and time step $n + 1/2$, it allows users to achieve second order accuracy in both time and spatial domains, for smooth flows.

In order to allow nonuniform x grid and variable v_x, the general numerical flux function to compute average flux for a slope-limiter method can be obtained from equation 3.40 with advection velocity v_x added. It gives rise to the following expression:

$$\overline{\psi}_{i+1/2}^{n+1/2} = \begin{cases} v_x \overline{f}_{i+1}^{n+1/2} + v_x(x_{i+1/2} - x_i - v_x\Delta t)\sigma_i^{n+1/2} & \text{if } v_x \geq 0 \\ v_x \overline{f}_{i+1/2}^{n+1/2} - v_x(x_{i+1} - x_{i+1/2} + v_x\Delta t)\sigma_{i+1}^{n+1/2} & \text{if } v_x \leq 0 \end{cases} \tag{3.41}$$

Our particular choice of slope is:

$$\sigma_{i-1} = \text{minmod}\left(\left(\frac{\overline{f}_{i+1} - \overline{f}_{i-1}}{x_{i+1} - x_{i-1}}\right), 2\left(\frac{\overline{f}_{i+1} - \overline{f}_i}{x_{i+1} - x_i}\right), 2\left(\frac{\overline{f}_i - \overline{f}_{i-1}}{x_i - x_{i-1}}\right)\right), \tag{3.42}$$

where the *minmod* function is defined in the following:

$$minmod(a, b, c) = \begin{cases} a & \text{if } |a| < |b| \text{ and } ab > 0 \\ a & \text{if } |a| < |c| \text{ and } ac > 0 \\ b & \text{if } |b| < |a| \text{ and } ab > 0 \\ b & \text{if } |b| < |c| \text{ and } bc > 0 \\ c & \text{if } |c| < |a| \text{ and } ac > 0 \\ c & \text{if } |c| < |b| \text{ and } bc > 0 \\ 0 & \text{if } abc \leq 0 \end{cases} \tag{3.43}$$

From equation 3.42, it is shown that there are three different slopes (Centered Slope, Upwind Slope and Downwind Slope) are compared. Depending on the flow, the selection process is controlled by the *minmod* function. This is called the *Monotonic Central-Difference Limiter* (MC limiter) which provides a smooth slope without artificially steepening the continuous functions and provides better resolution to any sharp gradient [LeVeque, 2002]. Figure 3.1 shows a test which makes explicit comparisons among various available limiters: minmod limiter, superbee limiter and MC limiter. As seen, the MC limiter provides a nice compromise between preserving the sharp gradients and maintaining the shape of smooth features.

3.1.3.3 Dimensional Splitting

The advection solver may easily be extended to multiple dimensions LeVeque [2002]. Essentially, we first solve the equation in term of the x variable along the x-direction, then we will use the updated solution to obtain the values along the y direction. Consider 2D advection equation:

$$\frac{\partial f}{\partial t} + A\frac{\partial f}{\partial x} + B\frac{\partial f}{\partial y} = 0. \tag{3.44}$$

Perform dimensional splitting:

$$\text{x-sweeps:} \quad \frac{\partial f}{\partial t} + A\frac{\partial f}{\partial x} = 0, \tag{3.45}$$

$$\text{y-sweeps:} \quad \frac{\partial f}{\partial t} + B\frac{\partial f}{\partial y} = 0. \tag{3.46}$$

According to LeVeque [2002], the errors introduced by this method for many situations may be no worse than the numerical method being used for one-dimensional
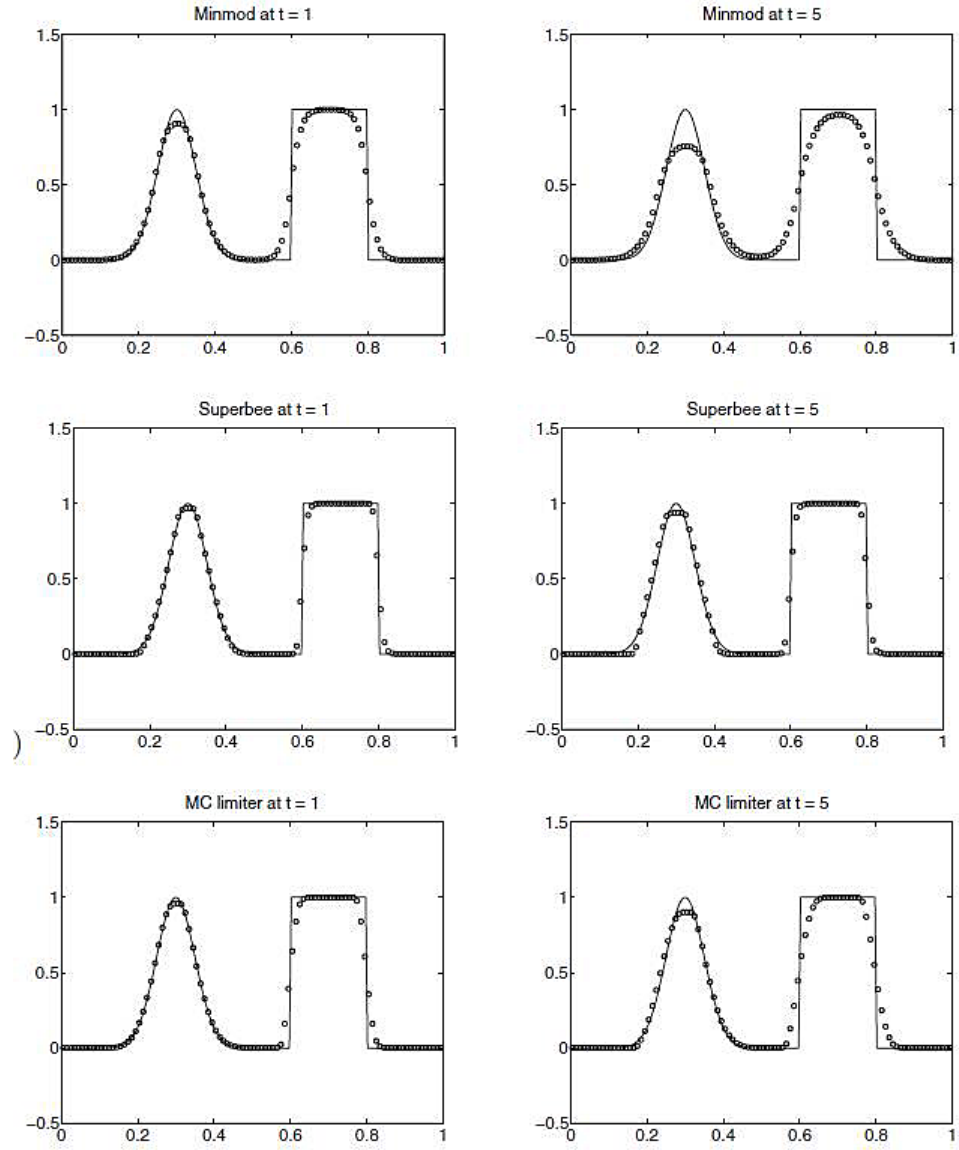
Figure 3.1: A Test on Different High Resolution Methods from [LeVeque, 2002, Fig. 6.2 on pp. 104].

problem. Therefore, it is an excellent technique to reduce numerical complexity while providing an easy algorithm for approaching many multidimensional problems.

3.1.4 Error Analysis

In order to test the accuracy of the advection solver, we can compare it against a problem with known solution. Figure 3.2 and 3.3 show a graphical comparison between a analytical solution and the numerical solution for solving a simple 3-D advection problem with the form

$$\frac{\partial f}{\partial t} + \mathbf{v} \cdot \nabla f = 0, \tag{3.47}$$

with an initial condition of $f(x, y, z, t_0)$, the solution becomes

$$f(x, y, z, t) = f(x - v_x t, y - v_y t, z - v_z t, t_0). \tag{3.48}$$

The numerical methodology uses both the MC Slope Limiter method and the dimensional splitting. For initial condition, we use a 3-D Gaussian distribution.

$$f(x, y, z) = e^{-\left[\frac{(x-a)^2}{\sigma_x^2} + \frac{(y-b)^2}{\sigma_y^2} + \frac{(z-c)^2}{\sigma_z^2}\right]} \tag{3.49}$$

With advection velocities of $v_x = 2$ ms^{-1}, $v_y = 8$ ms^{-1} and $v_z = 16$ ms^{-1}, this initial condition is started in the middle of the box (10m x 10m x 10m with $dx = dy = dz = 0.1$ m grid points) and propagates diagonally on a particular $x - y$ plane. The corresponding analytical solution is:

$$f(x, y, z, \mathbf{v}, t) = e^{-\left[\frac{(x-v_x t-a)^2}{\sigma_x^2} + \frac{(y-v_y t-b)^2}{\sigma_y^2} + \frac{(z-v_z t-c)^2}{\sigma_z^2}\right]}. \tag{3.50}$$

In this exercise, we use the Courant-Friedrichs-Lewy (CFL) stability defined in equation 3.51 to determine the time step. To be conservative, we use CFL = 0.5 to ensure numerical stability, For one dimension, we have:

$$\text{CFL}_x = \frac{v_x \Delta t}{\Delta x}. \tag{3.51}$$

This allows us to obtain Δt for the next step. In a 3-D problem, each direction is calculated and compared with others. By selecting the minimum value, it is then used to compute the next time step.

From Figures 3.2 and 3.3, the numerical methodology we are proposing here has an outstanding performance at preserving the shape of the function as it propagates. This feature is essential for the model. In addition, we can clearly see that there is an acceptable amount of numerical diffusion occurring. In the third row of each figure, at the leading edge, the numerical technique underestimated the values as it adjusting the slope in order to optimize the flux approximation. Similarly, at the trailing edge, the numerical technique overestimated the value for the same purpose. However, considering of using both the dimensional splitting and MC slope limiter, achieving the relative differences of between 4 to 6 percent indicates that such a numerical construct could provide confident results.

3.1.5   Implementation of Fluid Solver

The implementation can be described as follows: The program first obtains the velocities from the momentum balance approximation for different species. The data then is fed to the full parallel momentum equation. By invoking the Operational Splitting, we obtain the final parallel drift velocities for all species. The data is routed to
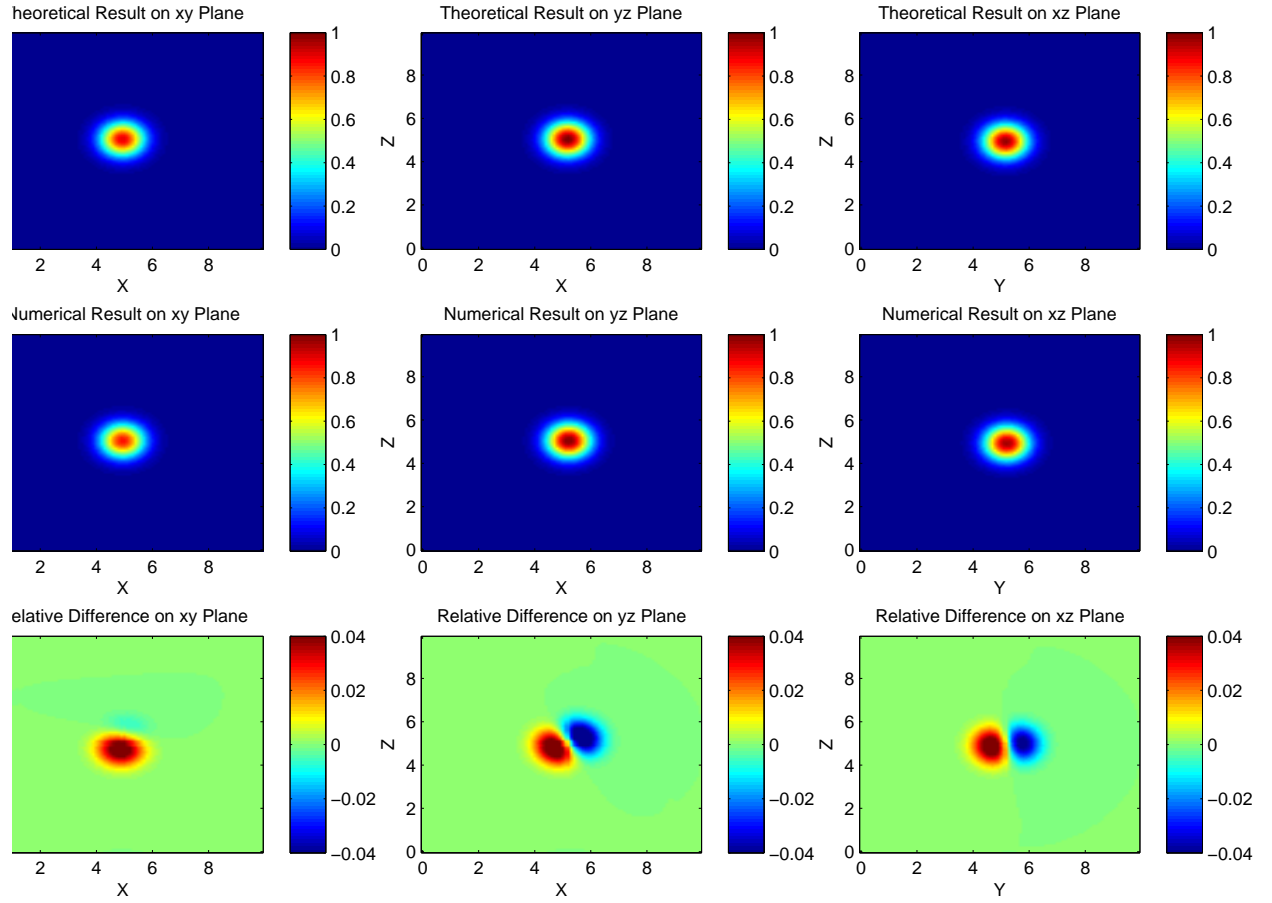
Figure 3.2: A comparison of Analytical and Numerical Solutions at t = 0.0028 second (the 1st Time Step).
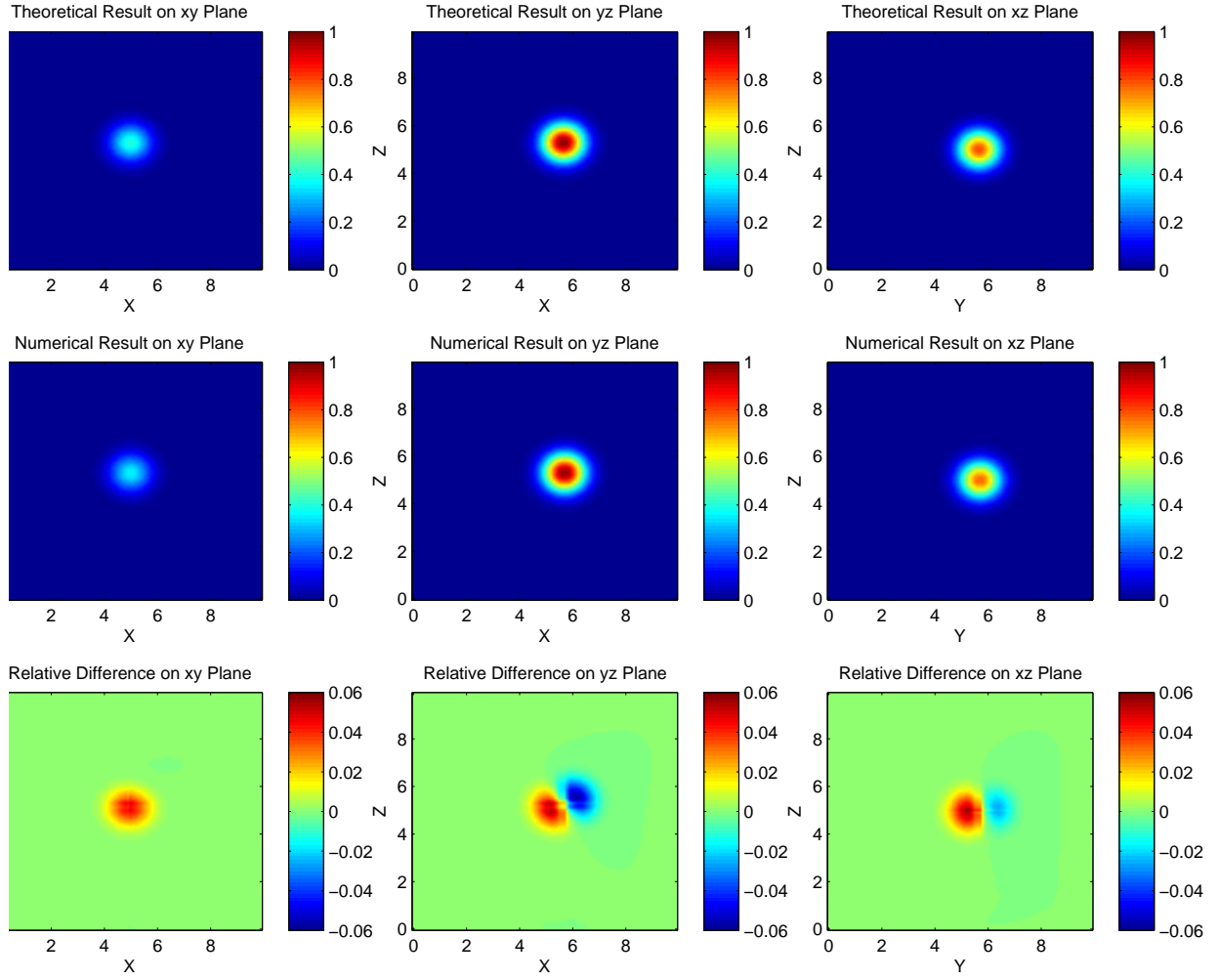
Figure 3.3: A comparison of Analytical and Numerical Solutions at t = 0.0528 second (the 19th Time Step).
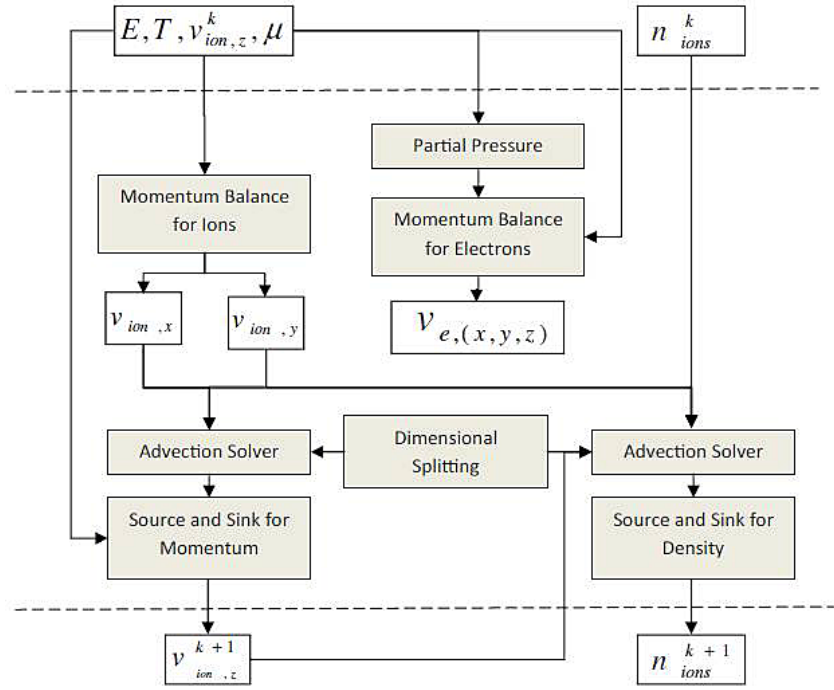
Figure 3.4: Synthesis of Transport Model.

the density calculation. The block diagram in Figure 3.4 illustrates the sequence of processes for one time step of fluid solver.

3.2 Ionospheric Electrodynamics

In order to construct the complete picture of the interactions within the ionosphere, it is necessary to specify $\mathbf{E}$ and $\mathbf{B}$ for mobility tensor in equation 3.1.2. In this work, the $\mathbf{B}$ comes directly from the geomagnetic field. Therefore, our primary objective is to study the characteristics of electric fields and currents in the ionosphere, and how they relate to the transports of various particles and the associated energy exchange processes. Theoretical formulations are then introduced, and the associated numerical approaches are presented, followed by a discussion of implementation.

3.2.1 Electrostatic Approximation

The most intuitive approach to obtain $\mathbf{E}$ field is to use the Gauss's Law with the electrostatic assumption, which states:

$$\nabla^2 \Phi = -\frac{\rho_c}{\epsilon_0}. \tag{3.52}$$

However, the charge density is rather unknown to our problem. Therefore, it is not advisable to obtain the potential solution using equation 3.52. However, another approach deploying the electrostatic approximation is suggested by Zettergren and Semeter [2012], which allows us to obtain electric potential without knowing the charge distribution.

We start with the conservation for density from equation 3.1. If we define the boundaries of a small volume, the change in charge density corresponds to the differences between the charges flowing in and out of the control surface of this volume. If we detect a decrease of charge density inside this volume, it corresponds to a scenario

where more charges are leaving the volume than coming in. The currents considered in this work are steady and thus the system is characterized by no change in the net charge density anywhere in space [Jackson, 1991]: That is,

$$\frac{\partial \rho_c}{\partial t} = 0. \tag{3.53}$$

Since we are mostly concerned with the final electrostatic state of the problem, we can neglect the transient state of charge interactions. In general, the decay constant for this transient state is in the order of 10^{-3} sec or smaller, compared to our much longer time step (10^{-1} sec). By doing so, we transform our problem into a final state boundary value problem where initial charge density can be neglected.

By substituting this condition into the continuity equation for charge conservation,

$$\nabla \cdot \mathbf{J} = -\frac{\partial \rho}{\partial t}. \tag{3.54}$$

By neglecting displacement current in the magnetostaic limit, we obtain the following important equation for current density:

$$\nabla \cdot \mathbf{J} = 0. \tag{3.55}$$

In order to use this important relation, recall the definition of current density:

$$\mathbf{J} = \sum_s n_s q_s \mathbf{v}_s. \tag{3.56}$$

The current density consists of the parallel and perpendicular terms. These two terms are governed by the motions of different species. In the perpendicular direction, the currents are conveyed by the motions of the ions. To calculate the

motions, the momentum balance approximation can be used because the electrons have much higher parallel mobility along the field line compared to the ions moving in the same direction. That makes the electrons the dominant charge carriers. As a result, the electrons can attain a steady-state relatively quickly compared to the ion species. In other words, the electrons have already achieved the equilibrium state while the ions are still in the transient state. Therefore, we can use the momentum balance equations for ions to resolve the $\mathbf{J}_\perp$. That is,

$$\mathbf{v}_{s\perp} = \boldsymbol{\mu}_{s\perp} \cdot (\mathbf{E}_\perp - \frac{1}{n_s q_s} \nabla_\perp p_s + \frac{m_s \nu_s}{q_s} \mathbf{v}_{n\perp}). \tag{3.57}$$

Similarly, the parallel current is mainly carried by the flow of the electrons. The momentum balance approximation is applied, and the expression is as follows:

$$v_{e\parallel} = \mu_{e0}(E_\parallel - \frac{1}{n_e q_e} \nabla_\parallel p_e). \tag{3.58}$$

The introduction of these equations give rise to the expression of currents in terms of electric field, motions of the neutral winds and pressure gradients:

$$\mathbf{J}_\perp = \boldsymbol{\sigma}_\perp \cdot \mathbf{E}_\perp + \sum_s n_s m_s \nu_s \boldsymbol{\mu}_{s\perp} \cdot \mathbf{v}_{n\perp}, \tag{3.59}$$

the term $\sum_s n_s m_s \nu_s \boldsymbol{\mu}_{s\perp} \cdot \mathbf{v}_{n\perp}$ is the current driven by the neutral-ion coupling. The effects of this can create a significant response in the E region of the ionosphere (details are described in Section 5.2). By deploying the same approach, we can obtain the expression field-aligned current density:

$$J_\parallel = \sigma_0 E_\parallel - \mu_{e0} \nabla_\parallel p_e. \tag{3.60}$$

The electric field can be separated into two components: the ambient electric field/ambipolar electric field due to the pressure gradient E_a, and the response field

43

E_r enforced by the imposed electric potential at the boundaries and by any charge accumulation in the system. The sum of these two electric fields forms the total electric field:

$$\mathbf{E} = \mathbf{E}_a + \mathbf{E}_r. \tag{3.61}$$

Since we ignore the pressure gradient for the ion species, we only consider the ambipolar electric field parallel to $\mathbf{B}$ field. To obtain it, we simply zero out the current density from equation 3.60. The resultant electric field would be the ambipolar electric fields:

$$E_{a\parallel} = \frac{\mu_{e0} \, \nabla_\parallel \, p_e}{\sigma_0}. \tag{3.62}$$

After substituting the above expressions back to equations 3.59 and 3.60, the result gives us a very simple expression for current density in term of the response electric field $\mathbf{E}_r$

$$\mathbf{J}_\perp = \boldsymbol{\sigma}_\perp \cdot \mathbf{E}_{\mathbf{r}\perp} + \sum_s n_s m_s \nu_s \boldsymbol{\mu}_{\boldsymbol{s}\perp} \cdot \mathbf{v}_{n\perp}, \tag{3.63}$$

$$J_\parallel = \sigma_0 E_{r\parallel}. \tag{3.64}$$

A more compact expression is

$$\mathbf{J} = \boldsymbol{\sigma} \mathbf{E}_r + \sum_s n_s m_s \nu_s \boldsymbol{\mu}_{\boldsymbol{s}\perp} \cdot \mathbf{v}_{n\perp}, \tag{3.65}$$

where $\boldsymbol{\sigma}$ describes the anisotropic conductivity of plasma, and it is closely related to the density, gyro frequency and collision frequency of the each species. They are written as follows:

$$\boldsymbol{\sigma} = \begin{bmatrix} \sigma_P & -\sigma_H & 0 \\ \sigma_H & \sigma_P & 0 \\ 0 & 0 & \sigma_0 \end{bmatrix} = \begin{bmatrix} \sum_s \frac{q_s^2 n_s}{m_s \nu_s} \frac{\nu_s^2}{\nu_s^2 + \Omega_s^2} & \sum_s \frac{q_s^2 n_s}{m_s \nu_s} \frac{\nu_s \Omega_s}{\nu_s^2 + \Omega_s^2} & 0 \\ -\sum_s \frac{q_s^2 n_s}{m_s \nu_s} \frac{\nu_s \Omega_s}{\nu_s^2 + \Omega_s^2} & \sum_s \frac{q_s^2 n_s}{m_s \nu_s} \frac{\nu_s^2}{\nu_s^2 + \Omega_s^2} & 0 \\ 0 & 0 & \sum_s \frac{n_s q_s^2}{m_s \nu_s} \end{bmatrix}. \quad (3.66)$$

There are three distinctive conductivities that describe the conductivities in the $\mathbf{E}_\perp$ direction (Pedersen Conductivity σ_P), $\mathbf{E} \times \mathbf{B}$ (Hall conductivity σ_H) and the field aligned (Parallel Conductivity σ_0) direction.

Finally, the electrostatics approximation is invoked:

$$\nabla \times \mathbf{E_r} = 0, \quad (3.67)$$

which gives

$$\mathbf{E} = -\nabla \Phi. \quad (3.68)$$

Incorporating equation 3.68, the Ohm's law 3.65 with quasistatic approximation, the measurable quantity Φ can be calculated with neutral winds via the following relation:

$$\nabla \cdot (\boldsymbol{\sigma} \cdot \nabla \Phi) = \nabla_\perp \cdot \left(\sum_s n_s m_s \nu_s \boldsymbol{\mu_{s\perp}} \cdot \mathbf{v}_{n\perp} \right). \quad (3.69)$$

By expanding this expression, it yields the following algebraic expression:

$$A \frac{\partial^2 \Phi}{\partial x^2} + B \frac{\partial^2 \Phi}{\partial y^2} + C \frac{\partial^2 \Phi}{\partial z^2} + D \frac{\partial \Phi}{\partial x} + E \frac{\partial \Phi}{\partial y} + F \frac{\partial \Phi}{\partial z} = G, \quad (3.70)$$

with:

$$
\begin{aligned}
A &= \sigma_P \\
B &= \sigma_P \\
C &= \sigma_0 \\
D &= \left(\frac{\partial \sigma_P}{\partial x} + \frac{\partial \sigma_H}{\partial y} \right) \\
E &= \left(\frac{\partial \sigma_P}{\partial y} - \frac{\partial \sigma_H}{\partial x} \right) \\
F &= \frac{\partial \sigma_0}{\partial z} \\
G &= \sum_s n_s m_s \nu_s \left[\frac{\partial}{\partial x} (\mu_{sP} v_{nx} - \mu_{sH} v_{ny}) + \frac{\partial}{\partial y} (\mu_{sH} v_{nx} + \mu_{sP} v_{ny}) \right].
\end{aligned}
$$

$$(3.71)$$

It is beyond hope to obtain any analytical solution due to the complex spatial variance of different conductivities in ionosphere. Therefore, numerical routines are utilized to obtain an approximate potential solution.

3.2.2 Finite Difference Equation (F.D.E.)

Elliptic PDEs are most commonly solved via finite difference methods. As usual, the equation is obtained by first expressing any continuous function in term of the *Taylor Series Expansion*:

$$
f(x + \Delta x) = f(x) + f'(x)\Delta x + f''(x)\frac{\Delta x^2}{2!} + f'''(x)\frac{\Delta x^3}{3!} + H.O.T, \quad (3.72a)
$$

$$
f(x - \Delta x) = f(x) - f'(x)\Delta x + f''(x)\frac{\Delta x^2}{2!} - f'''(x)\frac{\Delta x^3}{3!} + H.O.T. \quad (3.72b)
$$

In order to obtain the first derivative, we can subtract equation (a) from (b) and neglect higher order terms. It yields the following in uniform Δx:

$$f'(x) = \frac{f(x + \Delta x) - f(x - \Delta x)}{2\Delta x} = \frac{f_{i,j+1,k} - f_{i,j-1,k}}{2\Delta x}. \tag{3.73}$$

Likewise, adding (a) and (b) yields the second derivative,

$$f''(x) = \frac{f(x + \Delta x) - 2f(x) + f(x - \Delta x)}{\Delta x^2} = \frac{f_{i,j+1,k} - 2f_{i,j,k} + f_{i,j-1,k}}{\Delta x^2}. \tag{3.74}$$

The same methdology applies to obtain the first and second derivative in the uniform Δy. For non-uniform grid z-direction however, the expression is as followed:

$$f'(z) = \frac{f(z + \Delta z_+) - f(z - \Delta z_-)}{\Delta z_+ + \Delta z_-} = \frac{f_{i,j,k+1} - f_{i,j,k-1}}{\Delta z_+ + \Delta z_-}. \tag{3.75}$$

By subtracting (b) from (a) yields the second derivative,

$$\begin{aligned} f''(z) &= \frac{2\Delta z_+ f(z - \Delta z_-) - 2(\Delta z_- + \Delta z_+)f(z) + 2\Delta z_- f(z + \Delta z_+)}{\Delta z_+ \Delta z_-^2 + \Delta z_- \Delta z_+^2} \\ &= \frac{2\Delta z_+ f_{i,j,k-1} - 2(\Delta z_- + \Delta z_+)f_{i,j,k} + 2\Delta z_- f_{i,j,k+1}}{\Delta z_+ \Delta z_-^2 + \Delta z_- \Delta z_+^2}. \end{aligned} \tag{3.76}$$

Full expansion of 3.70 in term of F.D.E is written as followed:

$$\begin{aligned} A\left(\frac{f_{i,j+1,k} - 2f_{i,j,k} + f_{i,j-1,k}}{\Delta x^2}\right) + B\left(\frac{f_{i+1,j,k} - 2f_{i,j,k} + f_{i-1,j,k}}{\Delta y^2}\right) + \\ 2C\left[\frac{\Delta z_+ f_{i,j,k-1} - (\Delta z_- + \Delta z_+)f_{i,j,k} + \Delta z_- f_{i,j,k+1}}{\Delta z_+ \Delta z_-^2 + \Delta z_- \Delta z_+^2}\right] + \\ D\left(\frac{f_{i,j+1,k} - f_{i,j-1,k}}{2\Delta x}\right) + E\left(\frac{f_{i+1,j,k} - f_{i-1,j,k}}{2\Delta y}\right) + \\ F\left(\frac{f_{i,j,k+1} - f_{i,j,k-1}}{\Delta z_+ + \Delta z_-}\right) = G_{i,j,k}. \end{aligned} \tag{3.77}$$

By collecting terms for all the neighboring points, it yields,

$$\xi^1_{i,j,k} f_{i-1,j,k} + \xi^2_{i,j,k} f_{i,j,k} + \xi^3_{i,j,k} f_{i+1,j,k} + \xi^4_{i,j,k} f_{i,j-1,k} + \xi^5_{i,j,k} f_{i,j+1,k} +$$

$$\xi^6_{i,j,k} f_{i,j,k+1} + \xi^7_{i,j,k} f_{i,j,k-1} = G_{i,j,k}, \quad (3.78)$$

where $\xi_{i,j,k}$ are the coefficients for the grid points. They consist of both the conductivities and the spatial information. This finite difference method allows us to construct a linear system as followed:

$$\begin{bmatrix} \xi^1_{i,j,k} & \xi^2_{i,j,k} & \xi^3_{i,j,k} & \xi^4_{i,j,k} & \xi^5_{i,j,k} & \xi^6_{i,j,k} & \xi^7_{i,j,k} \end{bmatrix} \begin{bmatrix} f_{i-1,j,k} \\ f_{i,j,k} \\ f_{i+1,j,k} \\ f_{i,j-1,k} \\ f_{i,j+1,k} \\ f_{i,j,k-1} \\ f_{i,j,k+1} \end{bmatrix} = G_{i,j,k} \quad (3.79)$$

Equation 3.79 represents a solution at each grid point $f_{i,j,k}$ as it cycles through the entire system. It can also be written as a matrix system:

$$\mathbf{Mf} = \mathbf{G}. \quad (3.80)$$

Each row of the coefficient matrix is constructed based on the geometrical location of the grid location. It must also take into account of the edges, corners and the method of sweeping (In this project, the order of sweep is $y \to x \to z$. These

subtleties have to be borne in mind while constructing the coefficient matrix. In the next section, we will discuss how each boundary condition can be implemented based on such a mathematical construct.

3.2.3 Dirichlet and Neumann Boundary Conditions

In the situation where the electric potential is specified at the boundaries, the approach is simple. When the system is sweeping near the boundary, the $f_{i,j,k}$ are already specified. Therefore, the values are known and can simply be moved to the right hand side of the equation 3.80. For example, as we sweep along the left-side of the boundary, all the $f_{i,j-1,k}$ are known. Therefore, the linear system 3.79 can be written as:

$$
\begin{bmatrix} \xi^{1}_{i,j,k} & \xi^{2}_{i,j,k} & \xi^{3}_{i,j,k} & 0 & \xi^{5}_{i,j,k} & \xi^{6}_{i,j,k} & \xi^{7}_{i,j,k} \end{bmatrix}
\begin{bmatrix} f_{i-1,j,k} \\ f_{i,j,k} \\ f_{i+1,j,k} \\ f_{i,j-1,k} \\ f_{i,j+1,k} \\ f_{i,j,k-1} \\ f_{i,j,k+1} \end{bmatrix}
= G_{i,j,k} - \begin{bmatrix} 0 \\ 0 \\ 0 \\ \xi^{4}_{i,j,k} f_{i,j-1,k} \\ 0 \\ 0 \\ 0 \end{bmatrix}
\tag{3.81}
$$

As shown, the term where the values have been given are zeroed out and moved to the right hand side of the equation with the coefficients. Similar approaches can be applied for the other boundaries.

For the situation when we encounter the Neumann boundary condition, we only consider the situation when

$$
\frac{\partial \Phi}{\partial x} \Big|_{x=BC} = 0.
\tag{3.82}
$$

As an example, let's consider the left side of the boundary $x = 0$. We can rewrite this in the finite difference form as followed:

$$\frac{f_{i,j,k} - f_{i,j-1,k}}{\Delta x} = 0. \tag{3.83}$$

We can first rewrite the x component of the finite difference equation 3.77 as follows:

$$A\left(\frac{f_{i,j+1,k} - f_{i,j-1,k} - f_{i,j-1,k} + f_{i,j-1,k}}{\Delta x^2}\right) +$$
$$\ldots + D\left(\frac{f_{i,j+1,k} - f_{i,j,k} + f_{i,j,k} - f_{i,j-1,k}}{2\Delta x}\right) + \ldots = G_{i,j,k}. \tag{3.84}$$

We then substitute the condition 3.83 in equation 3.84 which yields the following FDE for grid points $f_{i,j,k}$ at the x=1 plane next to a Neumann boundary at the x=0 plane .

$$A\left(\frac{f_{i,j+1,k} - f_{i,j,k}}{\Delta x^2}\right) + \ldots + D\left(\frac{f_{i,j+1,k} - f_{i,j,k}}{2\Delta x}\right) + \ldots = G_{i,j,k}. \tag{3.85}$$

Similar approaches can be used for all the different sides, edges and corners by clearly identifying the terms required to be zero. For any nonzero gradient at the Neumann boundaries, the same approach can be used which only requires slight modifications to equation 3.85.

Regardless of the boundary conditions, it is inevitable that we are encountering a large linear system. In the next section, we will focus our attention to the methods that are generally used for solving large sparse matrix systems.

3.2.4 Iterative Solver

Normally, our system uses 100x100x128 size which consists of 1.28 millions data points. That means that the size of the coefficient matrix is 1.28 million by 1.28 million. The general approach of using direct inverse method would requires a huge storage for performing matrix inversion. Solving a matrix of this size requires the use of an iterative method and sparse storage approach. Normally, there are two major categories of iterative methods: stationary and nonstationary methods. The Jacobi Method, Gauss-Seidel Method and SOR (Succesive Overrelaxation) method are the well-known examples in the stationary iterative category. They are simple to implement but slow and ineffective when we attempt to solve a large matrix system. In order to understand the reasons for this, we can first express the general recursion relation for any iterative methods:

$$x^{n+1} = Bx^n + c. \tag{3.86}$$

Both B and c are critical to the rate of convergence. In the stationary method, since these two values are fixed during each iteration, their performance on convergence and effectiveness can be greatly reduced. Therefore, nonstationary methods have been developed to improve the performance.

Unlike the stationary method, the recursion relation for a nonstationary method has additional variables based upon the iterations to optimize the rate of convergence. Normally, it is expressed as followed:

$$x^{n+1} = x^n + \alpha_n p^n. \tag{3.87}$$

The term $\alpha_n p^n$ is the search vector for the optimal approximated solution. α_n gives the magnitude of this vector and p^n provides directions. Based on the residuals after from the previous time step, the search vector is updated to optimize the rate of convergence.

According to Barrett et al. [1994], selecting the best iterative method for a particular application is largely a matter of trial and error. Table 3.1 reports the result of a test of solving a Laplace's Equation with 50x50x50 grid points running on a 3.10 GHz Intel Xeon CPU with Linux Operating System. Evidently, the CGS method takes the least amount of time with relatively small number of iterations to achieve the solution.

However, we are encountering a large system that is at least 200 times bigger than this test scenario. Therefore, solely relying on the iterative method is not enough. Another special technique that can boost the performance is called the preconditioning. It is a numerical process that transforms any coefficient matrix into a new matrix with more favorable spectral properties which is most commonly defined as the rate of convergence. The rate of convergence for any linear system is determined by the condition number which measures how much the system would react to small changes in the argument. We usually label those that have low condition numbers to be well-conditioned and high condition numbers to be ill-conditioned. Hence, the purpose of this method is to decrease the condition number, which increases the rate of convergence. The basic idea is to multiply it with the conditioning matrix. For example,

Method	Time (sec)	Iterations
Quasi-minimal Residual Method	0.172	36
Conjugate Gradients Square	0.144	28
Biconjugate Gradient Method	0.165	37
LSQR	0.212	167
Transpose-Free Quasi-Minimal Residual Method	0.152	26

Table 3.1: A Comparison of Different Iterative Methods.

$$M^{-1}Ax = M^{-1}b. \tag{3.88}$$

That trick is to make the quantity $M^{-1}A$ exhibit favorable spectral properties which ease the burden on the iterative method.

After looking into a number of preconditioning methods, the team decided to use *LU Incomplete Factorization* for this project. Due to the scope of this project, the mechanism behind this method will not be discussed here. Barrett et al. [1994] and Saad [1996] have extensive discussions on this. Table 3.1 shows the performance of different non-stationary methods without using LU Incomplete Factorization. With the LU Incomplete Factorization, the number of iterations can be reduced by 5 to 10 times. However, the LU Incomplete also incurs additional computational costs. Therefore, it is also a trial and error process to obtain an optimal combination.

Conditions	Analytical and Numerical
B.C.	All Dirichlet
Imposed B.C. Value	Constant Value of 1
Grid Size	$dx = dy = dz = 1$
Domains	20x20x20

Table 3.2: Initial Setup.

3.2.5 Error Analysis

The Laplace's Equation can be obtained from our system by assuming the conductivities to be unity, and to set all the first derivative terms to zero. By doing so, it allows us to test the model against analytical solutions. In the following example, we will use the solution 3.89 provided by Jackson [1991, Problem 2.23, pp. 92] and compare it against our numerical solution. Table 3.2 lists the setup of this problem.

$$\Phi(x, y, z) = \sum_{m,n} A_{mn} sin\left(\frac{n\pi}{a}x\right) sin\left(\frac{m\pi}{a}y\right) \left(e^{\gamma z} - e^{-\gamma z + 2\gamma a}\right), \tag{3.89}$$

where

$$\gamma_{mn} = \left[\left(\frac{n\pi}{a}\right)^2 + \left(\frac{m\pi}{a}\right)^2\right]^{0.5}. \tag{3.90}$$

In the analytical solution, 26 terms in the series are used to compute the approximate potential solution. Figure 3.5 demonstrates a side-by-side comparison between the analytical solution and numerical solution. The size of the system is 20x20x20. More detailed analysis demonstrated in Figure 3.6 shows the average error at each
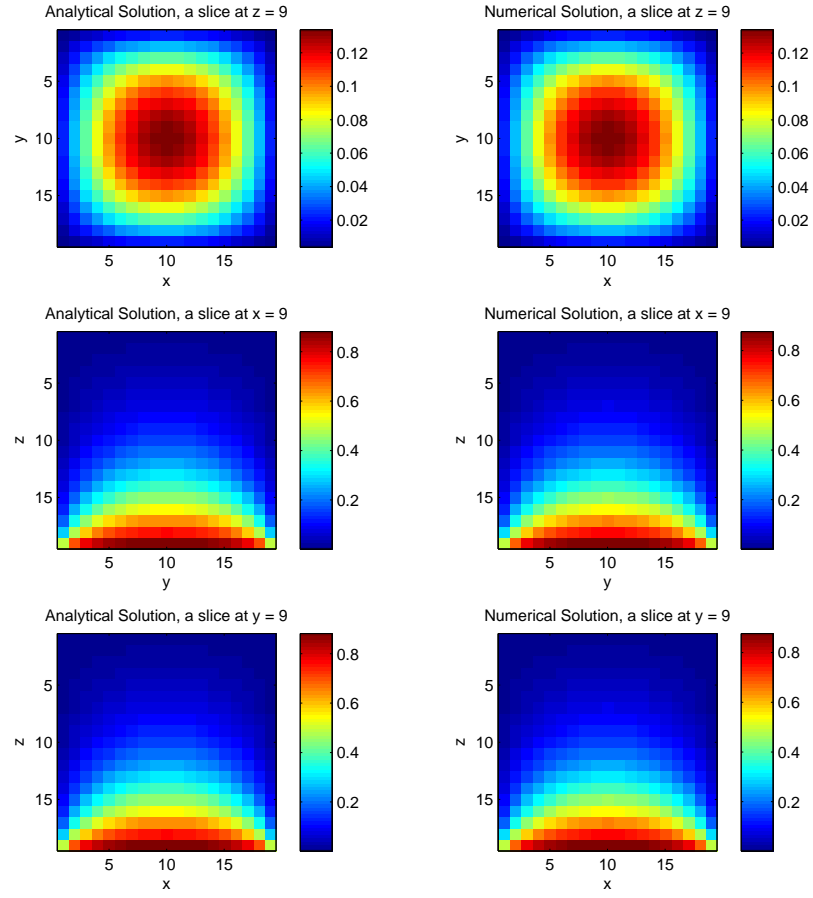
Figure 3.5: Performance of the Numerical Φ Solver.

discrete point of z. With a relative error of approximately 0.9 percent, the second order finite difference method performs quite well for calculating the electric potential.
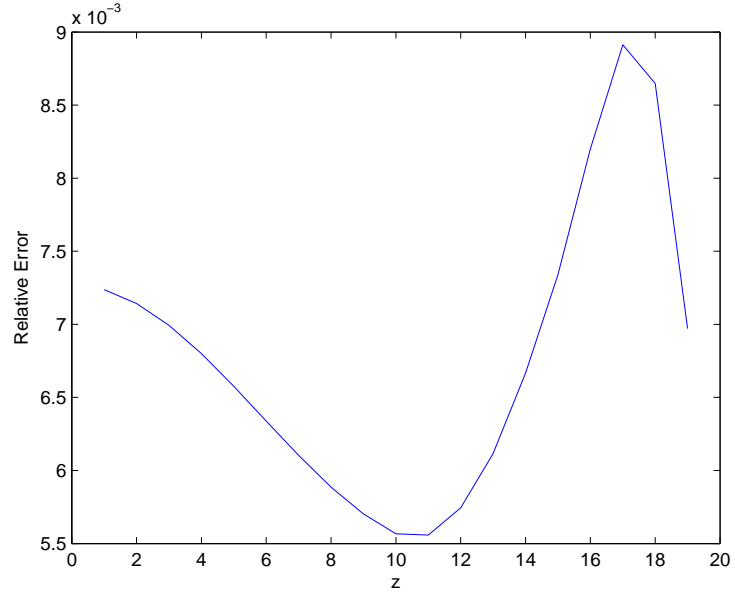
Figure 3.6: Relative Error of the Numerical Φ Solver.

3.2.6 Implementation

After the conductivities are calculated, the information about the size of the system are used for constructing the coefficient matrix. Depending on the geometric shape and the type of boundary condition (Dirichlet and Neumann), the coefficient matrix is constructed accordingly. The data is then stored in a known column vector. All information then passes to the electric potential solver. There, the program first manipulates the coefficient matrix using the LU incomplete factorization. In the meantime, the initial guess for the potential profile from the previous time step along with the conditioned coefficient matrix are input to the BIGSTAB method to compute the final solution for the electric potential. Figure 3.7 illustrates the logical flow of this process.
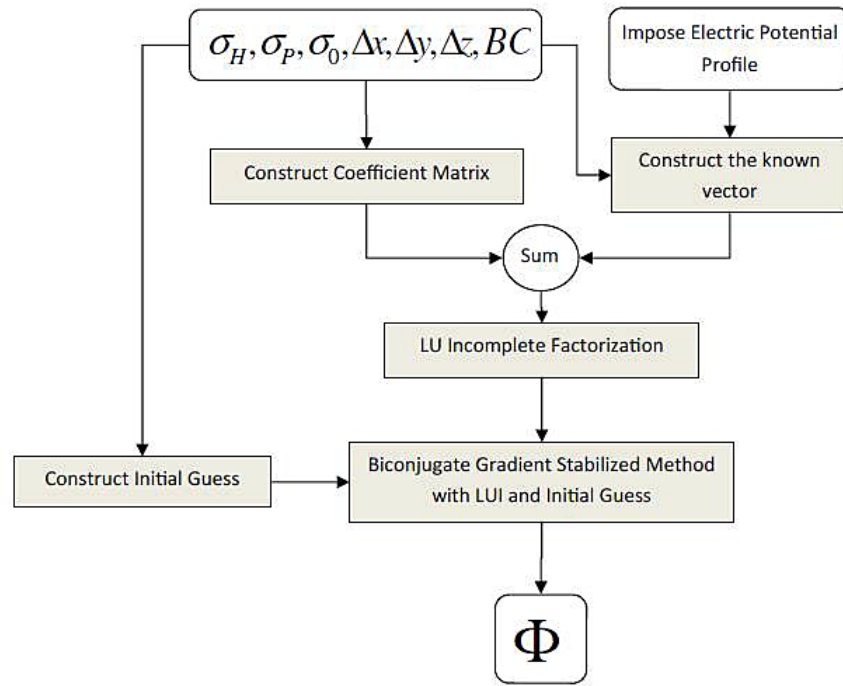
Figure 3.7: Synthesis of the Potential Solver.

3.3 Models and Simulation

By incorporating the previous numerical methodologies, the top level architecture for the entire model is illustrated in Figure 3.8. During the initial setup, all parameters are passed to the function through the MSIS model. It provides all the essential initial information about the neutral environment. The program then first calculates the potential in order to obtain the electric field and other arguments to compute perpendicular velocities via Momentum Balance Equation. This information then is given to the momentum equation to compute the parallel velocities. With the newly updated velocities, the density function and energy balance equation then compute the new density and temperature for the subsequent time steps. All results then are fed back to the *Input Parameters* to initiate the next time step.

Figure 3.8: Overall Program Architecture.

Chapter 4

Model Comparison and Data Verification

4.1   3-D and 2-D Models

Since this is the first model to demonstrate a small scale 3D ionospheric structure with multiple fluids, there is no reference data that can help perform any system level evaluation. However, our new model can theoretically be reduced to a 2-D model by eliminating any variations in the extra dimension. Currently, Zettergren and Semeter [2012] have already developed an ionospheric model in the 2-D limit. We will attempt to utilize results from their work to validate the 3-D model. Also, we developed a few simple 3-D scenarios in section 4.2 for which the behavior can easily be explained in order to test the functionality of the new model.

Set Up	2-D Model	3-D Model
Peak $\mid E_\perp \mid$	110 mV/m	110 mV/m
Is Φ Constant in Time?	Yes	Yes, and Φ is constant in y
Electron Flux	~ 0.1 mW/m^2	~ 0.025 mW/m^2
B.C.	DTNE	DTNE
Background Winds	No	No
Rnn Time	10 mins	10 mins

Table 4.1: Comparison of Different Iterative Methods (note, DTNE: Dirichlet for Topside and Neumann Elsewhere).

4.1.1 Setup

Table 4.1 shows the initial setup for the simulation. Figure 4.1 shows the imposed topside boundary electric potential condition conditions and Figure 4.2 illustrates the initial electron density profile. This profile is generated by running the simulation without any imposed topside boundary condition and allowing the density to reach an equilibrium state. In order to generate results similar to the 2-D model, the initial setup has to eliminate any variations in the E-W direction. Therefore, a planar geometry is imposed at the topside. Finally, this simulation is perform on an 100 x 100 x 130 finite difference grids (x,y,z) with a grid size of 10 km in both N-S and E-W directions. In the vertical direction, it consists of non-uniform grids ranged from 80 km to 800 km in altitude.
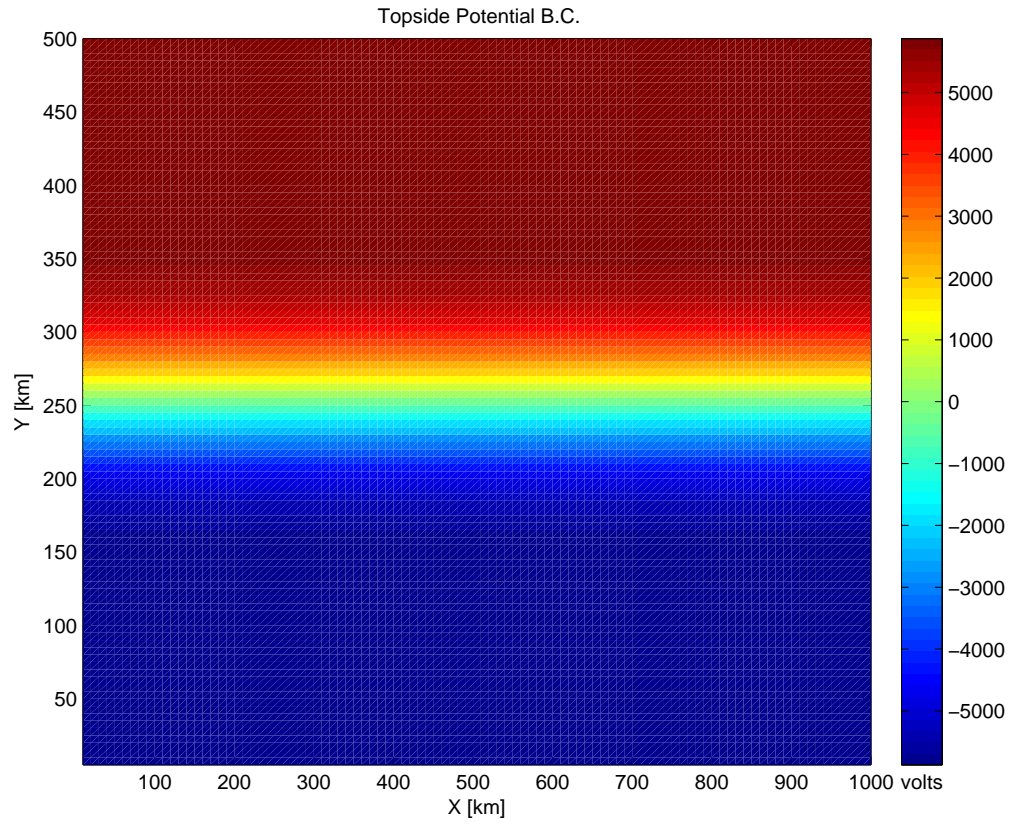
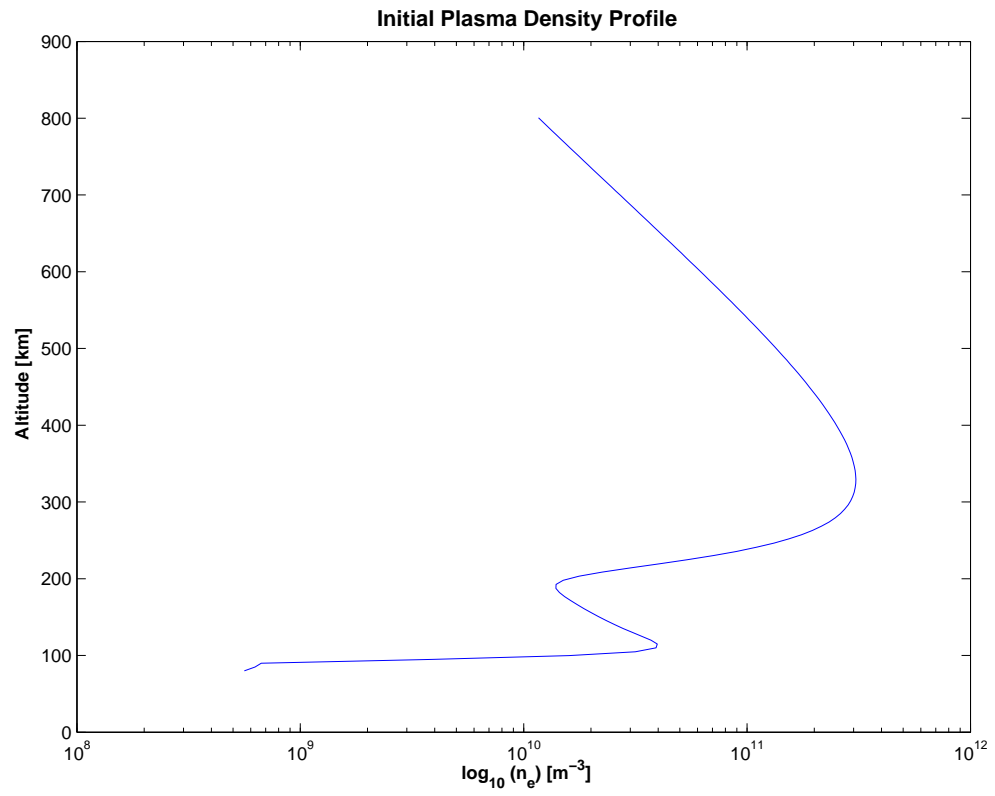Figure 4.1: Topside Potential Boundary Condition (note that x is the E-W direction and y is the N-S Direction).

Figure 4.2: Initial Density Profile.

4.1.2 Physical Processes

In order to validate this model, each process has to be carefully examined. Therefore, we will compare the 3-D and 2-D model panel-by-panel to understand the physical processes that are reproduced here. Figures 4.3 and 4.4 show the model results of 2-D and 3-D respectively.

Fig. 4.3a and Fig. 4.4a:

Compared to the initial current density profile, the downward current region is broadened (from initially 20 km to 40 km). This broadening is a result of the depletion process in the E-region (around 100 km) density. As density reduces, it decreases the Pedersen conductivity causing the downward current region to be broadened in order to utilize more charges to maintain the current flow in this configuration. Both of these panels demonstrate the same process.

Fig. 4.3b and Fig. 4.4b:

These panels show the Pedersen Current flowing in the negative direction to connect the downward and upward current region. Above that altitude of around 100 km, a decrease in Pedersen conductivity results in a very little cross-field current in those regions (130 km $< z <$ 350 km).

Fig. 4.3c and Fig. 4.4c:

In the E-region around 100 km, we have a depletion of the E-region due to a strong Pedersen current which transports ions in the negative x direction. Stagnation of ions in that region creates 77 percent enhancement of density at the bottom of the upward

current region. In the F-region between 250km to 500km, we see another depletion region, which is a combination of the chemical and recombination processes of O^+ and NO^+ (details are discussed in Section 2.1.2). This causes density to decrease depleting the F-region. Furthermore, the features of ion upflow which extends to 800 km, and downflow below the F-region peak (around 350 km) are also illustrated.

Fig. 4.3d and Fig. 4.4d:

These panels show the transitional altitude where the plasma is 50 percent molecular ions and 50 percent O^+. Enhancements are a result of the chemical process discussed above.

Fig. 4.3e and Fig. 4.4e:

Shows the ion heating occurring in the E and F regions. This heating is primarily due to the ion-neutral collisions. When the ions are moving across the field line, it collides with the neutral species creating frictional heating. This process is simulated by implementing the energy equation. The 2-D model solves the full time dependent energy equation [Zettergren and Semeter, 2012], while the 3-D model solves the energy balance equation. The differences between the transient and equilibrium states constitute the variations between Figure 4.3e and Figure 4.4e. As we have discussed in section 3.1.2, the 3-D model does demonstrate a very similar temperature profile as the 2-D model from 80 km to 600 km.

Fig. 4.3f and Fig. 4.4f:

The frictional heating generates an intense topside pressure enhancement, which leads to ion upflow in the high altitude region (Discussed in section 2.3.2). Due to the

temperature variations and dynamics on the topside of this system, we therefore see the variations in the velocity profiles between the 2-D and 3-D models.

4.1.3 Data Comparisons of the Transitional Altitudes

The transitional altitude corresponds to the ion composition of the ionosphere. This altitude is determined when 50 percent of the plasma is O^+ and 50 percent are the other ion species. Since the composition variations are due to the ionospheric heating and the chemical reactions, by modeling it against the electric field, it can illustrate the important point of how electric field contributes to the variations in transitional altitude. Zettergren and Semeter [2012] have an extensive discussion on the physical implications of this. Our purpose here is to perform model verification. In Figure 4.5, the data is obtained by measuring the perpendicular electric field and the transitional altitudes for a long exposure time. For the 2001 data, the exposure time is from 0215 to 0415 UT. For the 2003 data, the exposure time is from 1050 to 1800 UT. We then perform a data comparison with the 3-D model by taking a snap-shot at 100 and 809 seconds. The trends illustrated in these two time frames resemble the observation, providing a good validation for the model. In conclusion, the model shows rough agreement with the measurements.

4.1.4 Discussions

These two sets of figures generated by two different models are very similar except for the E-region densities and current magnitude. Table 4.2 quantitatively shows the approximate current densities. The 2-D model has linear current (it is defined as the
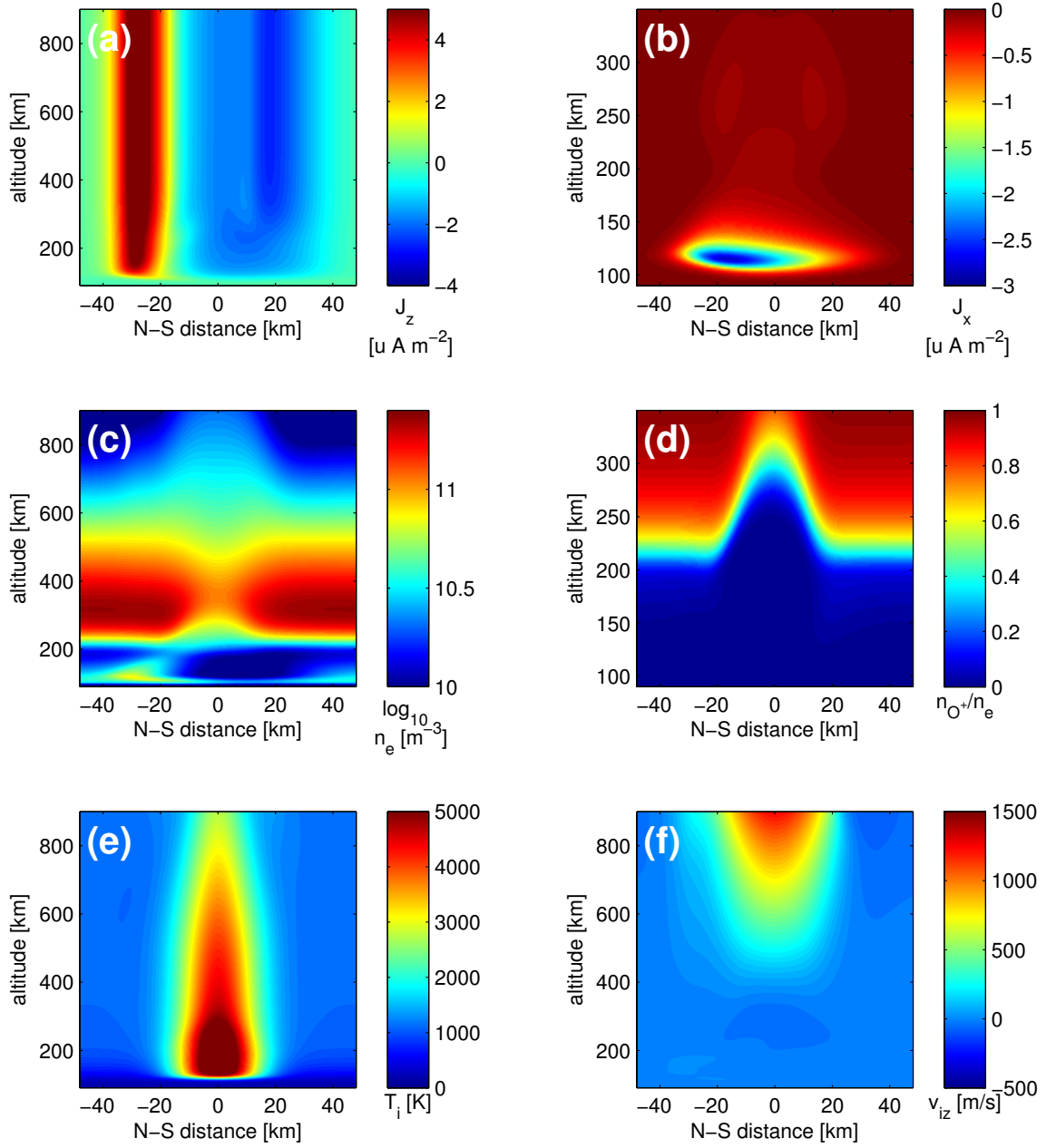
67

Figure 4.3: 2-D Model of the Auroral Ionosphere after t=300 seconds [Zettergren and Semeter, 2012], showing (a) Parallel Current Density, (b) Pederson Current Denisty, (c) Density Profile, (d) Transitional Altitude, (e) Temperature Profile and (f) Parallel Ion Drift Velocity.

Figure 4.4: A Slice of the 3-D Auroral Ionospheric model after t=300 seconds, showing (a) Parallel Current Density, (b) Pederson Current Denisty, (c) Density Profile, (d) Transitional Altitude, (e) Temperature Profile and (f) Parallel Ion Drift Velocity.
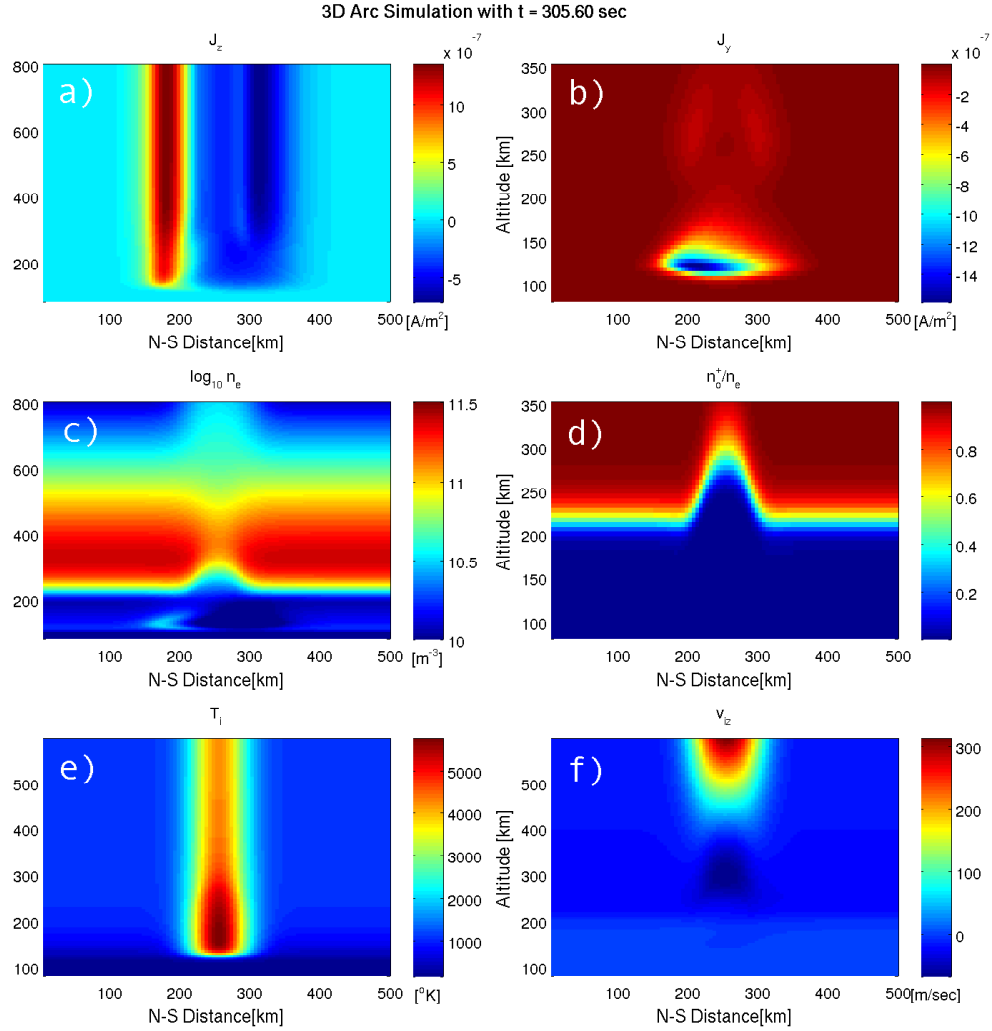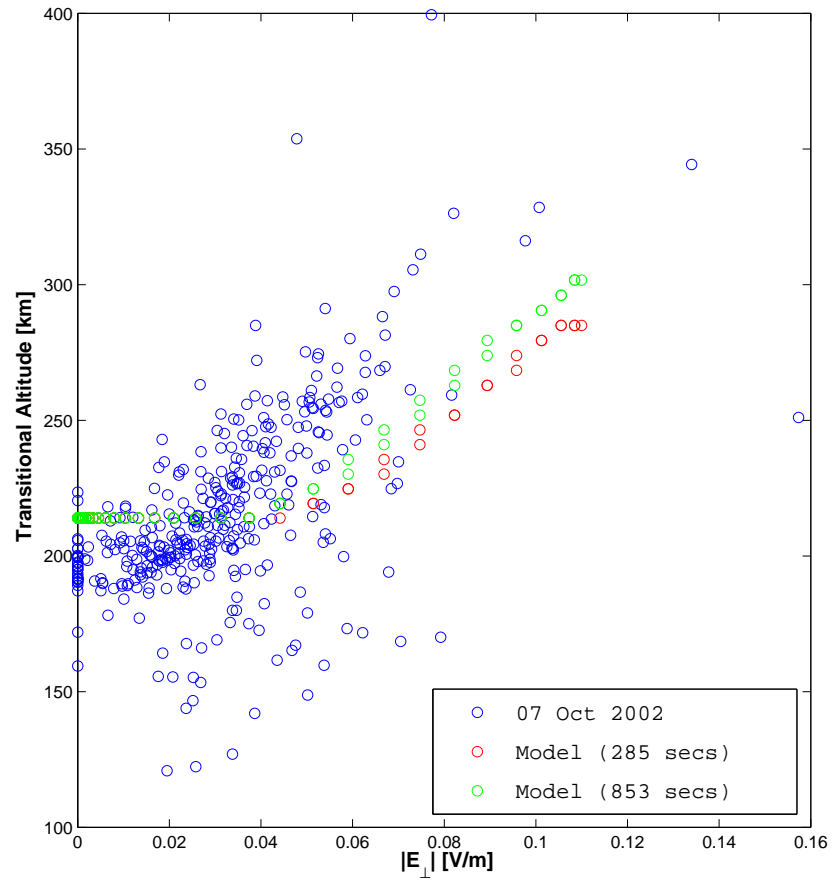
Figure 4.5: Transitional altitude of ions vs. $|E_\perp|$, a comparison between radar data and 3-D model in different time frames.

current density J_z multiplied by N-S Distance, that gives the linear current density A/m along the E-W direction) density around 0.08 A/m, compared to the 3-D model with around 0.05 A/m. The current density is directly proportional to conductivities (see equation 3.66), and the conductivity is directly proportional to the density. We can investigate if this ratio is related to the differences in E-region density. More specifically, we have linear UC around 0.075 A/m in the 2-D model and 0.06 A/m in the 3-D model. That gives a ratio of 1.25. Similarly, the ion densities in that region are $3.16 \times 10^{10} \mathrm{m}^{-3}$ and $2.51 \times 10^{10} \mathrm{m}^{-3}$ respectively. That gives a ratio of around 1.27. This analysis draw three preliminary conclusions. Firstly, the divergence of current density remains very close to zero (see table 4.2) in both models. Secondly, for a fixed topside potential, the current densities are indirectly related to the E-region ion densities. Thirdly, the geometries of the current systems in both models are essentially identical. More importantly, features such as the broadening of the downward current region and the evacuation of E-region (see Fig. 4.4c), the chemical processes in the F-region and ion upflow above 500km are all resolved. Furthermore, the transitional altitude between the two graphs are identical (around 300km). The major differences between them are the temperature profiles and the average parallel drift velocities (4.4e vs. 4.3e and 4.4f vs. 4.3f). This is primarily due to the different approaches in solving the energy equations Zettergren and Semeter [2012] model solves fully time dependent energy equation, while 3-D solves the energy balance. Despite the differences, these two models agree very well.

Current System	2-D Model	3-D Model
Upward Current	4 μAm^{-2}	1.3 μAm^{-2}
N-S Distance	2 $\times$ 10^5 m	4 $\times$ 10^4 m
Linear UC	0.08 Am^{-1}	0.052 Am^{-1}
Downward Current	2 μAm^{-2}	0.3 μAm^{-2}
N-S Distance	4 $\times$ 10^5 m	2 $\times$ 10^4 m
Linear UC	0.08 Am^{-1}	0.06 Am^{-1}
Cross-field Current	2.5 μAm^{-2}	1.2 μAm^{-2}
Altitude	3 $\times$ 10^4 m	5 $\times$ 10^4 m
Linear UC	0.075 Am^{-1}	0.06 Am^{-1}

Table 4.2: Current System Comparison.

4.2   Idealized Auroral Structures

By imposing different top boundary conditions, we can simulate a more realistic scenario to study the ionospheric responses under various types of atmospheric and electromagnetic forcing. The results from idealized auroral structures can be easily analyzed by drawing direct comparisons between this model and some well known physical processes. It serves as additional testing to evaluate the plausibility of the model's results. In the following scenarios, some simplified topside geometries will be imposed to elucidate the basic variations from the 2-D ionospheric model. Due to the complexity of 3-D visualization with time dependency, slice plots are introduced to dissect the system into a 2-D domains along the z direction to demonstrate the important features in plasma density, temperature and parallel drift velocity. In

addition, flow field diagrams are added to enhance visualization in order to allow more detailed analysis to be performed on the current density, velocity and plasma density evolution.

4.2.1   Bent Current Sheet

In this scenario, an error function equation 4.1 and Figure 4.6 constitute the geometry of the topside electric potential.

$$\Phi = \mathrm{erf} \left[\frac{y - e^{-\frac{(x-c_x)^2}{\gamma_1}}}{\gamma_2} \right] \Phi_0. \tag{4.1}$$

Table 4.3 describes the basic setup of this run. In order to demonstrate the evolution of different plasma's characteristics, the Matlab slices function is deployed to represent a 3-D function with a number of 2-D slices at the important regions along the z-axis. In addition, each slice has its own subplot at that particular altitude to further highlight the important features.

Temperature

The temperature profile is obtained by solving the energy balance equation (discussed in Section 3.1.2). As we know, in the E- and F- regions, we have frictional heating occurring, creating ion and electron upflow and it continues to propagate upward. Similar to the 2-D model, due to the imposed topside electric potential profile, the bent current sheet forces the charged particles to move along the curvature resulting in higher perpendicular velocity. Such an increase in speed creates localized heating around the bent regions(see Figure 4.7).
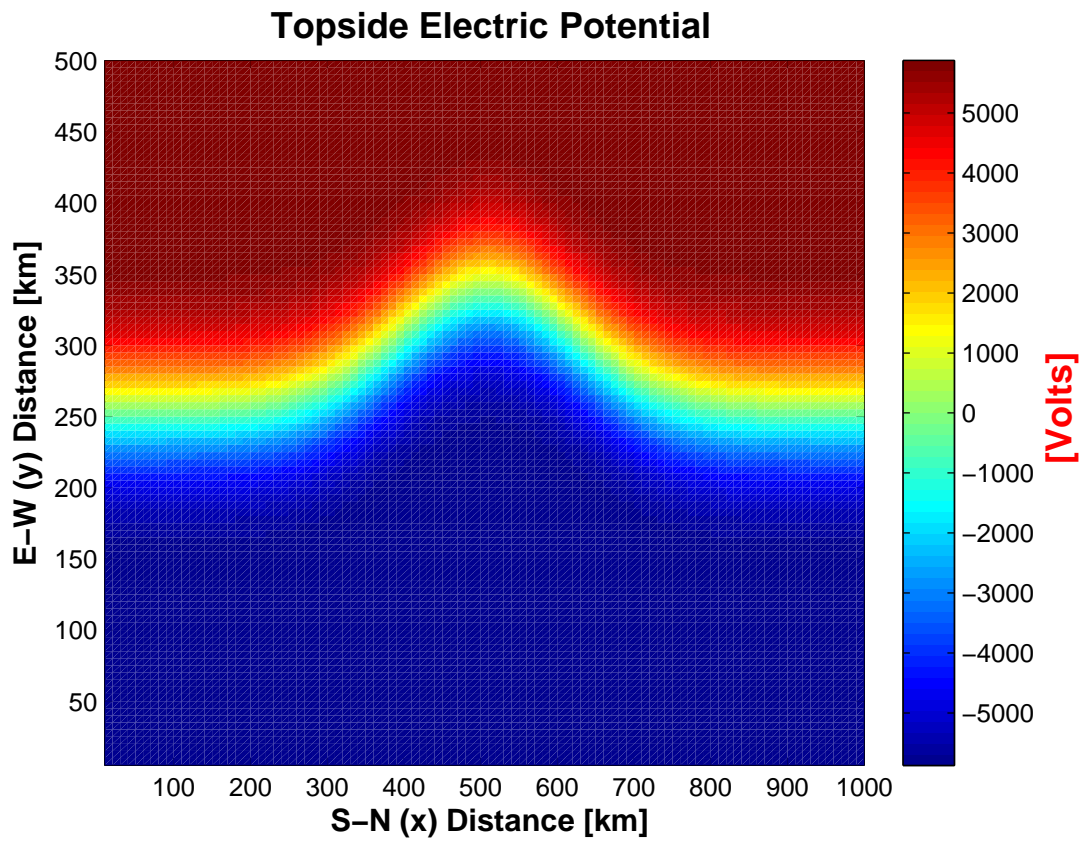
Figure 4.6: Topside Imposed Electric Potential Profile for Bent Current Sheet.

Set Up	Values
B.C.	DTNE
Initial Condition	Equilibrium Profile: 3×10^{11} m^{-3} (F-Region); 3.9×10^{10} m^{-3} (E-Region)
Neutral Winds	No
Electron Flux	0.025 mWm^{-2}
Peak $\mid E_\perp \mid$	0.12 Vm^{-1}
Slices	$z_1 = 100$ km,$z_2 = 250$ km,$z_3 = 600$ km,$z_4 = 800$ km

Table 4.3: Basic Setup for Bent Current Sheet.

Density Evolution

After 156 seconds from the initial time step (see Figure 4.8), you can clearly see the evolution of Pedersen current evacuating the E-region by creating low density region ($10^{10.55}$ m^{-3}) at the base of DCR, and high density region ($10^{10.64}$ m^{-3}) at the base of UCR. In this process, the plasma is being perpendicularly transported to a larger region indicated in red. In the F-region, the production and chemical recombination of NO$^+$ result in the reduction of plasma density around the most intense heated region at 250 km compared to higher altitudes around 600 or 800 km. At the 600 km altitude, we see the non uniformity in density due to the perpendicular transport of plasma. The $\mathbf{E} \times \mathbf{B}$ drift which follows the curvature causing the particles to move from x = 1000 km toward x = 0 km. Consequently, it creates the high density region on one side and low density region on the other (see Figure 4.8 at 600 km 2-D plot panel and same for 4.9). Simultaneously, ion upflow also advects plasma upward in
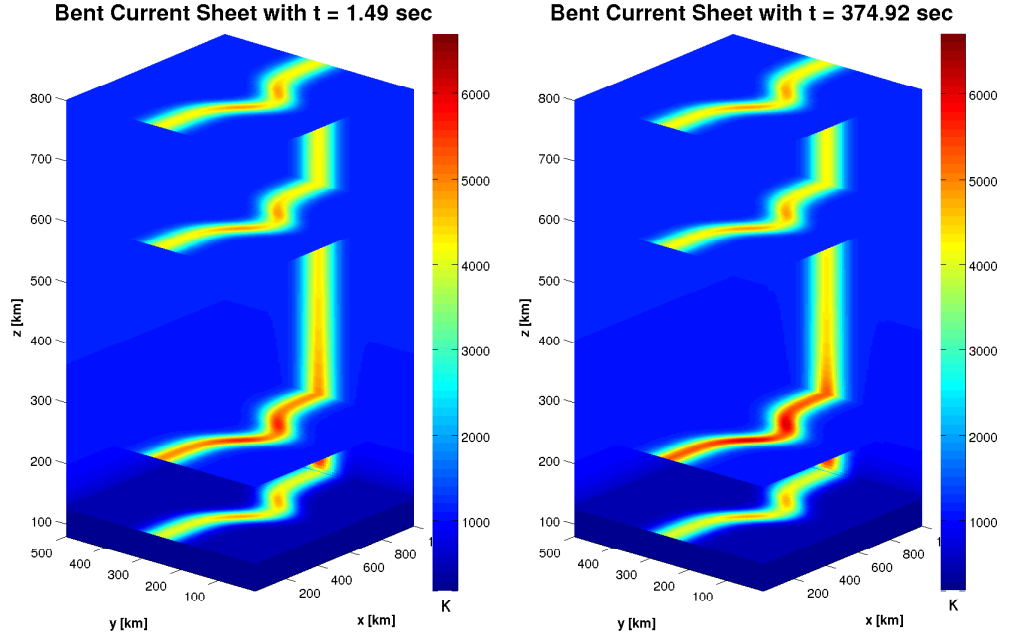
Bent Current Sheet with t = 1.49 sec   **Bent Current Sheet with t = 374.92 sec**

Figure 4.7: Ion Temperature Profile of Bent Current Sheet. Slices occur at z = 125 km (E-Region), z = 251 km (F-Region), z = 600 km and z = 800 km altitudes.

the region. From a simple comparison between Figures 4.9 and 4.8 at 800 km altitude the 2-D plot panel shows an average of around 2 to 3 percent reduction. Finally, at the 800 km altitude, again, we have ion upflow of around 1 km/sec that couples with the $\mathbf{E} \times \mathbf{B}$ transport velocity, which advects features in the x-direction.
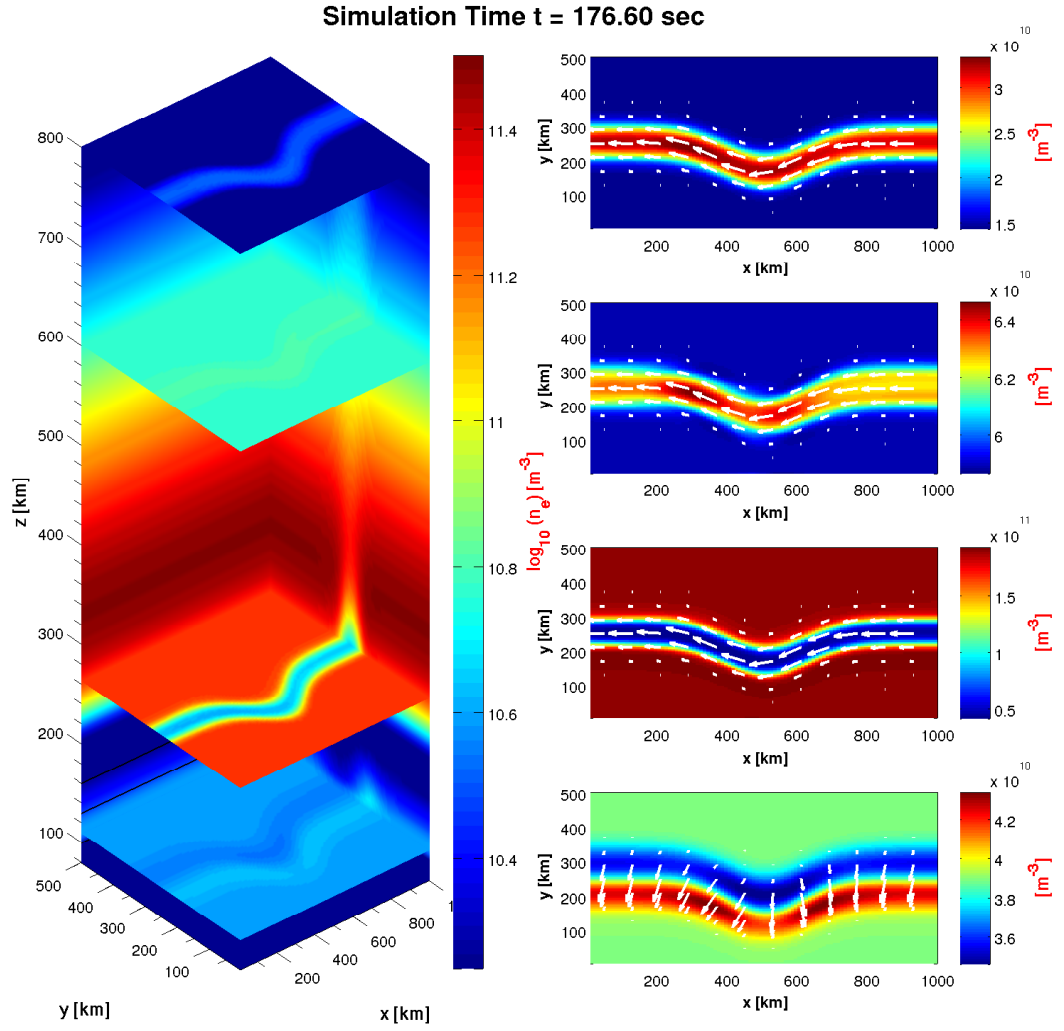
Figure 4.8: Density Slices at t = 176.60 seconds. Slices occur at z = 125 km (E-Region), z = 251 km (F-Region), z = 600 km and z = 800 km altitudes.
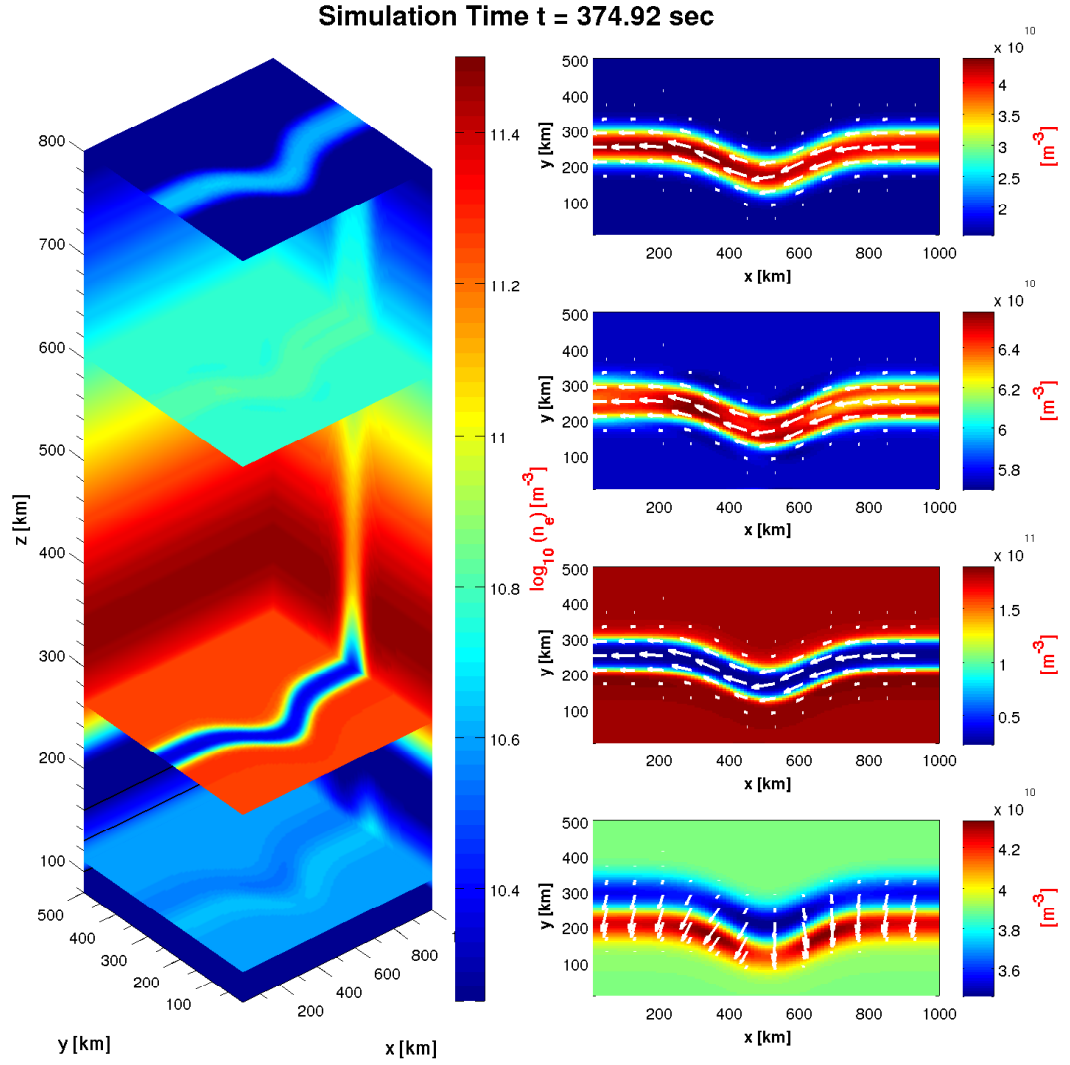
77

Figure 4.9: Density Slices at t = 375 second. Slices occur at z = 125 km (E-Region), z = 251 km (F-Region), z = 600 km and z = 800 km altitudes.

Parallel Velocity Evolution

After 1.49 seconds, in Figure 4.10, at the bottom of the F-region, the parallel velocity is driven by pressure gradient. Recall the plasma density peaks at the F-region creating downward pressure force below the peak and upward pressure force above the peak region. As the heating commences, this pressure gradient increases the upward and downward velocities above and below the peak region respectively.

In addition, momentum is being advected along the bent current sheet. We can see its evolution by comparing Figure 4.10, 4.11 and 4.12. It becomes pronounced in the later time because the upflow velocity begins to settle down to the quasi-steady state, while the perpendicular drift velocity $\mathbf{E} \times \mathbf{B}$ remains and dominates the transport process.
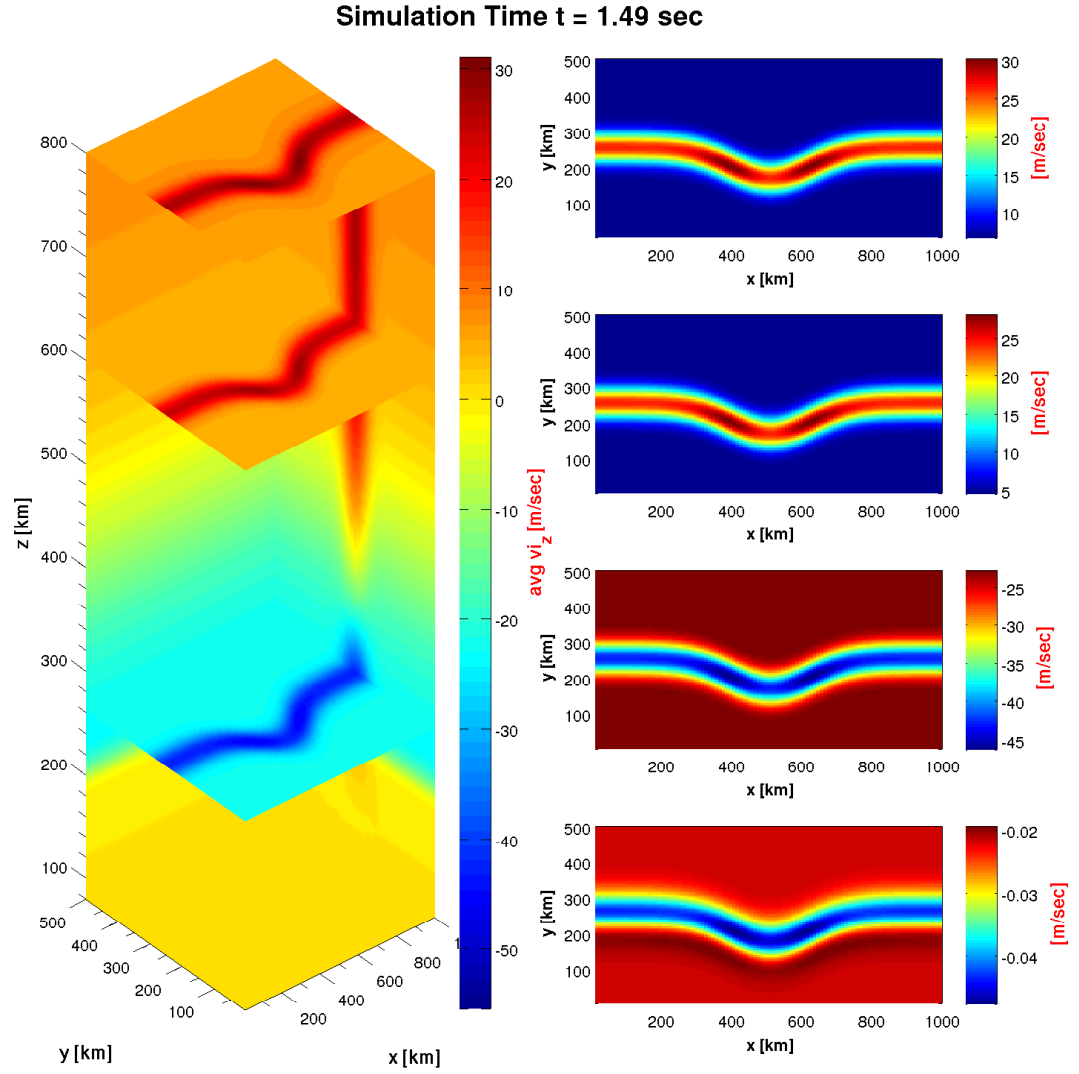
Figure 4.10: Parallel Velocity Structure at the initial time step, Slices occur at z = 125 km (E-Region), z = 251 km (F-Region), z = 600 km and z = 800 km altitudes.

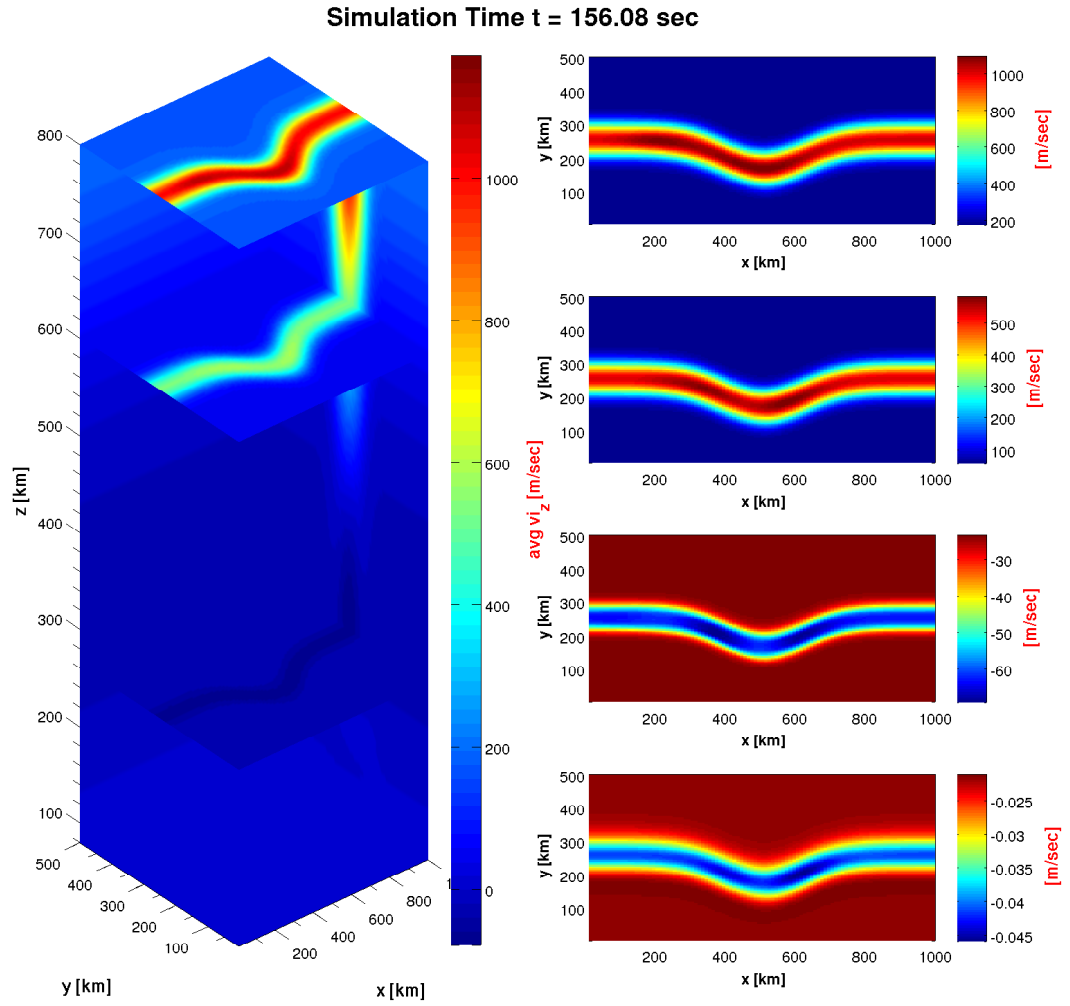Figure 4.11: Parallel Velocity Structure at t=156 seconds, Slices occur at z = 125 km (E-Region), z = 251 km (F-Region), z = 600 km and z = 800 km altitudes
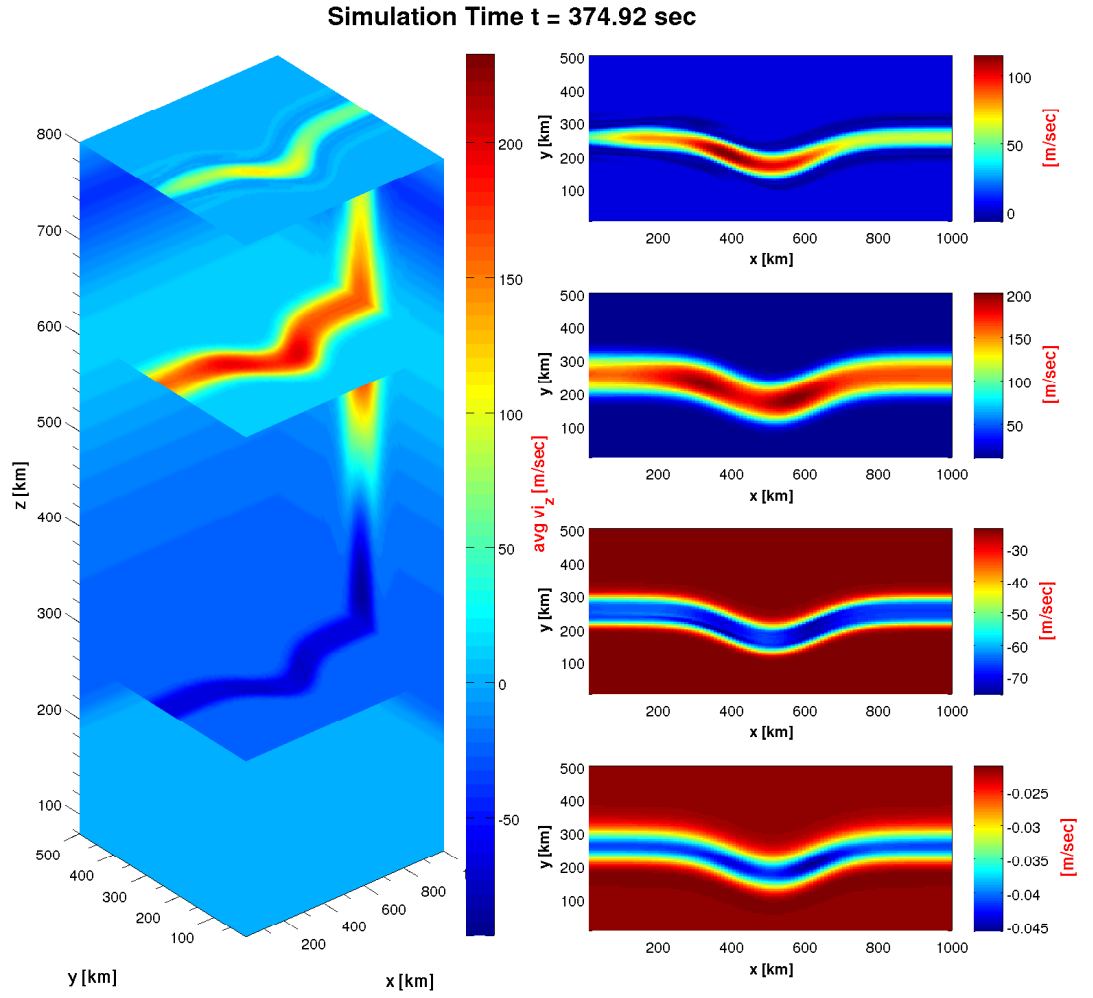
Figure 4.12: Parallel Velocity Structure at t=374 seconds, Slices occur at z = 125 km (E-Region), z = 251 km (F-Region), z = 600 km and z = 800 km altitudes

Reversed Bent Current Sheet

Another simulation with a similar bent current was run. The topside electric potential is as follows:

$$\Phi = \text{erf} \left[\frac{y + e^{-(x-c_x)^2/\gamma_1}}{\gamma_2} \right] \Phi_0. \tag{4.2}$$

Most other regions in the parallel direction remain relatively the same because the response $\mathbf{E}$ field remains unchanged, causing the $\mathbf{E} \times \mathbf{B}$ drift to be pointed along the bent current sheet. In the E-region however, we have a cross field current creating electric field that allows particles to move across different current regions. As a comparison, Figure 4.13 shows the plasma density in two different geometries after 375 seconds into the simulation. From the velocity flow fields, which are indicated in white arrows, the plasma from the upper bent region is transported toward the smaller region creating $\sim$ 4 percent density enhancement compared to the previous geometry. If we construct a smaller scale system, this process is likely to exhibit a more significant density enhancement. The geometrical placement of the upward and downward current regions create different responses, demonstrating the significance of introducing the third dimension.

Discussion

This kind of important of this kind of geometry occurs quite commonly in many auroral events. Since the auroral arcs are rarely planar, departures from 2-D geometry could have significant impacts on ionospheric response. However, the analysis has shown that the processes being presented here match our basic expectations about the ionosphere and further confirm the validity of our model.
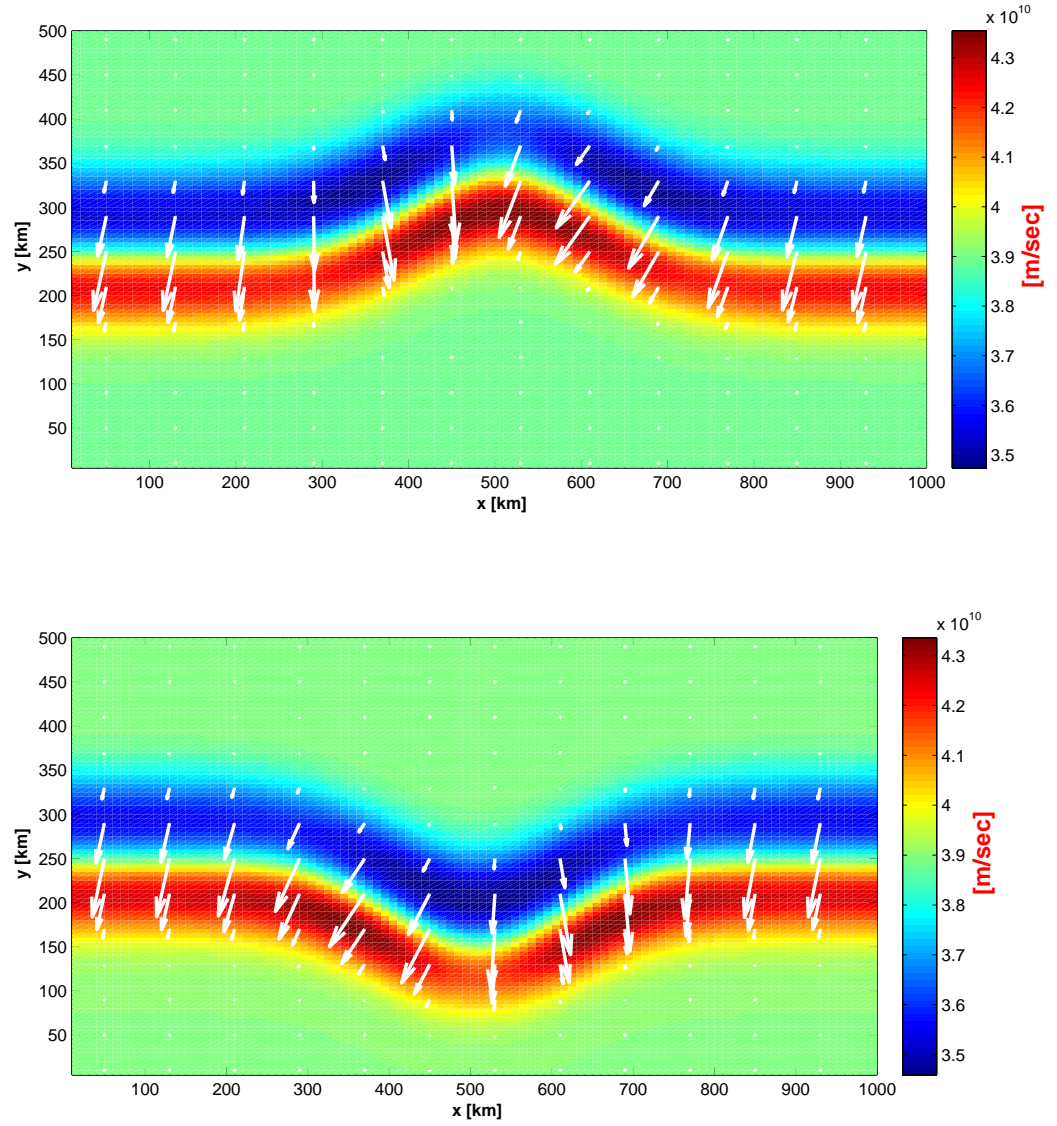
Figure 4.13: Different bent current sheet structures also play a role in Density Enhancement and Deplection.

Conditions	Values
B.C.	DTNE
Initial Condition	Equilibrium Profile: 3×10^{11} m^{-3} (F-Region), 3.9×10^{10} m^{-3} (E-Region)
Neutral Winds	No
Electron Flux	0.025 mW/m^2
Peak $\mid E_\perp \mid$	0.110 V/m
Slices	z_1=100 km,z_2=250 km,z_3=600 km,z_4=800 km

Table 4.4: Intial Setup of Cylindrical Geometry for Topside Boundary.

4.2.2 "Cylindrical" Current System

This is a scenario when an elliptical Gaussian topside boundary condition is imposed (see Figure 4.14). Unlike the error function, it creates a circular structure.

The topside Boundary Potential is as follows:

$$\Phi = \Phi_0 e^{(x-c_x)^2/\gamma_1 - (y-c_y)^2/\gamma_2}. \tag{4.3}$$

In this case, the elliptical profile has stronger potential differences along the y-direction ($\gamma_y < \gamma_x$) causing stronger perpendicular currents in that direction.

Unlike the previous scenario of having a two-current system, we have one main downward current region at the center of the ellipse and two upward current regions (see fig. 4.16). Similar to the previous scenario, the frictional heating from the $\mathbf{E} \times \mathbf{B}$ drifts is quite pronounced.
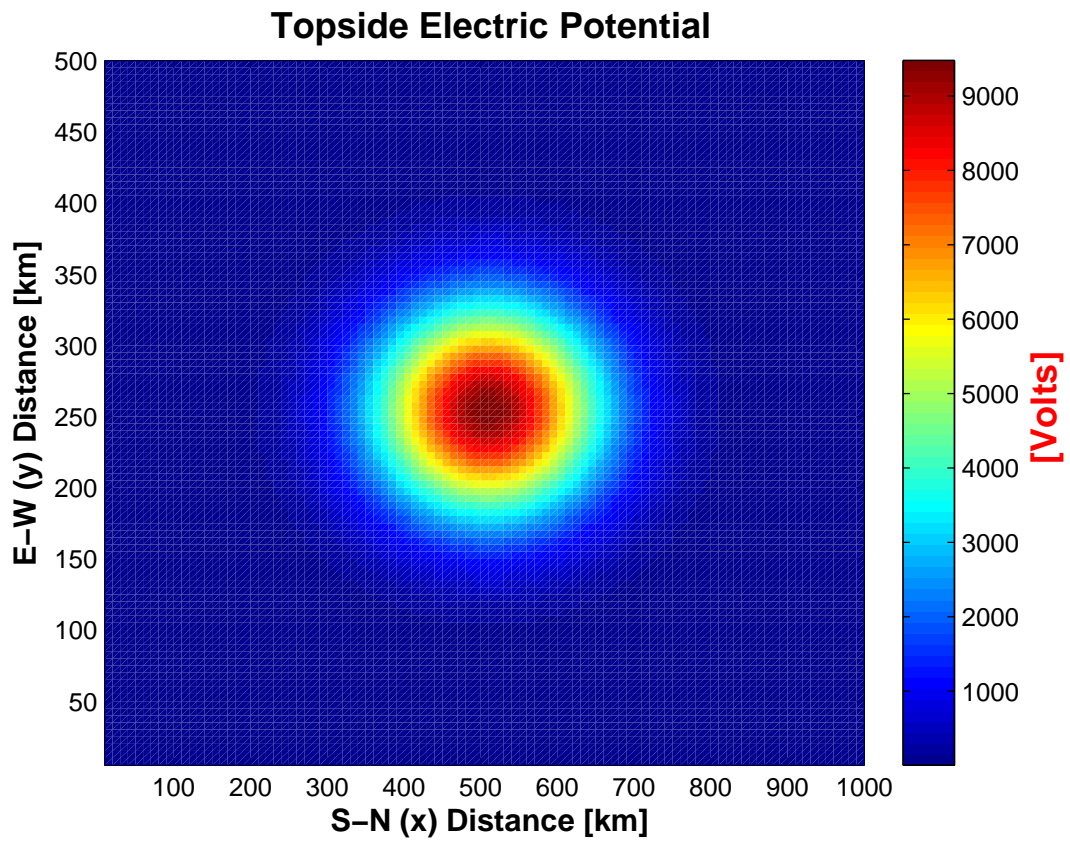
Figure 4.14: Topside potential boundary Condition for cylindrical current system.
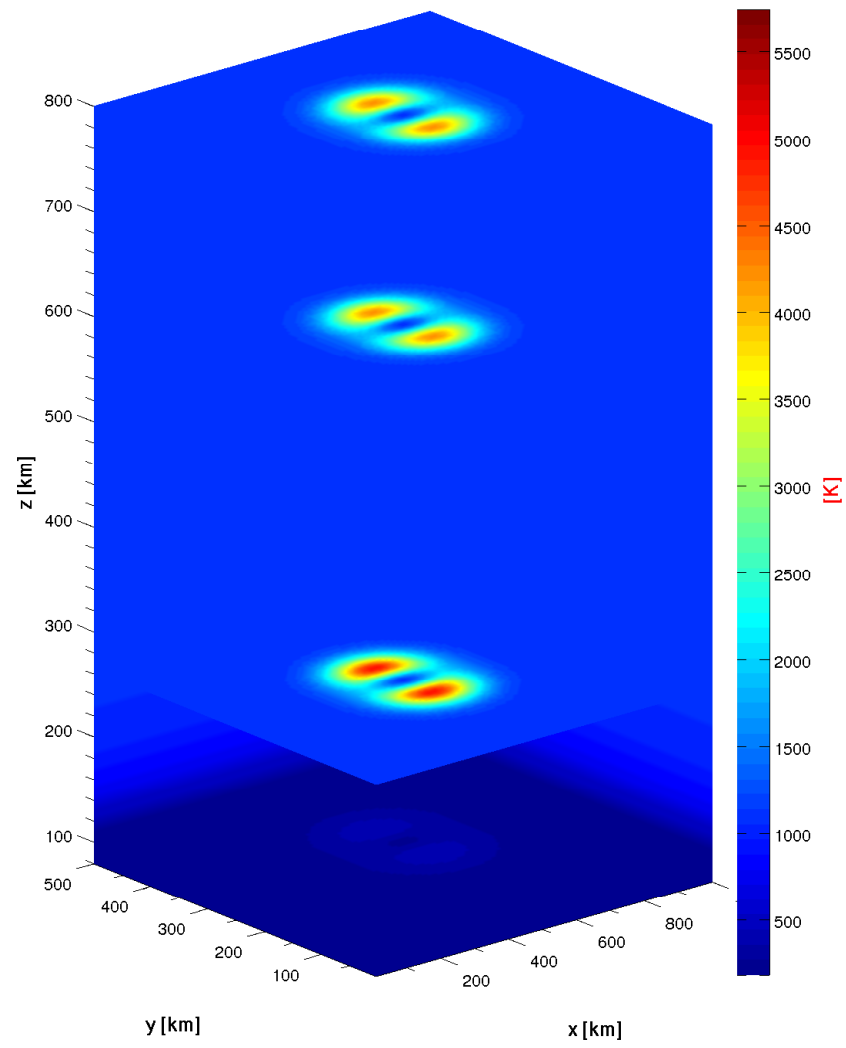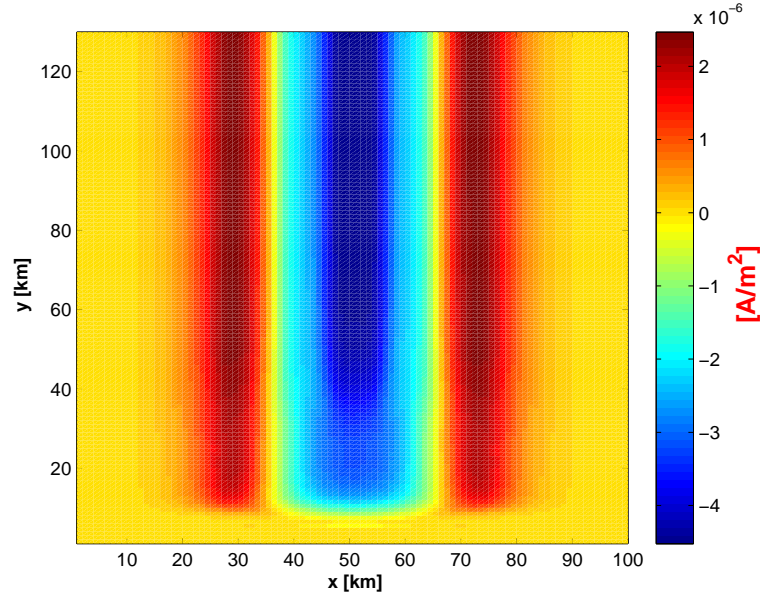
Figure 4.15: Equilibrum Temperature Profile.

Figure 4.16: Vertical current system of the cylindrical current System.

Temperature Evolution

Similar to the previous scenarios, the temperature profile in Figure 4.15 is based on the energy balance approximation. There are two high temperature regions. We denote the first one R_1 near the lower end of the y-axis and R_2 near the higher end of the y-axis. These two regions are caused by the stronger perpendicular currents which creates more intense frictional heating than the currents in the other direction. As the heating propagates upward, it maps along the field line toward the topside of this system.

Density Evolution

In the E-region, the cross-field current evacuates and transport plasma from one region to the two upward current regions causing the E-region structure we see in fig. 4.17.

In the F-region, chemical alterations and recombination occur. However, since the heating is not uniform in both x and y directions, we have a higher chemical recombination rate along the y-direction than x-direction. This results in density variations as you see in the 250 km slice of Figure 4.17. Unlike the previous scenario, instead of transporting plasma along a bent current sheet, we have elliptical circulating motion in Figure 4.17 at the 250 km slice. As time progresses, it continuously rotates the depleted plamsa to smear out the nonuniform density structure forming a uniform plasma ring as you see in Figure 4.18 at the 250 km slice.

At the 600 and 800km altitudes, we have two comparable motions occurring simultaneously: the upflow of ions and the rotational motion. As we have previously discussed in Section 4.1, the upflow creates density enhancement of around 60 percent at the 800km altitude and around 9 percent at the 600km altitude. However, it is not an uniform motion. The higher parallel velocity enhances the density, and less enhancement appears in the lower parallel velocity region. As time progresses, the difference in density enhancement becomes more and more pronounced . Again, the perpendicular rotational motion creates a more uniform density ring geometry in the later stages of evolution (Figure 4.18).

Parallel Velocity Evolution

In the E-region, due to the high collisions with the neutral species in that region, there is very little parallel drift velocity. Right below the F-region, we have pressure gradient driven downward parallel motion. However, due to the variations in temperature, they intensify the downward velocity in the hotter region. In contrast, the cooler regions have less effect on the downward velocity (see Figure 4.15. In addition, the rotational
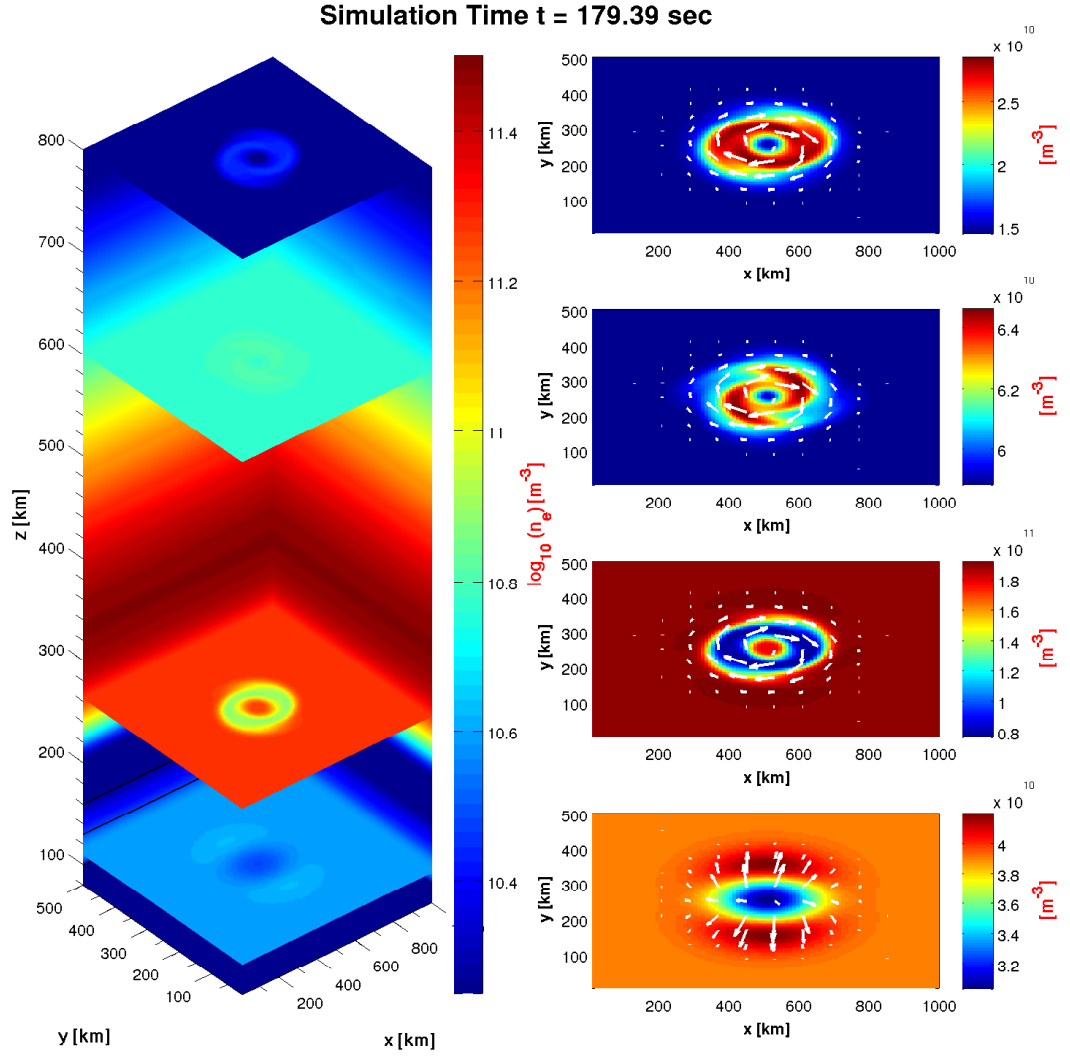
Figure 4.17: Density Slices at t = 179.60 seconds. Slices occur at z = 125 km (E-Region), z = 251 km (F-Region), z = 600 km and z = 800 km altitudes.
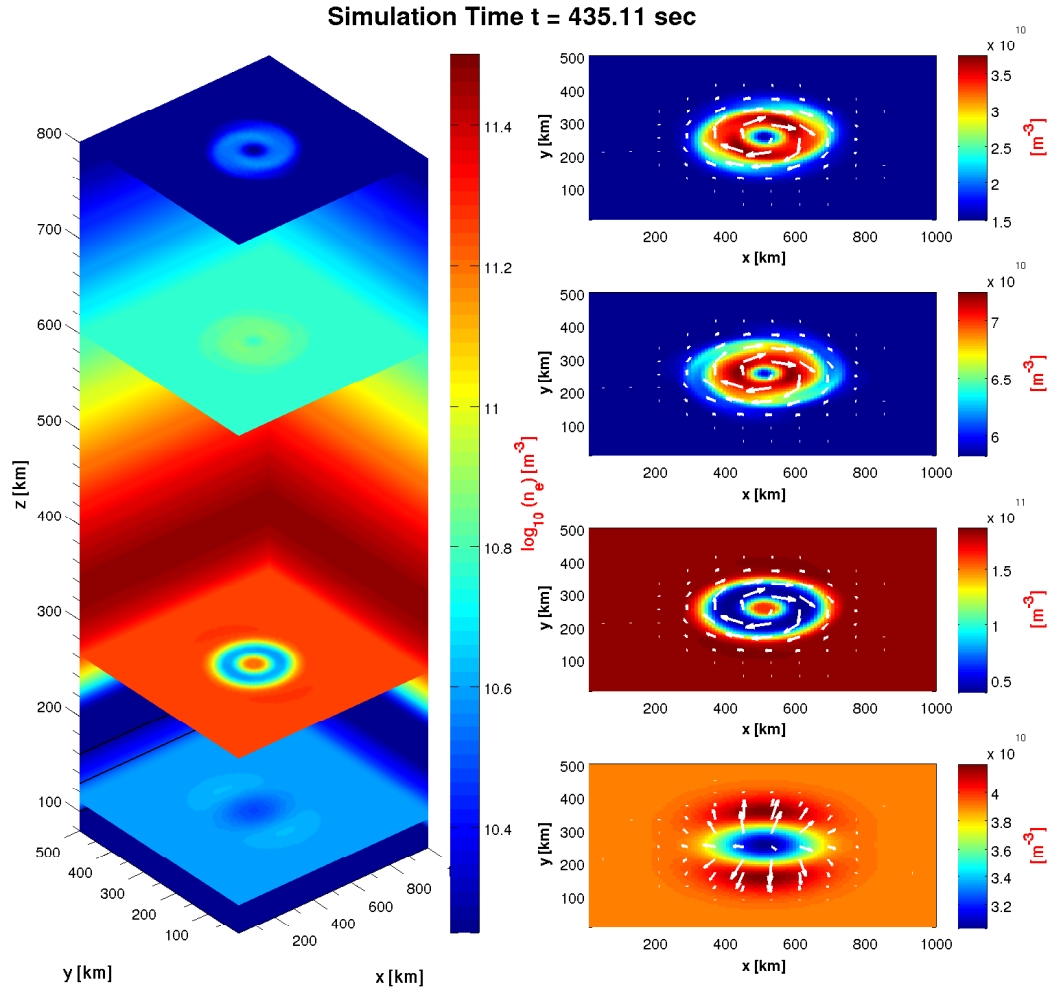
Figure 4.18: Density Slices at t = 435.11 seconds. Slices occur at z = 125 km (E-Region), z = 251 km (F-Region), z = 600 km and z = 800 km altitudes.

motion also advects the velocity in the elliptical manner similar to the density profile. As time progresses to 200 seconds, Figure 4.20 shows slightly higher velocity (60 to 70 percent) than t=96 seconds in Figure 4.19 between the two higher downward velocities regions that generates higher temperatures (R_1 and R_2).

At the 600 and 800km altitudes (see Fig. 4.21), we have two competing velocities $v_\perp$ and $v_\parallel$. (Note, the perpendicular velocity remains unchanged with respect to altitude due to the $\mathbf{E} \times \mathbf{B}$ drift). Combination of these two velocities creates helical motions of plasma parcels. For example in Figure 4.21, at the 700 km altitude, the magnitude of the parallel velocity is only 40 percent lower than the magnitude of the perpendicular component in the hot regions R_1 and R_2.

Discussion

Overall, the data generated from this model creates explainable phenomenon that match our physical understanding and expectations. It further strengthens our confidence in the model. In the next chapter, we will deploy this model to look at some realistic data and make some comparisons with the observations.
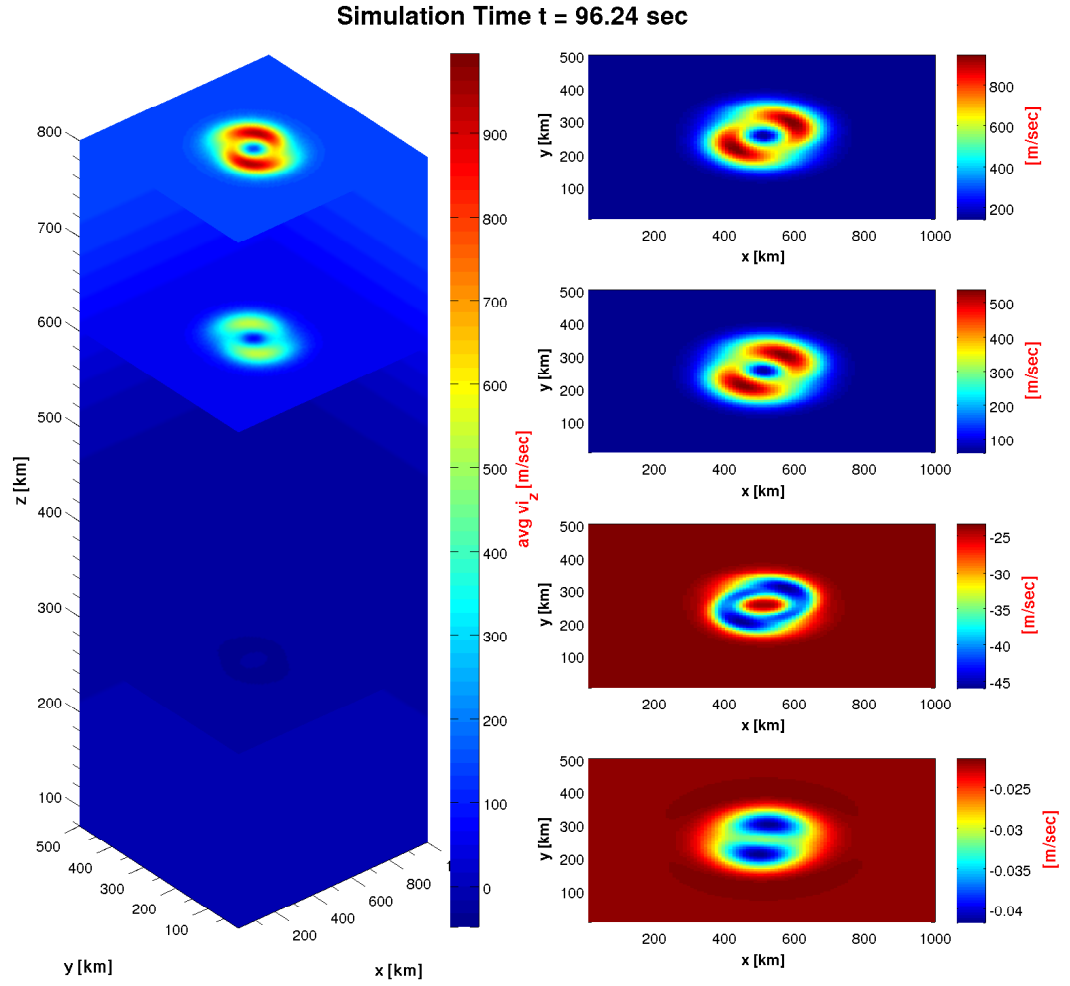
Figure 4.19: Parallel Velocity Structure at t=96 seconds, Slices occur at z = 125 km (E-Region), z = 251 km (F-Region), z = 600 km and z = 800 km altitudes.
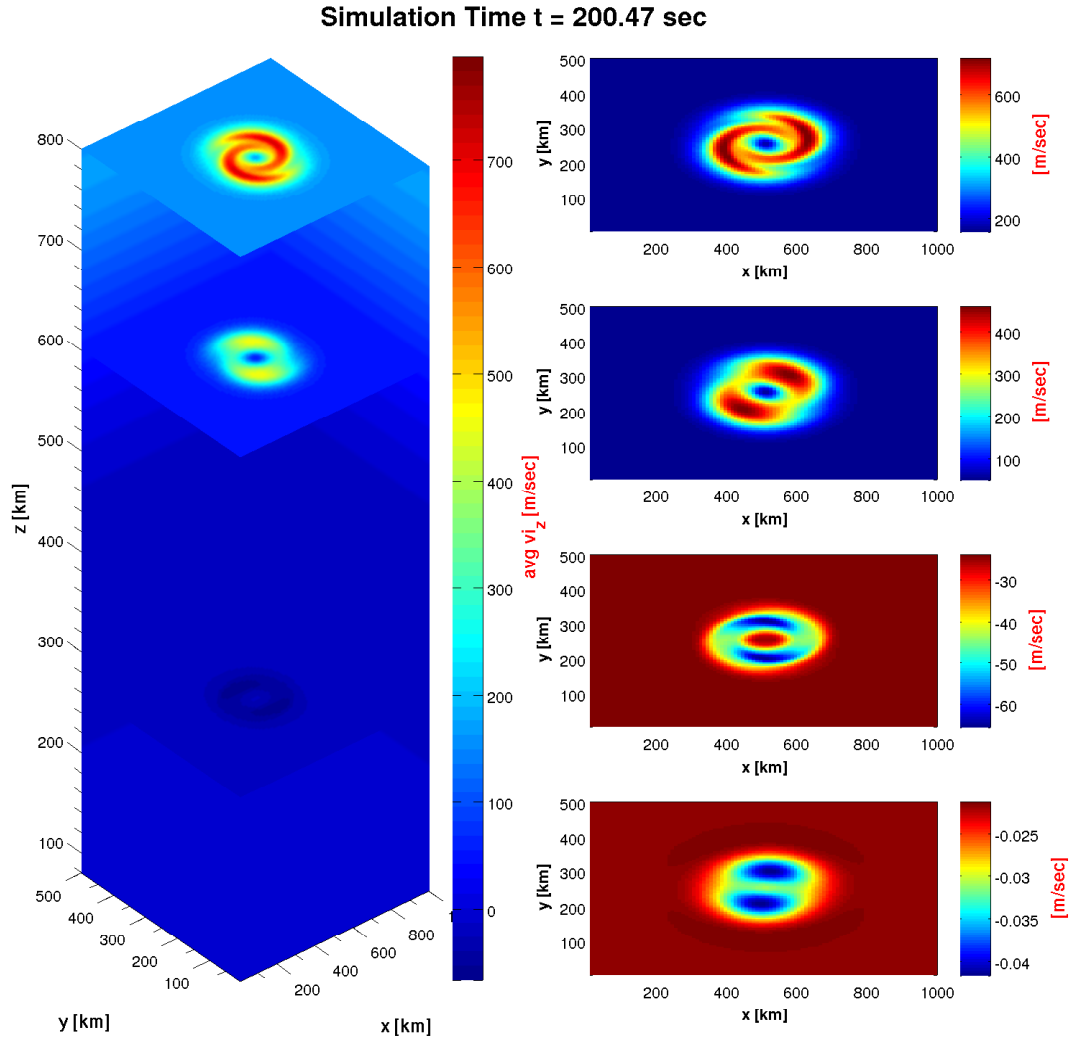
Figure 4.20: Parallel Velocity Structure at t=200 seconds, Slices occur at z = 125 km (E-Region), z = 251 km (F-Region), z = 600 km and z = 800 km altitudes.
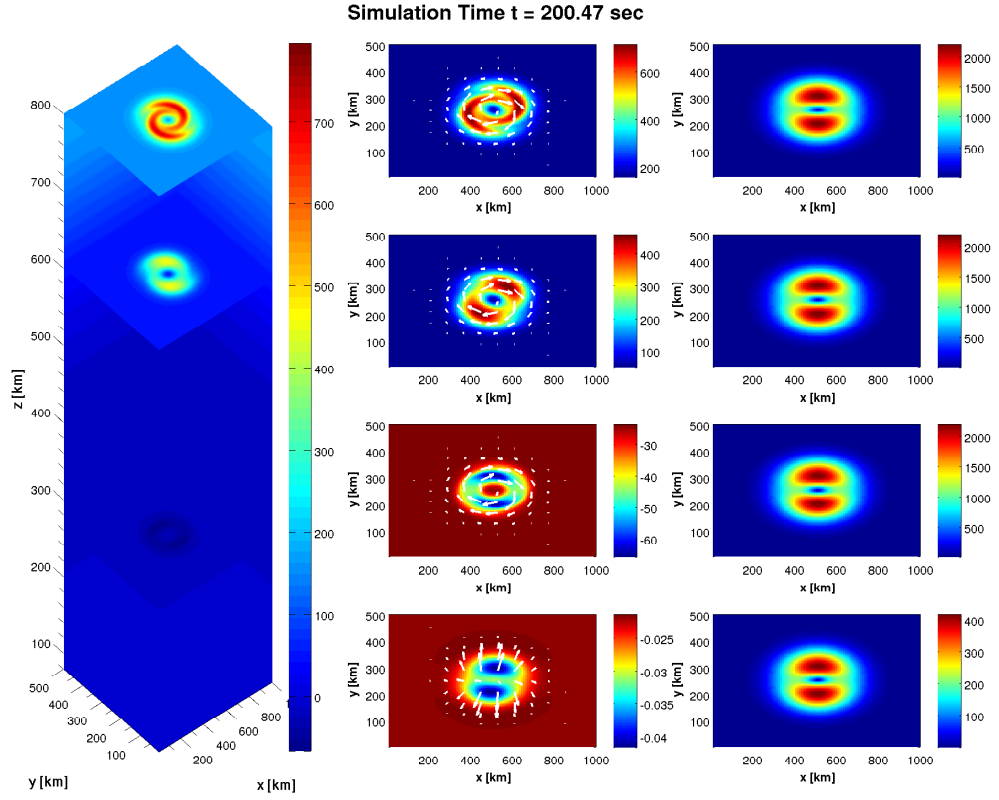
94

Figure 4.21: 1st column slice graph shows the 3-D structure of the vertical velocity. 2nd column shows the parallel drift velocity at different sliced altitudes. 3rd column shows the magnitude of the perpendicular velocities. The unit for coloarbars are in m/sec. Slices occur at z = 125 km (E-Region), z = 251 km (F-Region), z = 600 km and z = 800 km altitudes.

.

Chapter 5

Case Studies

5.1 Realistic Boundary Conditions

On February 26, 2001, an experiment was conducted to analyze the responses of ionosphere to magnetospheric forcing. Figure 5.1 shows the convection patterns estimated by the SuperDARN radar data during an auroral event. It was simultaneously observed by the Sonderstrom ISR (Incoherent Scatter Radar). The image shows a flow reversal potential structure. Our area of interest is where the arrows point near where the Sondrestrom radar is located. In this section, we attempt to model the structure and the ionospheric response.

Figure 5.3 shows the imposed topside boundary condition. On one side, we will have a strong potential gradient to simulate fast moving flow, and a weak potential gradient on the other to simulate a slow moving flow.

Set up

There are two criteria we use to ensure our setup matches with the radar data: the

Conditions	Values
B.C.	DE (Dirichlet B.C. Everywhere)
Initial Condition	Equilibrium Profile: $3 \times 10^{11}/\text{m}^3$ (F);$5.4 \times 10^{10}/\text{m}^3$ (E)
Neutral Winds	No
Electron Flux	0.025 mW/m^2
Peak $\mid E_\perp \mid$	0.0929 V/m

Table 5.1: Basic Setup of Realistic B.C.

geometry of the equipotential lines and the magnitude of the perpendicular drift velocity (both quantities are provided from Figure 5.1). This figure shows that the north side of the auroral arc exhibits high drift velocity of around 1800 m/sec. The south side has average velocity of around 500 to 600 m/sec. Table 5.1 shows the basic setup for this run. From Figure 5.2, we can see that the simulated perpendicular velocity has a range between 600 m/sec to 1800 m/sec in the current sheet (x denotes N-S Direction, y denotes E-W Direction). In addition, the simulated geometrical structure appear to match the data shown in Figure 5.1. Therefore, this setup should satisfy the objective of this run.

Density Evolution

Due to the high gradient potential region between x =750 km to 900 km, it invokes an initial disturbance in the region as shown in Figure 5.4, three seconds into the simulation, the magnitudes of density perturbations are relatively small. As we progress later to around 130 seconds (Fig. 5.5), we see that three different processes are evolving. In the E region, the depletion occurs in the upper x-axis region due to
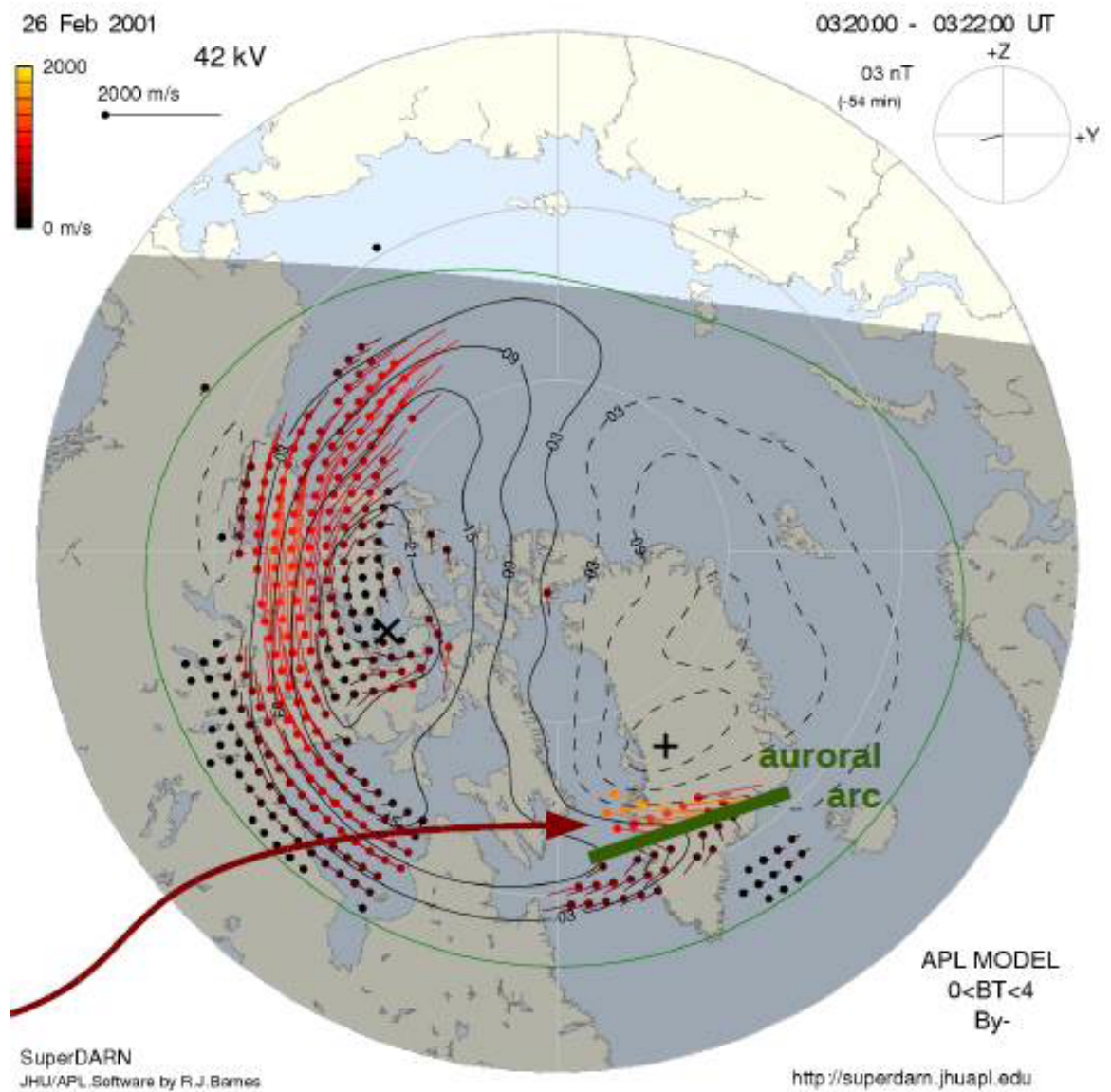
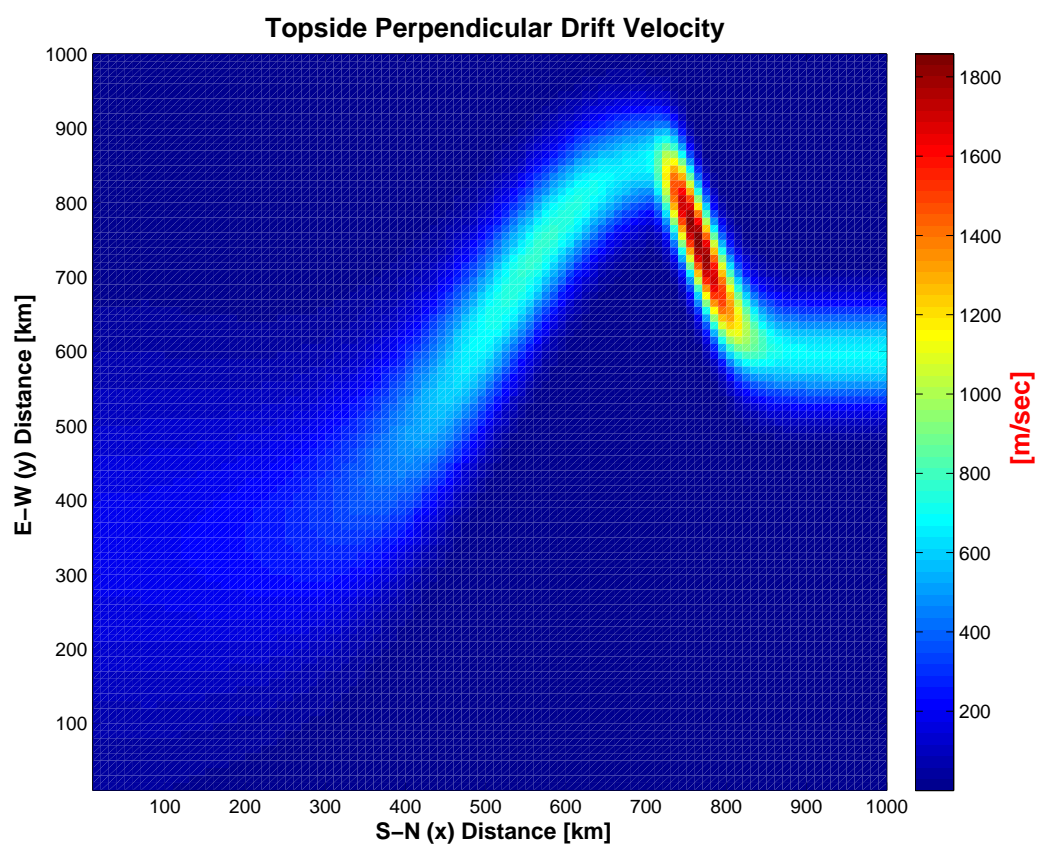Figure 5.1: Superdarn Radar Data from Feb 26, 2001.

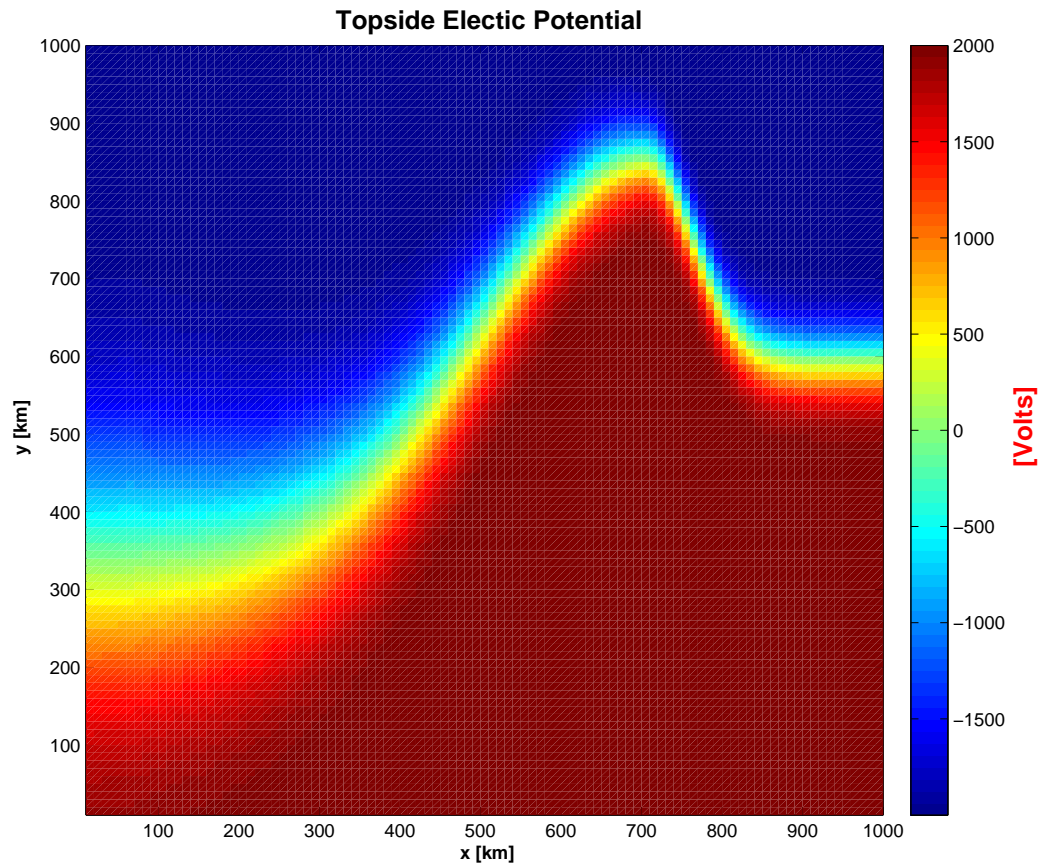Figure 5.2: Topside Perpendicular Drift Velocity.

Figure 5.3: Imposed Topside Boundary Condition Electric Potential.

the Pedersen currents. In the F region however, we have two distinct processes occurring simultaneously, the downward velocity driven by the pressure gradient (relatively small) and the chemical recombination of NO^+ (relatively large). As the plasma flow from the high velocity region to the low velocity region, the depleted plasma starts to stagnate creating low density region (79 percent reduction from the background density) after 2 minutes. In the meantime, perpendicular velocity continues transporting new plasma to undergo the similar process. As a result, after 496 seconds (Figure 5.6 and even 1028 seconds (Figure 5.7), we see a large affected area of low plasma density occurring in the lower x-axis region.

At the 600 and 800km altitudes, we see the nominal upflow of plasma enhancement particularly from the high temperature region and the perpendicular drift transports the dense plasma along the current system structure (see Fig. 5.6 and Fig. 5.7 at the 600 km and 800 km slices).

Velocity Evolution

In the E region, due to the high collision frequency with the neutral species, the parallel drift velocities appear to be small, similar to all the previous scenarios (see Figures 5.9 and 5.10). In the F region, we have downward velocities as before. However, in the higher altitude regions around 600 km in altitude, we have a upward and downward flow regions separated by the transitional region for the velocity (see Figures 5.9 and 5.10 at 600 km altitude.

Hypothesis

In Figure 5.7 and 5.6, there is a dense plasma region in the lower x-axis region (67 percent high than the background density). However, since the temperature in that
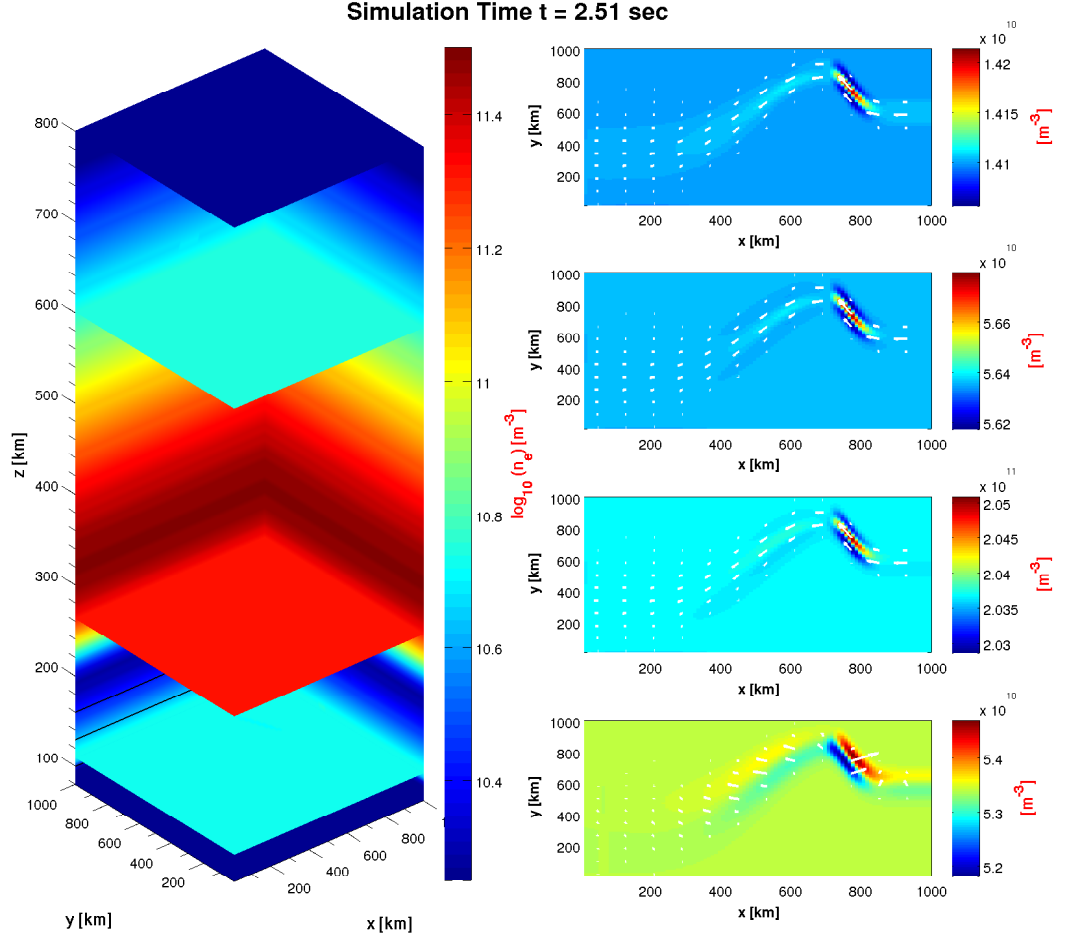
Figure 5.4: Initial Density Disturbance at t = 2.51 seconds. Slices occur at z = 125 km (E-Region), z = 251 km (F-Region), z = 600 km and z = 800 km altitudes.
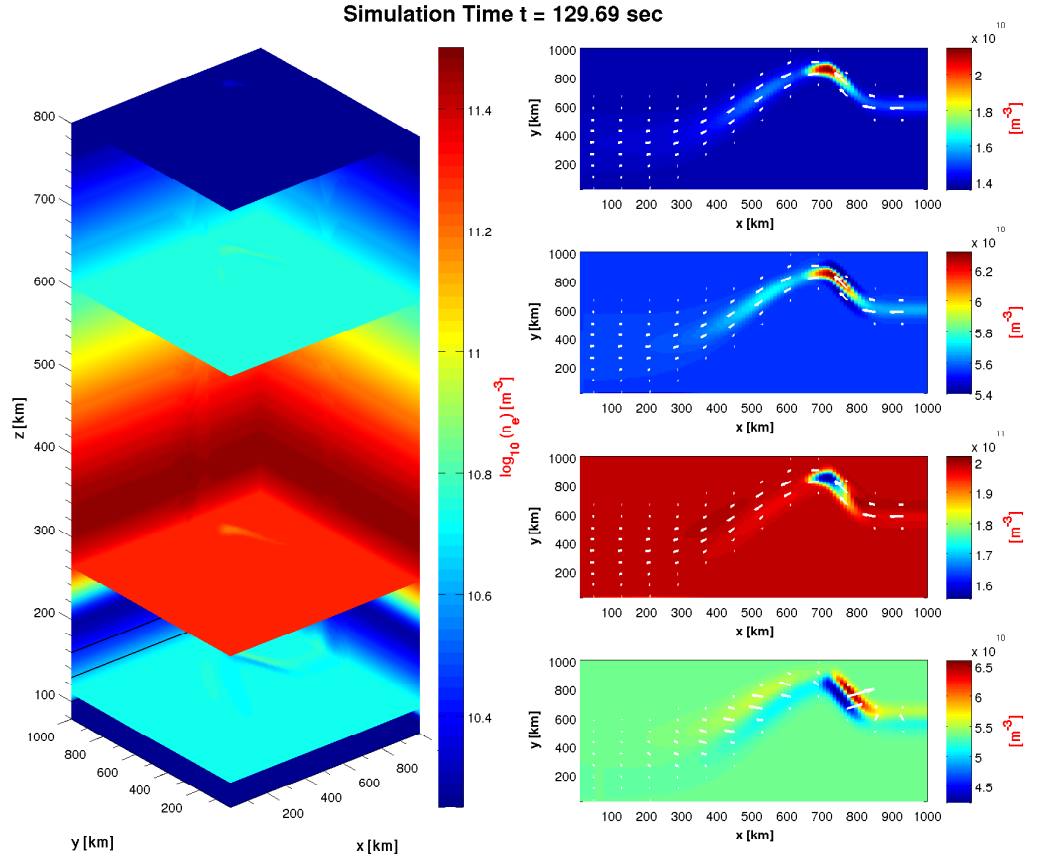
Figure 5.5: Disturbance continues to develop at t = 130 seconds (occuring in the F-region and above). Slices occur at z = 125 km (E-Region), z = 251 km (F-Region), z = 600 km and z = 800 km altitudes.

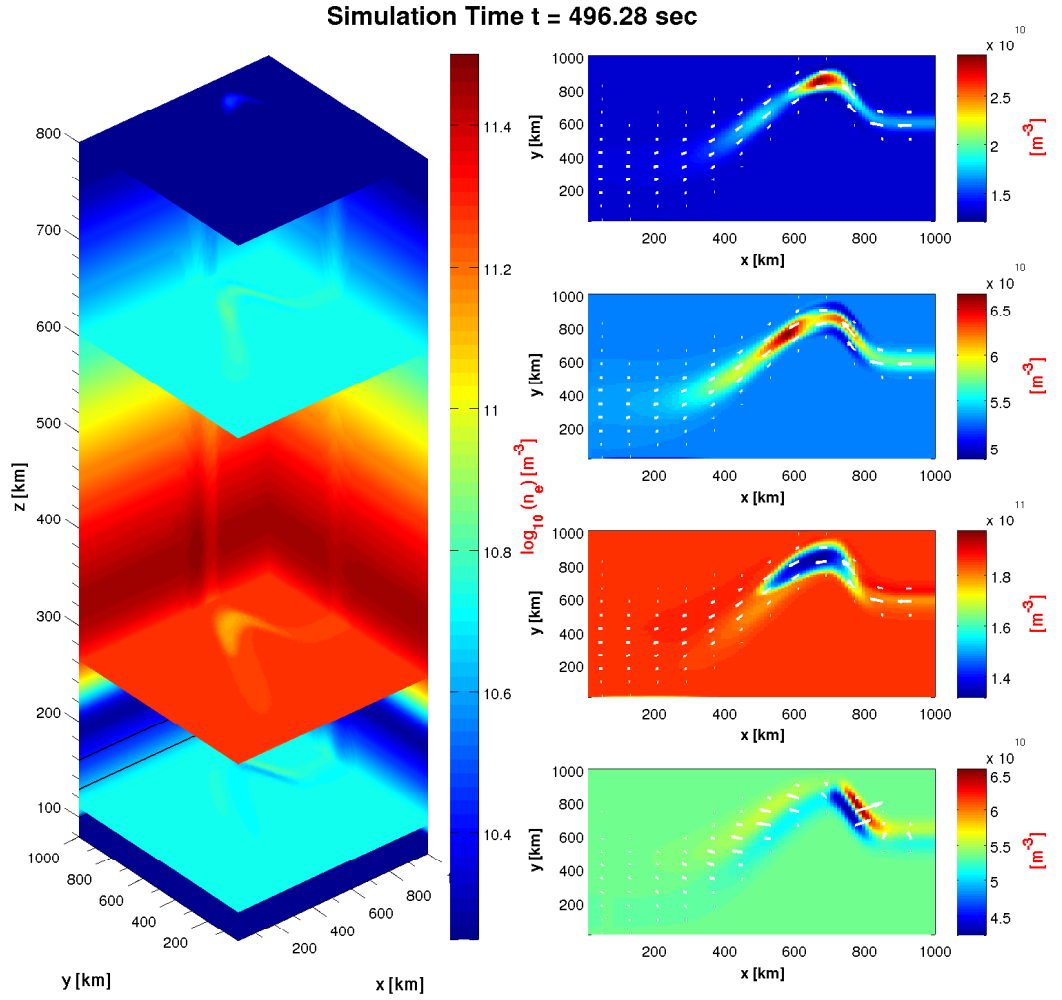Figure 5.6: Large scale disturbance at t = 496 seconds. Slices occur at z = 125 km (E-Region), z = 251 km (F-Region), z = 600 km and z = 800 km altitudes.
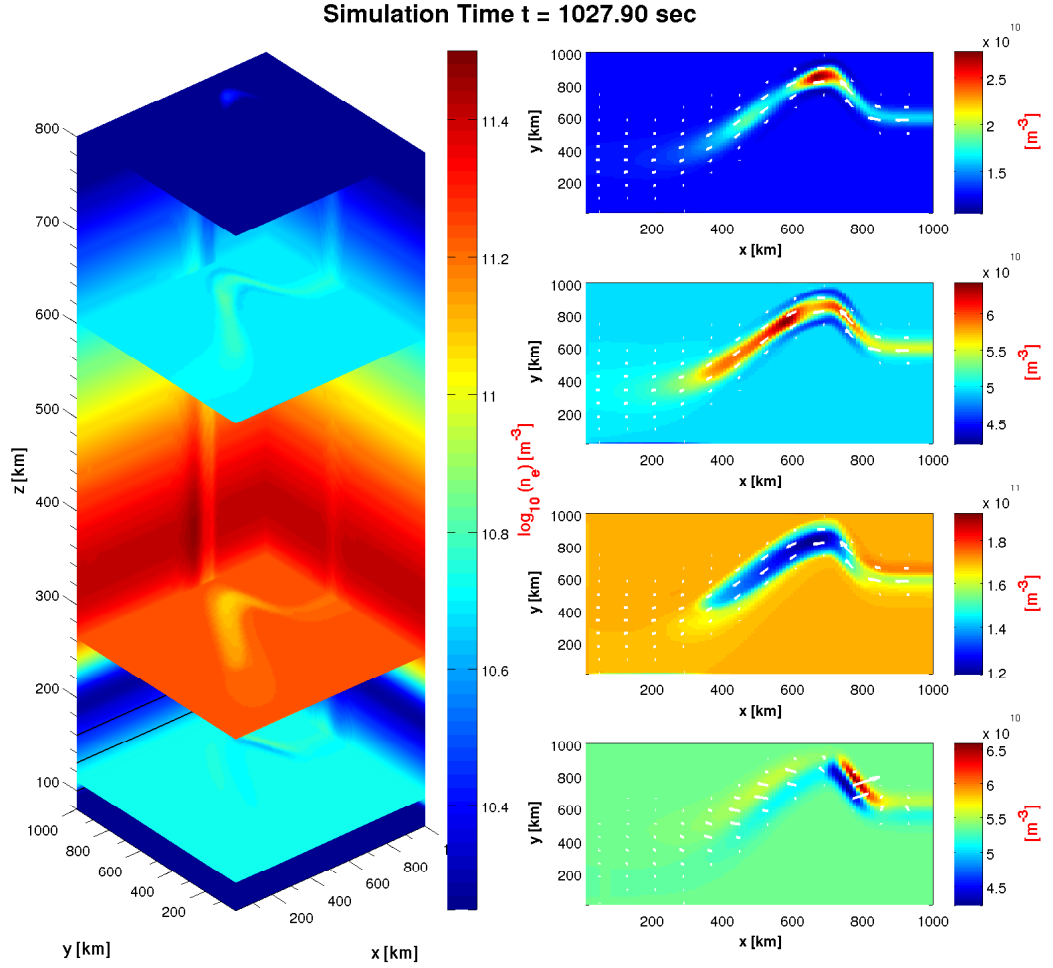
Figure 5.7: Large scale disturbance continues developing at t = 1027 seconds. Slices occur at z = 125 km (E-Region), z = 251 km (F-Region), z = 600 km and z = 800 km altitudes.

105

region (see Figure 5.8) is low (T$\approx 1500K$), the ion upflow is not as high. As a result, the pressure gradient due to the difference in densities between the dense plasma and background plasma dominates the flow direction causing the motion of the plasma to drift downward instead. Consequently, Figure 5.9 and 5.10 show at the 600km altitude, that we have both upward and downward flows on both sides of the transitional region. In the upper region, since the density enhancement is not high enough to cause any pressure gradient drift, we only observe the ion upflow. In other words, in the hotter region, the temperature intensifies the upward flow region. As a result, the plasma experiences positive velocity. In the meantime, the effect of $\mathbf{E} \times \mathbf{B}$ drift causes the particles to be ejected out to the cooler region. As a result, the sudden cooling causes the plasma to drift downward creating the upward and downward flow on both sides of the transitional region.
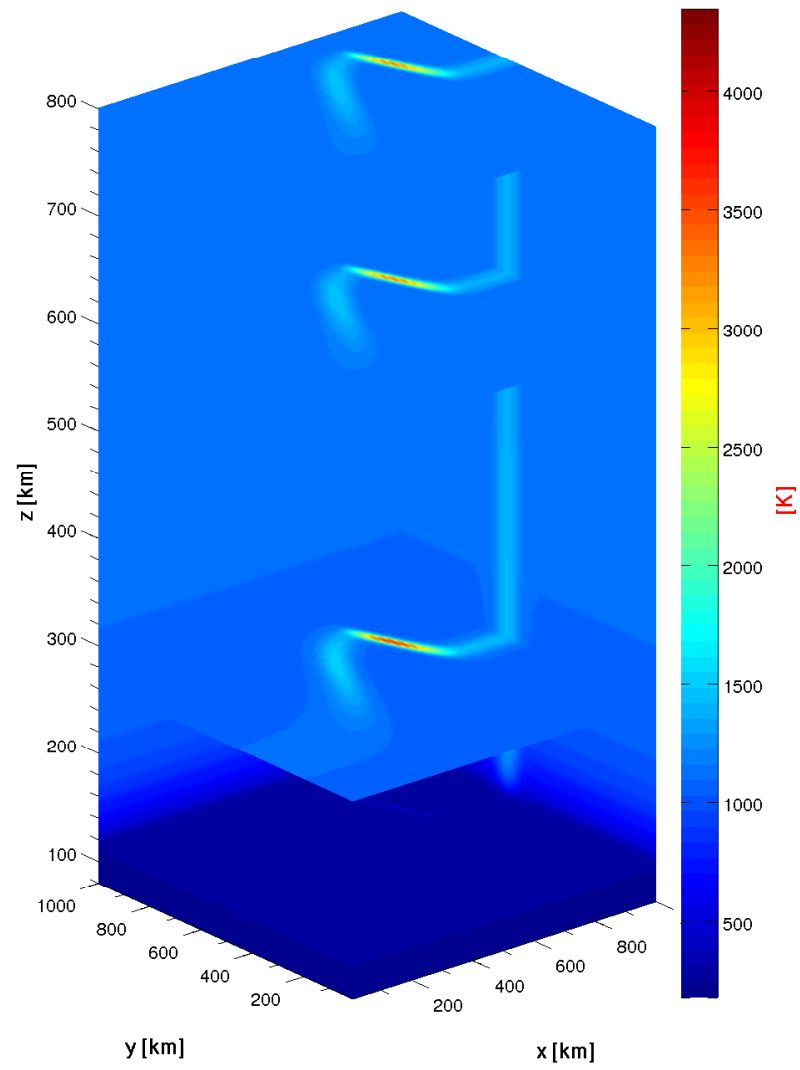
Figure 5.8: Equilbirum Temperature Profile.

Figure 5.9: The vertical drift velocity exhibits similar distrubance as plasma density at t = 496 seconds. Slices occur at z = 125 km (E-Region), z = 251 km (F-Region), z = 600 km and z = 800 km altitudes.
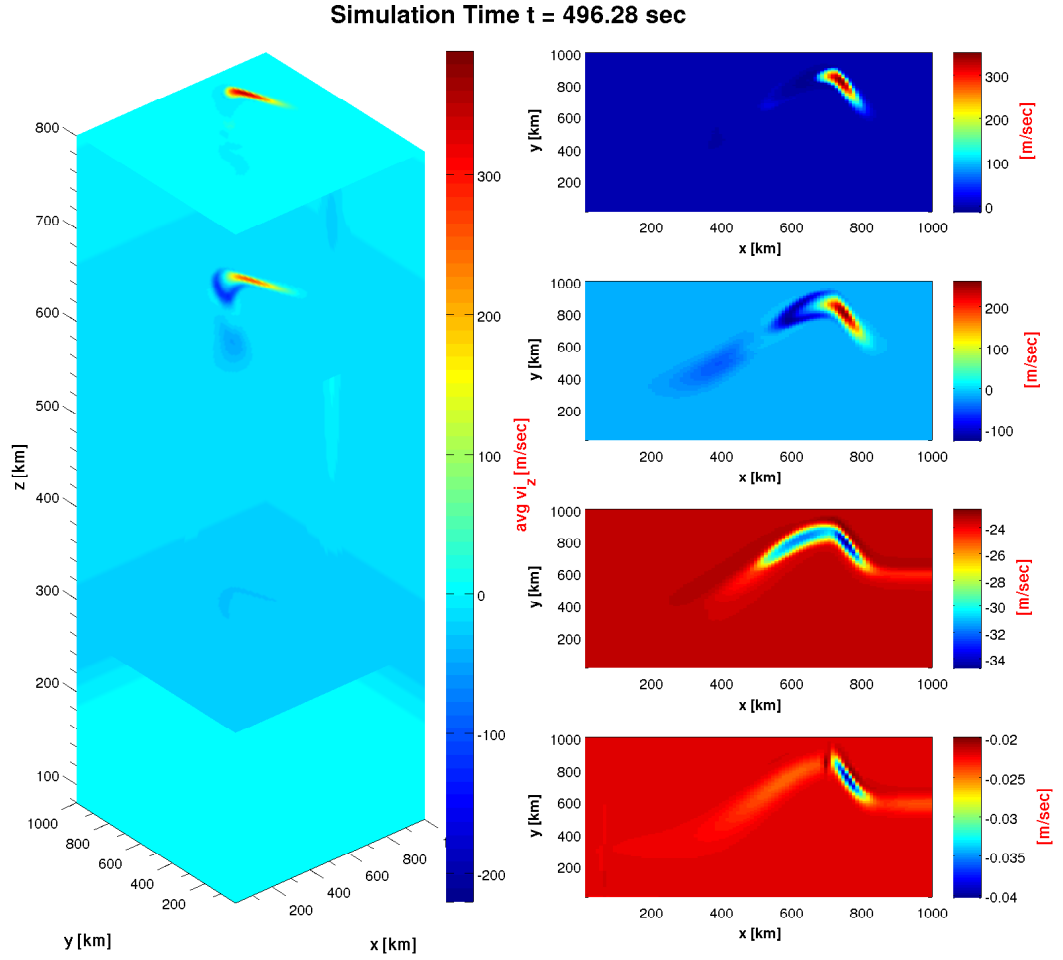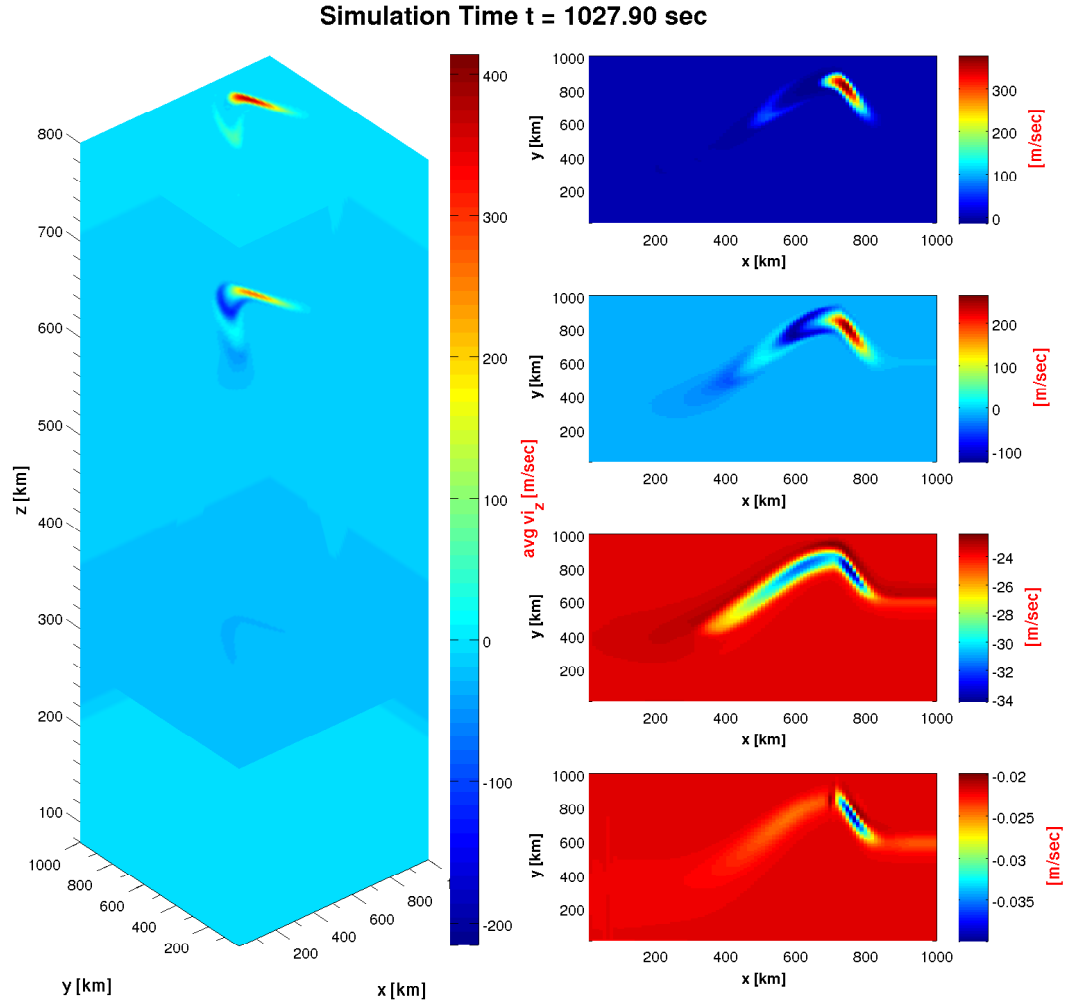
Figure 5.10: The vertical drift velocity exhibits similar distrubance as plasma density at t = 1028 seconds. Slices occur at z = 125 km (E-Region), z = 251 km (F-Region), z = 600 km and z = 800 km altitudes.

Conditions	Values[1]
B.C.	DTNE
Initial Condition	Equilibrium Profile: 3×10^{11} m^{-3} (E);1.19×10^{11} m^{-3} (F)
Neutral Winds	Yes
Electron Flux	0.1 mW/m^2
max. $\mid E_\perp \mid$	n/a
Slices	$z_1 = 110$ km

Table 5.2: Initial Setup for the Ionospheric Model with Neutral Wind Forcing

5.2 Ionospheric Response to Neutral Wave Forcing

In this study, we will examine the effects of acoustic waves on the auroral ionosphere. Unlike gravity waves, acoustic waves can be strongly localized as they propagate upward above their sources. To simulate this phenomenon, a compressible atmospheric model [Snively and Pasko, 2008] was used by solving the compressible Euler equations in cylindrical coordinates. Viscosity and thermal conduction are included via a time-split method. This model generates a directional upward forcing, which starts here at the bottom of the troposphere with a radius of approximately 30 km and a maximum vertical propagation of 250 km. This highly coherent and idealized source is simulated within a peak amplitude of approximately 1 percent of the atmospheric ambient pressure in the troposphere. As a result of the focused wave packet, it will not interfere with the horizontal boundaries of the 3-D auroral ionospheric model, which may
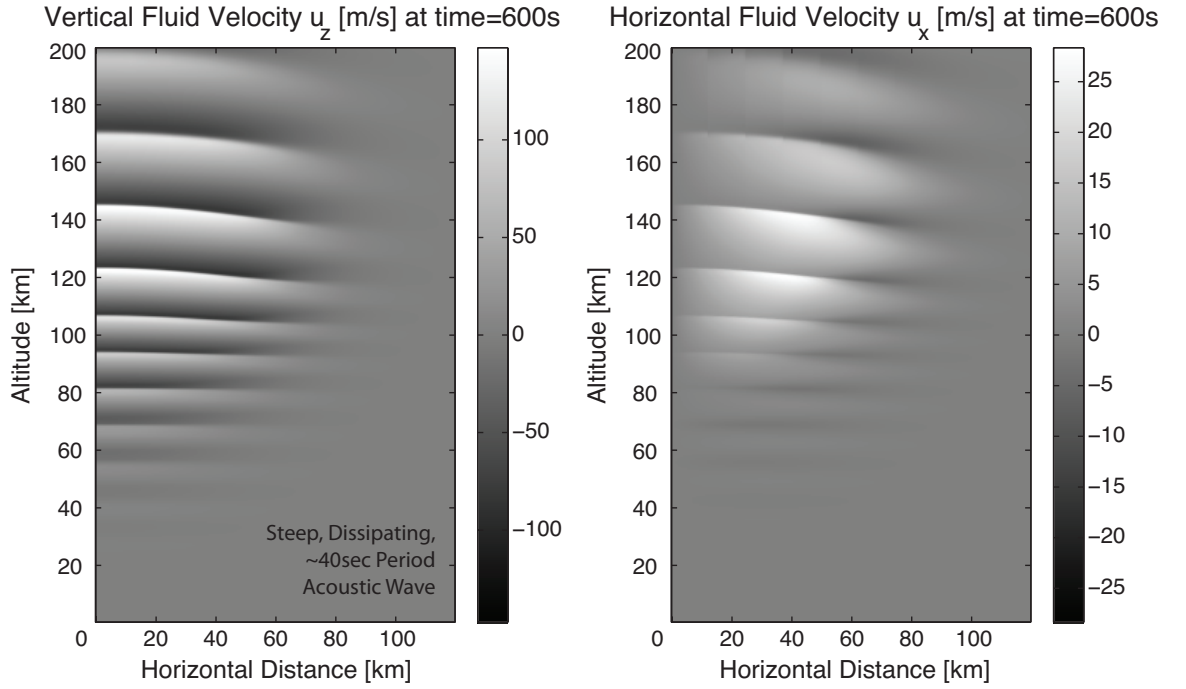
110

Figure 5.11: Acoustic Wave Profile in Cylinderical Coodinate System Provided by Dr. J. B. Snively.

create unwanted artifacts. Measurements from situ satellite have detected acoustic waves with similar amplitudes in the F-region ionosphere[Garcia et al., 2013]. Figure 5.11 illustrates the acoustic wave profile at t = 600 seconds in cylindrical coordinate system.

After performed a coordinate transformation from Cylindrical to Cartesian coordinate system, the neutral wind data become 3 sets of 3-D data that describe the winds in x, y and z directions. In this scenario, we will discuss the ionospheric responses in terms of dynamo currents and density variations. Figure 5.12, 5.13 and 5.14 show the 3 components of current densities with respect to altitudes. The depleting perpendicular velocity in higher altitude regions are clearly shown. That is

due to the diminishing strengths in neutral winds in altitudes. Interestingly, we also observe rotational currents structures in the E region. The complexity of this current system is due to the perpendicular current density calculation. Recall the current density equation with neutral winds disturbance

$$\mathbf{J}_\perp = \boldsymbol{\sigma}_\perp \cdot \mathbf{E}_{r\perp} + \sum_s n_s m_s \nu_s \boldsymbol{\mu}_{s\perp} \cdot \mathbf{v}_{n\perp}. \tag{5.1}$$

Here, the summation $\sum_s n_s m_s \nu_s \boldsymbol{\mu}_{s\perp}$ acts as an altitude dependent rotational matrix that transforms the neutral wind profile. Therefore, it invokes many interesting geometries as you see from Figure 5.15, 5.16 and 5.17. The magnitude of current density is significant enough to possibly be detected.

In addition to current density, vertical winds invoke interesting density enhancements of 5 to 25 percent. For example, at z=125 km altitude, upper right corner of Figure 5.18 shows an asymmetrical density feature. Based on the color bar, the densest regions (red regions) are around 17 percent more compared to the background density. Figure 5.18 shows a strong variations of such enhancements between 100 and 150 km in altitude with magnitudes between 7 percent to 23 percent. In the plot diagram shown in Figure 5.18, blue line indicates the absolute variations between the minimum and maximum densities at that particular altitude. The green line indicates the density variation at the center [150, 150] km of each discrete altitude, where the most activities occurred.

Discussion

Due to the complexity of strong neutral winds, further studies are needed to describe the processes involved in creating these interesting geometrical structures.
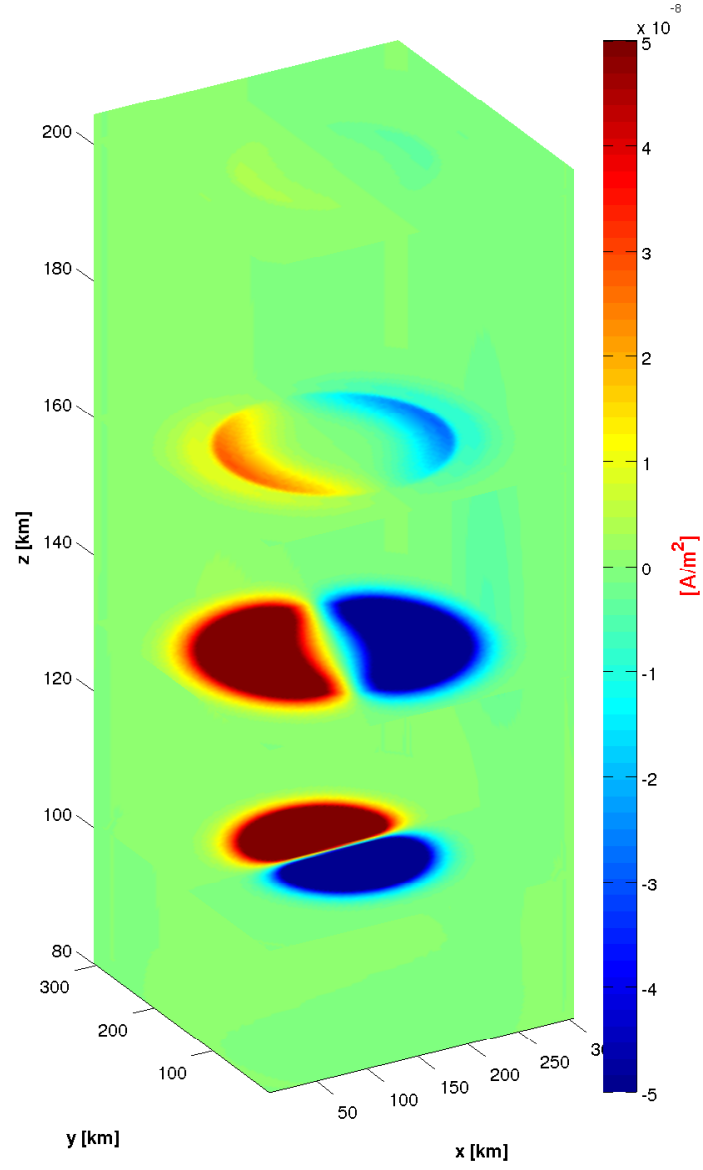
Figure 5.12: Ionosperic J_x Rsponse in Neutral Winds Model at t=458 seconds with peak current density of $\sim 1.4\ \mu Am^{-2}$. Slices occur at z = 100 km (E-Region), z = 130 km, z = 160 km altitudes.
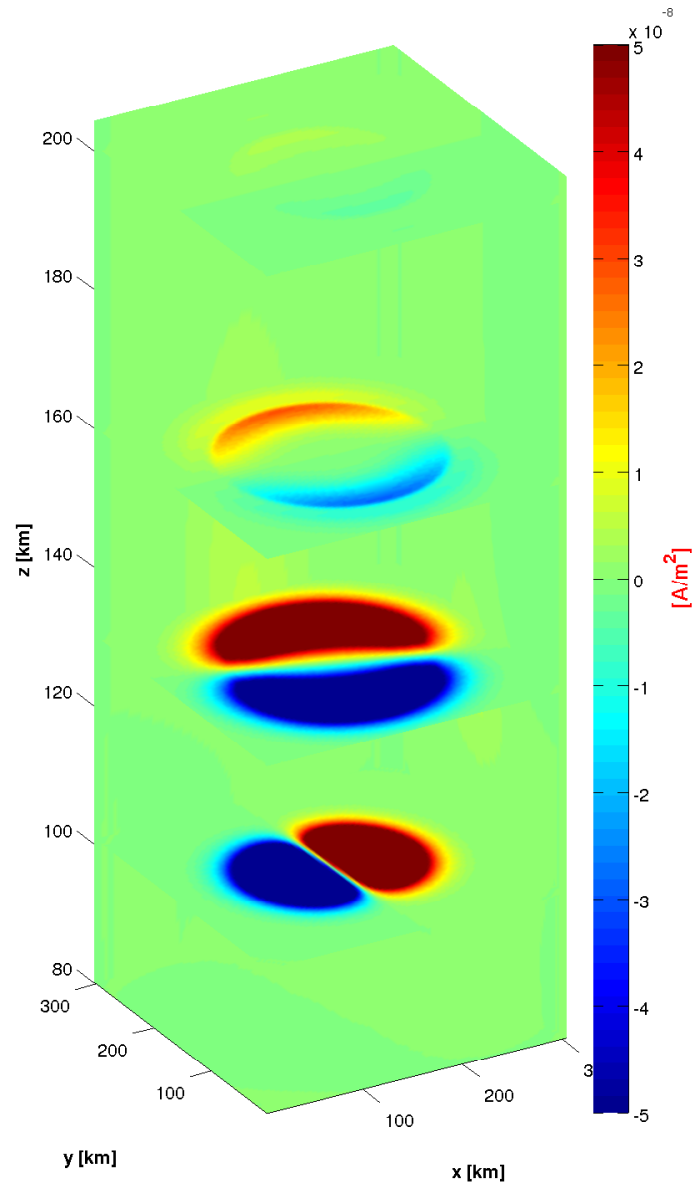
Figure 5.13: Ionosperic J_y Rsponse in Neutral Winds Model at t=458 seconds with peak current density of $\sim 1.4~\mu Am^{-2}$. Slices occur at z = 100 km (E-Region), z = 130 km, z = 160 km altitudes.
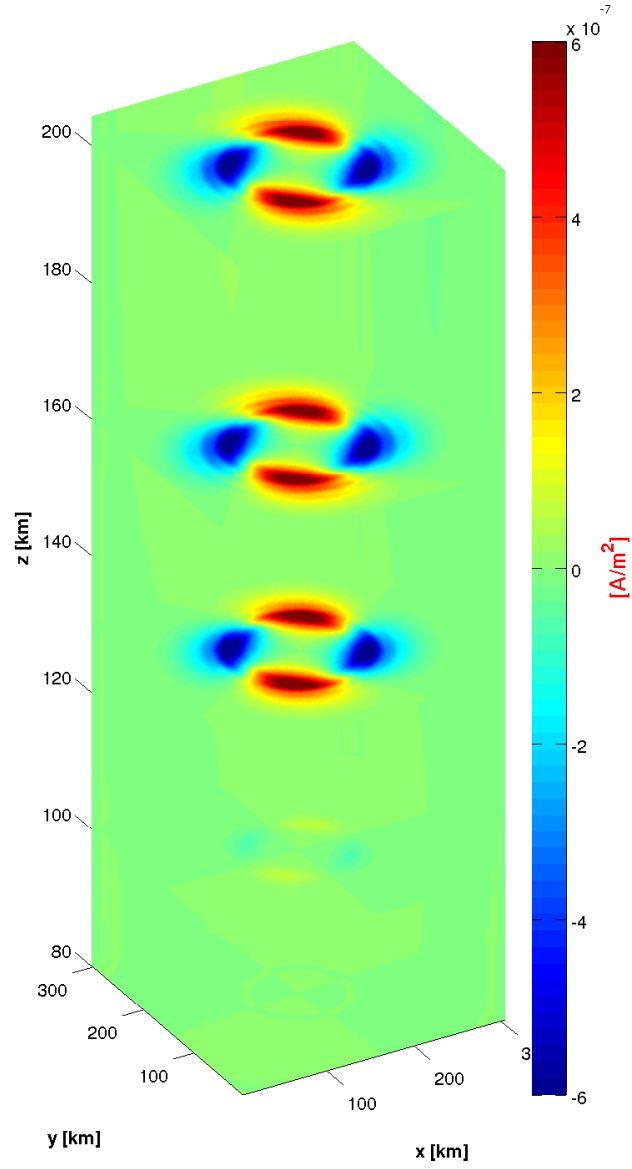
Figure 5.14: Ionosperic J_z Rsponse in Neutral Winds Model at t=458 seconds. Slices occur at z = 100 km (E-Region), z = 130 km, z = 160 km altitudes.

Figure 5.15: Perpendicular Current Response (J_x and J_y) due to Neutral Winds (v_{nx} and v_{ny} at t = 458.34 seconds and z = 100 km

Figure 5.16: Perpendicular Current Response (J_x and J_y) due to Neutral Winds (v_{nx} and v_{ny} at t = 458.34 seconds and z = 130 km

Figure 5.17: Perpendicular Current Response (J_x and J_y) due to Neutral Winds (v_{nx} and v_{ny} at t = 458.34 seconds and z = 160 kms
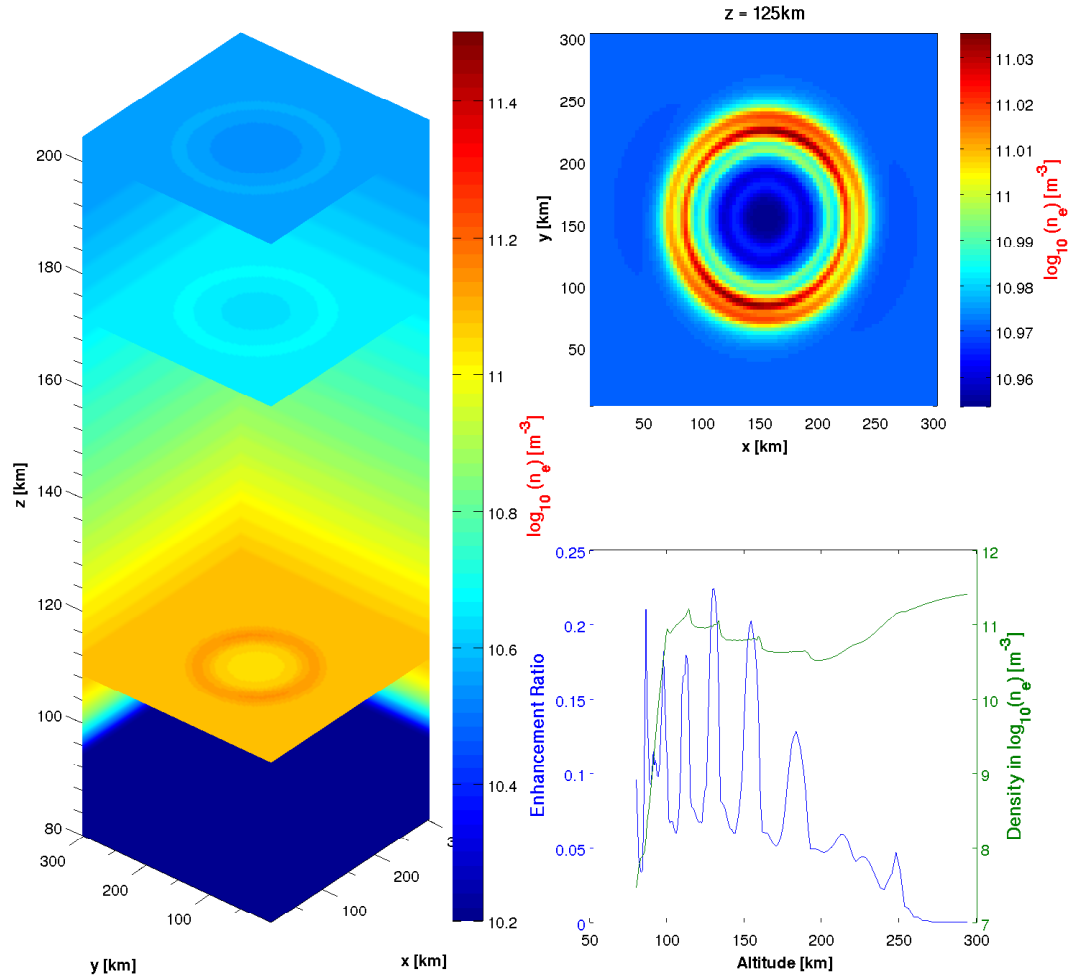
Figure 5.18: Electron Density Disturbance Due to Neutral Winds at t = 458 seconds
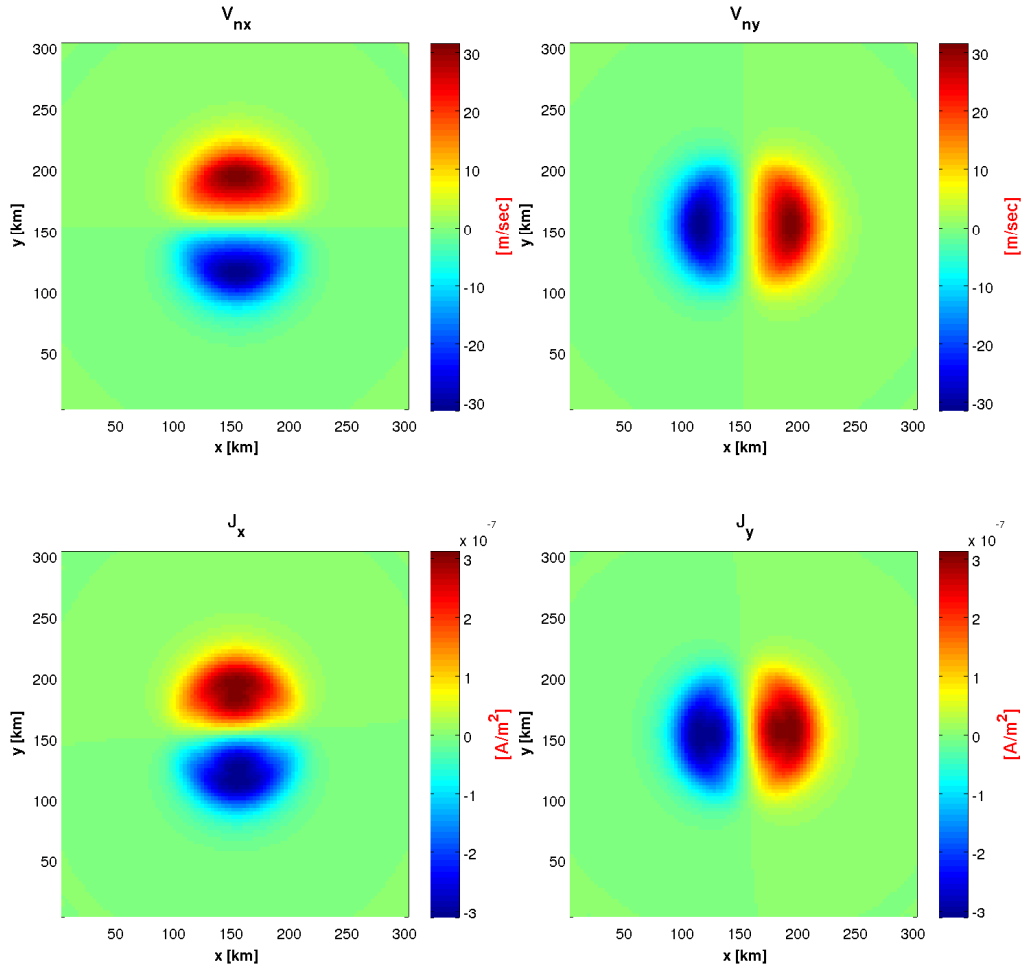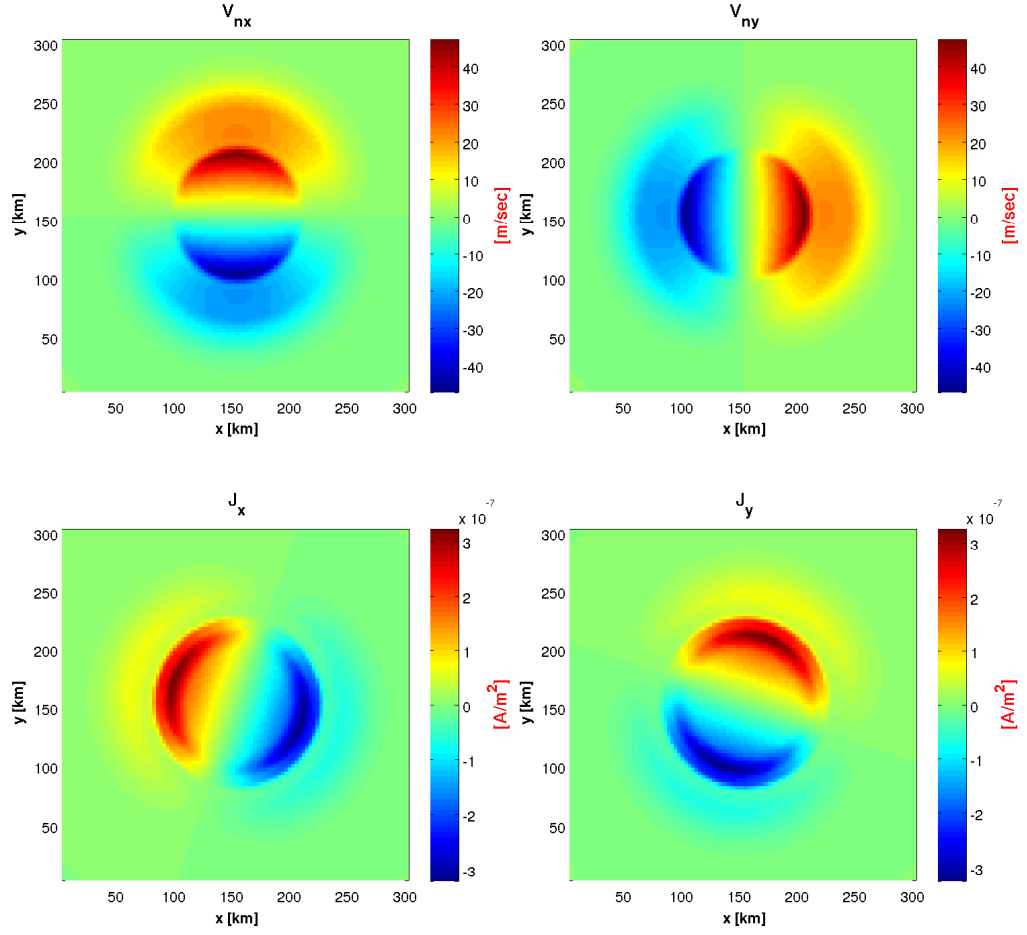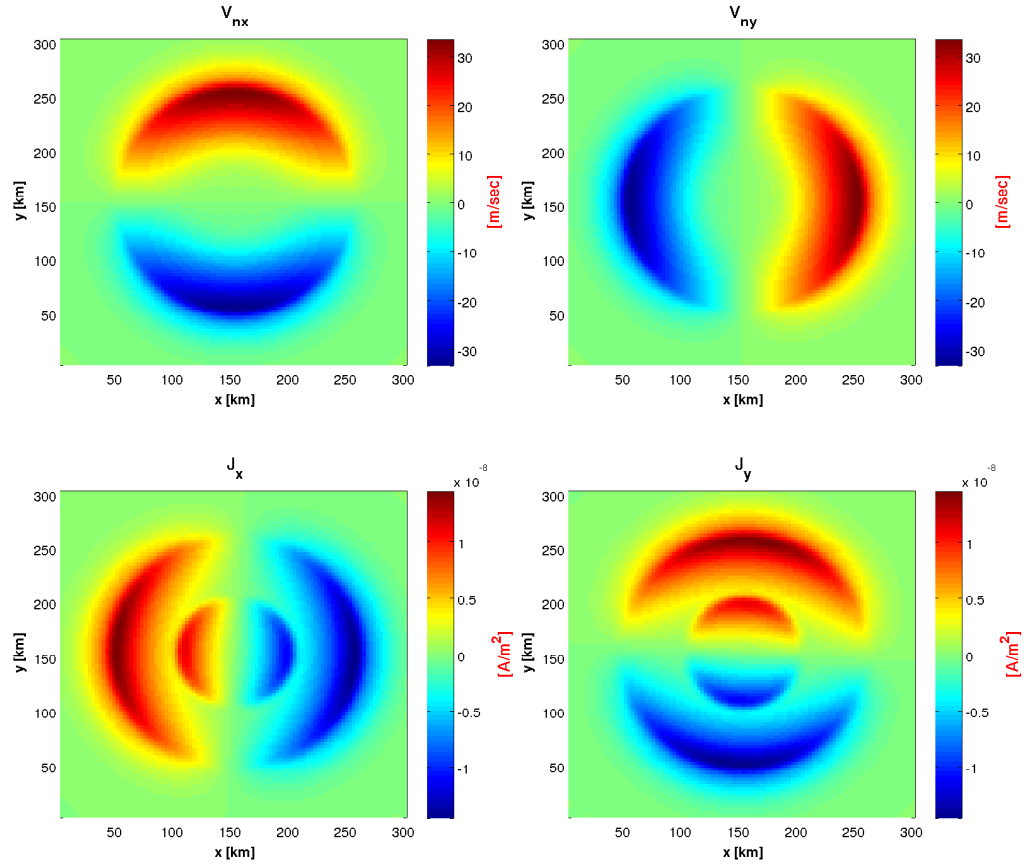
Quantitatively speaking, the variations in plasma density are significant enough that they should be detectable by instrumentation. In addition, it is significant that neutral wind and the neutral ion coupling are capable of generating a detectable current system without any imposed magnetospheric conditions. From a modeling standpoint, there are a number of improvements that can be made. For example, the grid level fluctuations in density can be a numerical artifact, probably caused by velocity profile being a discrete function with a 5-second interval, which could also trigger unwanted disturbance in our simulation. However, the atmospheric inputs demonstrated here are substantial, which create more opportunities for analyzing the implications of neutral winds in the ionospheric model.

Chapter 6

Conclusions and Future Work

The 3-D model has been developed and tested for variety of ionospheric scenarios:

- This new 3-D model is validated by comparing it to an existing 2-D simulation, the following features are shown to be in good agreement between the two models:

  - Plasma enhancement and depletion in the E region

  - Plasma frictional heating process

  - Ion upflow in high altitude regions

  - Chemically driven depletion process in the F region

  - Rough agreement was achieved between the simulated transitional altitude $\hat{z}$ and that estimated from the radar data

- This work resolved and evaluated the plausibility of 3-D Ionospheric Responses using a simplified Topside Potential Geometry.

- The project conducted a simulation case study to model ionospheric response to realistic topside potential patterns.

- This model demonstrated the ionospheric response due to neutral winds from large amplitude acoustic waves.

Currently, the 3-D model uses the energy balance approximation to resolve the ion temperature profile. For the future, the program will implement the full energy equation to describe this profile up to 1000 km. For the ionospheric data estimated by the incoherent scatter radar, there are still uncertainties due to the measurements. As a result, fully 3-D interpretations of the transitional altitudes require more in-depth analysis. Furthermore, literature has shown the phenomenon of $\mathbf{E} \times \mathbf{B}$ instability in high latitude ionosphere, several models of similar kind have successfully demonstrated its evolution [Huba et al., 1988; Yokoyama et al., 2008]. It is therefore important for our next iteration of this project is to show this capability. Lastly, the way the neutral winds were imported to the model needs to be altered to include temporal interpolation to reduce the unwanted numerical artifacts. In addition, neutral density fluctuation will be incorporated to demonstrate the full ionospheric response. These improvements should give researchers the first look into the complex effects of the coupling of the ionosphere and neutral winds.

Bibliography

P. M. Banks and G. Kockarts. *Aeronomy.* 1973.

R. Barrett, M. Berry, T. F. Chan, J. Demmel, J. M. Donato, J. Dongarra, V. Eijkhout, R. Pozo, C. Romine, and H. V. D. Vorst. Templates for the solution of linear systems: Building blocks for iterative methods, 1994.

P.-L. Blelly, J. Lilensten, A. Robineau, J. Fontanari, and D. Alcaydé. Calibration of a numerical ionospheric model with EISCAT observations. *Annales Geophysicae*, 14:1375–1390, December 1996. doi: 10.1007/s00585-996-1375-x.

Raphael F. Garcia, Sean Bruinsma, Philippe Lognonn, Eelco Doornbos, and Florian Cachoux. Goce: The first seismometer in orbit around the earth. *Geophysical Research Letters*, 40(5):1015–1020, 2013. ISSN 1944-8007. doi: 10.1002/grl.50205. URL http://dx.doi.org/10.1002/grl.50205.

R. A. Heelis. The effects of interplanetary magnetic field orientation on dayside high-latitude ionospheric convection. *Journal of Geophysical Research*, 89:2873–2880, May 1984. doi: 10.1029/JA089iA05p02873.

R. A. Heelis, W. R. Coley, M. Loranc, and M. R. Hairston. Three-dimensional iono-

spheric plasma circulation. *Journal of Geophysical Research*, 97:13903, September 1992. doi: 10.1029/92JA00872.

J. D. Huba, H. G. Mitchell, M. J. Keskinen, J. A. Fedder, P. Satyanarayana, and S. T. Zalesak. Simulations of plasma structure evolution in the high-latitude ionosphere. *Radio Science*, 23(4):503–512, 1988. ISSN 1944-799X. doi: 10.1029/RS023i004p00503. URL `http://dx.doi.org/10.1029/RS023i004p00503`.

J. D. Huba, S. L. Ossakow, G. Joyce, J. Krall, and S. L. England. Three-dimensional equatorial spread F modeling: Zonal neutral wind effects. *Geophysical Research Letters*, 36:L19106, October 2009. doi: 10.1029/2009GL040284.

J. David Jackson. *Classical Electrodynamics*. John Wiley & Sons, Inc., New Jersey, USA, 3 edition, 1991.

M.C. Kelley. *The Earth's Ionosphere: Plasma Physics and Electrodynamics*. International Geophysics. Elsevier Science, 2009. ISBN 9780080916576. URL `http://books.google.com/books?id=3GlWQnjBQNgC`.

R. J. LeVeque. *Finite Volume Methods for Hyperbolic Problems*. Cambridge University Press, 2002. URL `http://dx.doi.org/10.1017/CBO9780511791253`.

J.-M. A. Noël, J.-P. St.-Maurice, and P.-L. Blelly. Nonlinear model of short-scale electrodynamics in the auroral ionosphere. *Annales Geophysicae*, 18:1128–1144, September 2000. doi: 10.1007/s00585-000-1128-1.

M. H. Rees, V. J. Abreu, and P. B. Hays. The production efficiency of O/+//2P/

ions by auroral electron impact ionization. *Journal of Geophysical Research*, 87: 3612–3616, May 1982. doi: 10.1029/JA087iA05p03612.

P. C. Richards, J. A. Fennelly, and D. G. Torr. EUVAC: a solar EUV flux model for aeronomic calculations. *Journal of Geophysical Research*, 99:3283, May 1994.

H. Rishbeth and O.K. Garriott. *Introduction to ionospheric physics*. International geophysics series. Academic Press, 1969. URL http://books.google.com/books?id=YdbAAAAAIAAJ.

Y. Saad. *Iterative Meghods for Sparse Linear Systems*. The Pws Series in Computer Science. PWS Publishing Company (Thomson), 1996. ISBN 9780534947767. URL http://books.google.com/books?id=jLtiQgAACAAJ.

J.-P. Saint-Maurice and W. B. Hanson. Ion frictional heating at high latitudes and its possible use for an in situ determination of neutral thermospheric winds and temperatures. *JGR*, 87:7580–7602, September 1982. doi: 10.1029/JA087iA09p07580.

R. W. Schunk and A. F. Nagy. *Ionospheres*. November 2004.

R. W. Schunk and J. J. Sojka. Ion temperature variations in the daytime high-latitude f region. *Journal of Geophysical Research: Space Physics*, 87(A7): 5169–5183, 1982. ISSN 2156-2202. doi: 10.1029/JA087iA07p05169. URL http://dx.doi.org/10.1029/JA087iA07p05169.

R. W. Schunk and J. C. G. Walker. Theoretical ion densities in the lower ionosphere. *Planetary and Space Science*, 21:1875–1896, November 1973. doi: 10.1016/0032-0633(73)90118-9.

J. B. Snively and V. P. Pasko. Excitation of ducted gravity waves in the lower thermosphere by tropospheric sources. *Journal of Geophysical Research (Space Physics)*, 113:A06303, June 2008. doi: 10.1029/2007JA012693.

S. C. Solomon and L. Qian. Solar extreme-ultraviolet irradiance for general circulation models. *Journal of Geophysical Research (Space Physics)*, 110:A10306, October 2005. doi: 10.1029/2005JA011160.

J.-P. St.-Maurice and P. J. Laneville. Reaction rate of O+ with O2, N2, and NO under highly disturbed auroral conditions. *Journal of Geophysical Research*, 103: 17519–17522, August 1998. doi: 10.1029/98JA01387.

Y.-J. Su, R. G. Caton, J. L. Horwitz, and P. G. Richards. Systematic modeling of soft-electron precipitation effects on high-latitude F region and topside iono- spheric upflows. *Journal of Geophysical Research*, 104:153–164, January 1999. doi: 10.1029/1998JA900068.

J. H. Whitteker. The transient response of the topside ionosphere to precipita- tion. *Planetary and Space Science*, 25:773–786, August 1977. doi: 10.1016/0032- 0633(77)90129-5.

T. Yokoyama, Y. Otsuka, T. Ogawa, M. Yamamoto, and D. L. Hysell. First three-dimensional simulation of the Perkins instability in the nighttime midlati- tude ionosphere. *Geophysical Research Letters*, 35:L03101, February 2008. doi: 10.1029/2007GL032496.

T. Yokoyama, D. L. Hysell, Y. Otsuka, and M. Yamamoto. Three-dimensional simulation of the coupled perkins and es-layer instabilities in the nighttime

midlatitude ionosphere. *Journal of Geophysical Research: Space Physics*, 114 (A3):n/a–n/a, 2009. ISSN 2156-2202. doi: 10.1029/2008JA013789. URL http://dx.doi.org/10.1029/2008JA013789.

M. Zettergren and J. Semeter. Ionospheric plasma transport and loss in auroral downward current regions. *Journal of Geophysical Research: Space Physics*, 117(A6):n/a–n/a, 2012. ISSN 2156-2202. doi: 10.1029/2012JA017637. URL http://dx.doi.org/10.1029/2012JA017637.

M. D. Zettergren and J. L. Semeter. Ionospheric heating, upwelling, and depletions in auroral current systems. *AGU Fall Meeting Abstracts*, page B5, December 2010.

H. Zhu, A. Otto, D. Lummerzheim, M. H. Rees, and B. S. Lanchester. Ionosphere-magnetosphere simulation of small-scale structure and dynamics. *Journal of Geophysical Research*, 106:1795–1806, February 2001. doi: 10.1029/1999JA000291.